Cosmoparticle Constraints with Large-Scale Structure

Constance Mahony

Submitted for the degree of Doctor of Philosophy

Department of Physics and Astronomy

University College London

Supervisors:

Dr. Benjamin Joachimi & Dr. Andreas Korn

Prof. Hiranya V. Peiris

Examiners:

Prof. Anthony Challinor

Prof. David Waters

14th December 2020

I, *Constance Mahony*, confirm that the work presented in this thesis is my own. Where information has been derived from other sources, I confirm that this has been indicated in the thesis. In particular, I would like to point out the following contributions:

- C. Mahony et al. Target Neutrino Mass Precision for Determining the Neutrino Hierarchy. *Phys. Rev. D*, 101(8):083513, 2020.
- M. C. Fortuna et al. The halo model as a versatile tool to predict intrinsic alignments. arXiv:2003.02700, 2020.

Abstract

Precisely measuring the large-scale structure of the universe is key to learning about fundamental physics. This thesis focuses on two of the most pressing problems in fundamental physics; massive neutrinos and dark energy, and explores what can be learnt from precise measurements of the large-scale structure of the universe.

First, I examine the precision required for large-scale structure measurements to determine the neutrino hierarchy when combined with current particle physics results. The neutrino hierarchy refers to the ordering of the neutrino masses, and is a key question in neutrino physics. Particle physics and cosmology provide complementary information about neutrinos so a joint analysis is highly desirable. However, the method of incorporating prior knowledge about neutrinos into the analysis can strongly influence any results. I therefore developed a prior which is agnostic to the hierarchy by design, and used it to set a conclusive target precision for upcoming cosmological experiments.

Second, I forecast whether including weak lensing magnification in future large-scale structure analyses can improve the constraints on dark energy and dark matter. Weak gravitational lensing is one of the key probes in forthcoming galaxy surveys, such as the Vera Rubin Observatory. Usually, the signal is detected by measuring distortions to the shapes of millions of galaxies - weak lensing shear. However, it can also be detected by measuring fluctuations in the number density of galaxies across the sky - weak lensing magnification. Weak lensing magnification only requires a count of galaxies to be made, as opposed to a measurement of their shape so is therefore traceable even for the very faint, small, and distant galaxies. In this thesis, I determined whether including weak lensing magnification in upcoming deep large-scale structure analyses improves the final cosmological constraints.

Impact Statement

This thesis focusses on the precision of upcoming large-scale galaxy surveys. These surveys will provide vast astronomical datasets, to better understand the fundamental properties of our Universe.

Our work sets a target precision for these surveys to determine the neutrino hierarchy, when combined with current particle physics measurements. Massive neutrinos are evidence of physics beyond the Standard Model of particle physics, and the ordering of the three neutrino masses – the neutrino hierarchy – is a key unanswered question. Since upcoming galaxy surveys will have huge statistical power their results will be limited by systematic effects. Our target precision therefore sets a clear aim for systematics control, which can guide the analysis choices.

Our work also explores the impact of a particular systematic effect, called weak lensing magnification, on upcoming weak lensing analyses. Weak lensing is a technique, which probes the distribution of both light and dark matter in the Universe, and is a key probe for future large-scale galaxy surveys. Weak lensing magnification has previously not been included in standard weak lensing analyses, but due to improvements in statistical precision will need to be included in future studies to avoid biasing the results. We confirmed this bias, and also found that including weak lensing magnification can increase the precision of the final cosmological constraints. This work will therefore inform the core analysis of future surveys, and help to improve the accuracy and precision of the final results.

The work in this thesis has resulted in one peer-reviewed publication (chapter 2), which has already been cited by several other independent studies, and a second near submission (chapter 3). The PhD candidate has given over 10 professional presentations, including invited talks, at a variety of international institutions. Additionally, the work in this thesis involved the collaboration of both cosmologists and particle physicists, thereby helping to build greater interdisciplinary collaboration.

Acknowledgements

Firstly, thank you to my supervisors Benjamin Joachimi and Andreas Korn for your expert guidance and endless patience. Benjamin, thank your for your questions, which always get to the heart of the matter and make me think more deeply. Andreas, thank you for sharing your programming expertise without which I would be lost, and for all the cups of tea! My gratitude also goes to my second supervisor Hiranya Peiris for your amazing insight into current cosmology, and for teaching me the skills to be a better researcher.

I would like to thank my collaborators; Boris Leistedt for your encouragement and advice, Jonathan Braden for teaching (confusing?!) me about neutrino theory, and Linda Cremonesi and Ryan Nichol for helping me to understand particle physics measurements. Special thanks goes to Maria-Cristina Fortuna for your trips to UCL to help me implement your halo model code.

My time at UCL would not have been such a pleasure were it not for the students and postdocs of the Astrophysics group. Thank you for all the lunches and pub trips. In particular, thank you to my cosmology contemporaries Martin, Krishna and Harry, our catch up dinners kept me grounded.

An important thank you also goes to UCL psychological services, and Martina and Wendy for helping me to manage the many anxieties of a PhD.

Finally, thank you to my parents for all the opportunities that made a PhD possible, and to my partner Tom. You have been there through all of the ups and downs. Thank you for your endless encouragement and support, and especially all of your delicious cooking!

Contents

List of Figures

List of Tables

1 Introduction

1.1 The Cosmological Model

In the last 30 years cosmology has transformed from a largely speculative data-starved science into a field able to precisely test theoretical predictions with observations. This is due to the advent of large datasets from cosmic microwave background satellites, such as the Cosmic Background Explorer (COBE) (Mather et al., 1990) and Wilkinson Microwave Anisotropy Probe (WMAP) (Bennett et al., 2013), large galaxy surveys such as the 2dF Galaxy Redshift Survey (Colless et al., 2001), observations of supernovae (Perlmutter et al., 1999; Riess et al., 1998) and many others. These observations are able to test the fundamental predictions of the cosmological model and cosmology is now a data intensive science, focussed on how to extract information from these large and complex datasets.

The current cosmological model is underpinned by two aspects; the cosmological principle and Einstein's theory of General Relativity. The cosmological principle states the Universe is homogeneous and isotropic, i.e., the Universe looks the same from every observing position and in every direction. Einstein's theory of General Relativity connects the matter distribution within the universe to the structure of spacetime. These fundamentals can explain the large scale geometry of the Universe, and once coupled with the knowledge that the Universe is expanding, enable an understanding of the history of the Universe. However, clearly the Universe is not perfectly smooth. In order to explain the development of structure in the Universe, such as galaxies, we require deviations from this uniformity.

In this introduction we present the key results of General Relativity, describe the contents of the Universe, the expansion history of the Universe in relation to these contents and the development of structure. Next we introduce the technique of weak lensing, the focus of chapter 3, and finally

include a discussion of neutrinos in particle physics and cosmology, the focus of chapter 2. The key references for much of this introduction are the textbooks Dodelson (2003), Mo et al. (2010) and Schneider (2015); and the lecture notes from both the Imperial College cosmology course, and the two University College London cosmology courses.

1.1.1 General Relativity

Einstein's theory of General Relativity links gravity to the underlying geometry of spacetime. This geometry is summarized by a metric, which gives the physical distance between two points in a coordinate system. For a homogeneous and isotropic universe the metric is the Friedmann-LeMaître-Robertson-Walker metric (FLRW):

$$ds^2 = c^2dt^2 - a^2(t)\left[\frac{dr^2}{1-\kappa r^2} + r^2 d\Omega^2\right] , \tag{1.1}$$

where $d\Omega^2 = d\theta^2 + \sin^2\theta d\phi^2$. ds is the infinitesimal line element of spacetime, t is the time coordinate and r, θ and ϕ are the spatial coordinates. The geometry of spacetime is therefore specified by the scale factor $a(t)$, which describes how the length scale of the universe changes with time, and the curvature κ. If $\kappa < 0$ the universe has an open geometry, $\kappa = 0$ the universe has a flat geometry and $\kappa > 0$ the universe has a closed geometry.

The geometry of the universe, the metric, is related to the matter and energy in the universe by the Einstein equation:

$$G_{\mu\nu} \equiv R_{\mu\nu} - \frac{1}{2}g_{\mu\nu}R = 8\pi G T_{\mu\nu} + \Lambda g_{\mu\nu} , \tag{1.2}$$

where $G_{\mu\nu}$ is the Einstein tensor, $R_{\mu\nu}$ is the Ricci tensor, which depends on the metric $g_{\mu\nu}$, and $R = g^{\mu\nu}R_{\mu\nu}$ is the Ricci scalar. The infinitesimal line element ds (eq. 1.1) is related to the metric $g_{\mu\nu}$ as $ds^2 = g_{\mu\nu}dx^\mu dx^\nu$. Λ is the cosmological constant, G is Newton's constant and $T_{\mu\nu}$ is the energy momentum tensor, which summarises the energy content of the universe. Λ was first introduced by Einstein to provide a solution for a static universe, but today accounts for the accelerated expansion of our Universe due to dark energy (see section 1.1.2).

If we employ the cosmological principle once again to give the energy momentum tensor the form of a perfect fluid $T_{\mu\nu} = \mathrm{diag}[\rho, P, P, P]$, where ρ is the energy density and P is the pressure of

the fluid, we can insert the FLRW metric into the Einstein equation and obtain

$$\left(\frac{\dot{a}}{a}\right)^2 = \frac{8\pi G}{3}\rho - \frac{\kappa c^2}{a^2} + \frac{\Lambda c^2}{3} \,, \tag{1.3}$$

$$\frac{\ddot{a}}{a} = -\frac{4\pi G}{3}\left(\rho + \frac{3P}{c^2}\right) + \frac{\Lambda c^2}{3} \,. \tag{1.4}$$

These are the Friedmann equations and they specify the rate of expansion or contraction of the universe, $\dot{a}/a$, and whether this evolution is accelerating or decelerating, $\ddot{a}/a$. We discuss some details of these equations in the sections below.

Hubble Parameter

The expansion rate is often referred to as the Hubble parameter,

$$H(t) = \frac{\dot{a}}{a} \,, \tag{1.5}$$

and the expansion rate today, at time t_0, is the Hubble constant H_0. It is often presented in terms of h where,

$$H_0 = 100h \text{ km s}^{-1}\text{Mpc}^{-1}. \tag{1.6}$$

The Hubble constant was actually first introduced by Georges Lemaître in 1927 (Lemaître, 1927), and then by Edwin Hubble in 1929 (Hubble, 1929). They observed that galaxies move away from the Earth with a velocity proportional to their distance,

$$v = H_0 d \,, \tag{1.7}$$

where v is the recession velocity and d is the distance. This observation that $H_0 > 0$ determined the Universe was expanding, and began modern cosmology.

Redshift

Hubble and Lemaître measured the recession velocities of galaxies by measuring the wavelength of the photons emitted by these galaxies. In an expanding universe the wavelength of photons emitted from a galaxy is stretched along with the expansion, $\lambda \propto a$, so the observed wavelength is greater

than the emitted wavelength. This stretching is often defined in terms of redshift z,

$$1 + z = \frac{\lambda_{\rm obs}}{\lambda_{\rm em}} = \frac{a(t_{\rm obs})}{a(t_{\rm em})} \, . \tag{1.8}$$

If the emitted wavelength is known, for example the photon comes from a known spectral line, then the redshift provides a direct connection to the scale factor at the time of emission $a(t_{\rm em})$. This is because the scale factor today is taken to be 1 by convention, $a(t_0) = 1$, so the scale factor at observation $a(t_{\rm obs})$ is usually set to 1. Measuring redshifts is therefore a vital tool for studying the expansion of the Universe.

Density Parameters

The first Friedmann equation (eq. 1.3) connects the rate of the expansion of the universe to the energy density, curvature and cosmological constant. The density parameter is defined as,

$$\Omega = \frac{8\pi G}{3H^2}\rho = \frac{\rho}{\rho_{\rm crit}} \, . \tag{1.9}$$

The relevance of the critical density $\rho_{\rm crit}$ can be seen by setting $\Lambda = 0$. In this case,

$$\Omega - 1 = \frac{\kappa c^2}{H^2 a^2} \, , \tag{1.10}$$

so if the energy density of the universe ρ is equal to the critical density $\rho_{\rm crit}$ the universe is flat, if it is greater the universe is closed and if it is smaller the universe is open.

This density parameter formalism can be extended to the curvature, $\Omega_\kappa = -\kappa c^2/H^2 a^2$, and cosmological constant, $\Omega_\Lambda = \Lambda c^2/3H^2$, to convert eq. 1.3 to,

$$\Omega + \Omega_\kappa + \Omega_\Lambda = 1 \, . \tag{1.11}$$

Density Evolution

Combining the two Friedmann equations (eqs. 1.3 and 1.4) gives the continuity equation,

$$\frac{d\rho}{dt} + 3H\left(\rho + \frac{P}{c^2}\right) = 0 \, . \tag{1.12}$$

Integrating this equation, and including an equation of state connecting the energy density and pressure of the form $P = w\rho$, gives the solution,

$$\rho \propto a^{-3(1+w)} \ . \tag{1.13}$$

This relates the energy density of the universe to the expansion. Different fluids have different values of w; for non-relativistic matter (where the average kinetic energy of a particle is small compared to its rest mass) w=0, for radiation/relativistic matter w=1/3, and for a cosmological constant w=-1. As the universe expands the radiation density decreases more rapidly than the matter density, as in addition to the dilution the wavelength is stretched, and the cosmological constant density does not change. The first Friedmann equation can then be written in terms of the density parameters as,

$$\left(\frac{H}{H_0}\right)^2 = \Omega_{m,0}(1+z)^3 + \Omega_{r,0}(1+z)^4 + \Omega_{\kappa,0}(1+z)^2 + \Omega_\Lambda \ , \tag{1.14}$$

where the subscript 0 indicates the value of the associated energy density today and the scale factor a has been converted to redshift z using equation 1.8.

We can also relate the evolution of the scale factor directly to the type of fluid dominating the energy density. If we assume that the universe only contains one fluid and substitute the density solution in eq. 1.13 into the first Friedmann equation we find,

$$a \propto \begin{cases} t^{\frac{2}{3(1+w)}}, & \text{if } w \neq -1 \\ e^{Ht}, & \text{if } w = -1 \end{cases} \ . \tag{1.15}$$

In a radiation-dominated universe the scale factor grows as $t^{1/2}$, in a matter-dominated universe the scale factor grows as $t^{2/3}$ and in a cosmological-constant-dominated universe the scale factor grows exponentially.

1.1.2 The Contents of the Universe

The equations above show that the evolution of the Universe is governed by the energy density of its main components. Currently, the most popular model of cosmology is the Λ-Cold Dark Matter (ΛCDM) model with the additional assumption that the Universe is flat. It contains the following components:

Radiation

Radiation refers to relativistic components, and is mostly comprised of photons from the cosmic microwave background (CMB). The only other contribution is from a background of neutrinos (see section 1.4). At the present time radiation comprises less than 1% of the energy density of the Universe.

Baryons

The term baryons, in cosmology, refers to all visible matter including protons, neutrons and electrons (even though electrons are not baryons). Baryons make up approximately 5% of the energy density of the current Universe, and form all the stars and galaxies that astronomers observe.

Dark Matter

Dark matter forms the majority of the non-relativistic matter content in the Universe, and approximately 25% of the total energy density. It does not interact electromagnetically (dark) and its existence has only been inferred indirectly through gravitational effects. The evidence for dark matter comes from: the velocity dispersion of galaxies in clusters (Zwicky, 1933), the rotation curves of galaxies (Rubin and Ford, 1970), gravitational lensing (Clowe et al., 2006) and the CMB (Aghanim et al., 2018). The nature of dark matter remains unknown and is an active area of research. One proposed candidate is the Weakly Interacting Massive Particle (WIMP), which interacts with ordinary matter through an interaction that is weaker than the weak interaction, and through gravity. Three different avenues are being pursued to detect WIMPS; direct, indirect and accelerator searches. Direct searches focus on spotting the rare occasions when WIMP particles interact with ordinary matter in lab-based experiments; indirect searches look for signatures of WIMP annihilation in high density regions in the Universe; and accelerators attempt to reach sufficient energies to produce WIMPS (Tanabashi et al., 2018). Currently there is no definitive evidence for the existence of a WIMP particle. Another possible candidate is the axion, a very light particle, which a direct detection experiment XENON1T may recently have found a hint of (Aprile et al., 2020). XENON1T observed an excess of events at low energies, however radiological backgrounds cannot be completely excluded at this point.

Dark Energy

The remaining approximately 70% of the Universe comprises of Dark Energy. Dark energy is responsible for the accelerating expansion of our current Universe, which was first discovered through observations of supernovae in 1998 (Perlmutter et al., 1999; Riess et al., 1998) and won the 2011 Nobel prize. Little is known about the nature of dark energy except that its effects are similar to those of a cosmological constant; dark energy replaces the cosmological constant and reinterprets the term as a contribution to the energy-momentum tensor with $w = -1$. Whether dark energy evolves with time, e.g. $w(a) = w_0 + [1 - a(t)]w_a$, and can be explained by a new theory of modified gravity are active areas of research in cosmology.

1.1.3 Expansion History

The Big Bang theory rests on three key pieces of observational evidence: the Hubble diagram showing expansion, the abundance of elements in the Universe which agree with Big Bang Nucleosynthesis (BBN), and the relic radiation left over from approximately 380,000 years after the Big Bang – the cosmic microwave background (CMB). Since the Universe is currently expanding it must have been hotter and denser in the past. If we extrapolate all the way back in time, this would result in a singularity in which all of the laws of Physics break down.

After this time, approximately 10^{-35} seconds after the Big Bang, it is postulated that the Universe went through a period of exponential expansion called inflation. Inflation explains both the homogeneity of our current Universe on large scales and the origin of structure in our Universe, but is awaiting confirmation. In order to obtain structure in the late-time Universe (stars and galaxies) there must be perturbations from the smooth background evolution described above. Inflation is thought to provide the seeds of structure by turning quantum fluctuations in the early Universe into density perturbations on cosmological scales.

The energy density of the early Universe is dominated by radiation and hence $a \propto t^{1/2}$. At this point the Universe consists of a high energy plasma, a 'soup' of relativistic particles which are constantly being created and destroyed. As the Universe expands the temperature drops and particles begin to fall out of thermal equilibrium with the plasma – they decouple. Neutrinos decouple roughly 1 second after the Big Bang forming the cosmic neutrino background (see section 1.4). Big Bang nucleosynthesis occurred approximately 3 minutes after the Big Bang and saw the formation of light elements such as deuterium, helium and lithium.

Since the density of radiation falls as a^{-4} and the density of matter falls as a^{-3} roughly 40,000

years after the Big Bang (at z=3000) the Universe becomes matter dominated. The point of matter-radiation equality is significant as perturbations grow at different rates in the two eras. This impacts the development of the large-scale structure of the Universe and the CMB anisotropies. In the matter dominated era $a \propto t^{2/3}$.

During the matter-dominated era, 380,000 years after the Big Bang (at z=1100) recombination takes place. Recombination refers to when the temperature of the Universe is low enough for electrons and protons to form hydrogen. At this point photons decouple from matter as they are no longer repeatedly scattered off electrons, and can free stream. These photons form the CMB and carry an imprint of the small density fluctuations in the early Universe.

After recombination a period called the dark ages began. During this time the dark matter perturbations continued to grow, and to form the structure we see in our current Universe. This structure is referred to as the cosmic web, and consists of clusters of gravitationally-bound dark matter called halos connected together by filaments. Before recombination, baryons were prevented from falling into the dark matter potential wells by radiation pressure, but after recombination they begin to cluster. As the perturbations continued to grow they eventually became non-linear, and the pressure and temperature became great enough to form the first stars and galaxies. This epoch is called reionisation, as the neutral hydrogen formed during recombination is reionised, and while little is known about exactly when reionisation occurred it is an active area of research. These first stars and galaxies continued to evolve into larger galaxies and galaxy clusters. The distribution of galaxies that we see today is a key observable of large-scale structure cosmology. These galaxies are particularly useful as they trace the underlying distribution of dark matter.

Recently the Universe ceased to be matter dominated and became dominated by dark energy, or the cosmological constant. This began a period of exponential expansion ($a \propto e^{Ht}$), which continues to this day.

1.2 Structure

If the Universe only followed the background evolution detailed by General Relativity the structure in the Universe, which we see today, would not exist. Clearly there must be perturbations from this background. The key quantity used to describe these perturbations is the density contrast or

fractional density perturbation,

$$\delta(\boldsymbol{x}, t) = \frac{\rho(\boldsymbol{x}, t) - \bar{\rho}(t)}{\bar{\rho}(t)} \tag{1.16}$$

where $\bar{\rho}$ is the mean density of the Universe.

In this section we present the formalism for how the initial fractional density perturbations evolve into structure, particularly in relation to the dominant component of the Universe at the time. We then summarize the key statistics used to describe these perturbations, and detail two observational pillars of cosmology, the matter power spectrum and the CMB.

1.2.1 Perturbation Theory

The evolution of the small initial density perturbations into structure is fully described by relativistic perturbation theory (Dodelson, 2003; Weinberg, 2008). However, the evolution of cold dark matter is well approximated by Newtonian perturbation theory. Since the structure formed by dark matter is the focus of this thesis, and of cosmological surveys in general, Newtonian perturbation theory is presented here.

A smooth matter-dominated universe can be represented as a perfect fluid with energy/mass density ρ, pressure P ($\ll \rho$), velocity distribution $\boldsymbol{u}$ ($\ll c$) and gravitational potential Φ. The equations of motion of the fluid are: the continuity equation,

$$\frac{\partial \rho}{\partial t}\Big|_{\boldsymbol{r}} + \boldsymbol{\nabla}_{\boldsymbol{r}} \cdot (\rho \boldsymbol{u}) = 0 \; ; \tag{1.17}$$

Euler's equation,

$$\frac{\partial \boldsymbol{u}}{\partial t}\Big|_{\boldsymbol{r}} + \boldsymbol{u} \cdot \boldsymbol{\nabla}_{\boldsymbol{r}} \boldsymbol{u} = -\frac{1}{\rho} \boldsymbol{\nabla}_{\boldsymbol{r}} P - \boldsymbol{\nabla}_{\boldsymbol{r}} \Phi \; ; \tag{1.18}$$

and the Poisson equation,

$$\boldsymbol{\nabla}^2_{\boldsymbol{r}} \Phi = 4\pi G \rho \; . \tag{1.19}$$

The continuity equation describes the conservation of energy/mass, the Euler equation describes the motion of the fluid with respect to gravity and pressure, and the Poisson equation connects the gravitational potential to the energy density of the fluid.

Since the Universe is expanding it is convenient to convert these equations from physical

coordinates $\boldsymbol{r}$ into comoving spatial coordinates $\boldsymbol{x}$. Comoving coordinates expand with the universe and therefore remain constant for a comoving observer, whereas physical coordinates are scaled by the scale factor a, $\boldsymbol{r} = a(t)\boldsymbol{x}$. The derivatives are transformed as,

$$\begin{aligned}\left(\frac{\partial}{\partial t}\right)_{\boldsymbol{r}} &= \left(\frac{\partial}{\partial t}\right)_{\boldsymbol{x}} + \left(\frac{\partial \boldsymbol{x}}{\partial t}\right)_{\boldsymbol{r}} \cdot \boldsymbol{\nabla}_{\boldsymbol{x}} \\ &= \left(\frac{\partial}{\partial t}\right)_{\boldsymbol{x}} - H(t)\boldsymbol{x} \cdot \boldsymbol{\nabla}_{\boldsymbol{x}} \ ,\end{aligned} \tag{1.20}$$

where in the second line we have used $\boldsymbol{x} = \boldsymbol{r}/a(t)$ and $H(t) = \dot{a}/a$; and

$$\boldsymbol{\nabla}_{\boldsymbol{r}} = a^{-1}\boldsymbol{\nabla}_{\boldsymbol{x}} \ . \tag{1.21}$$

We can now introduce perturbations around the background evolution,

$$\begin{aligned}&\rho \to \bar{\rho}(t) + \delta\rho \equiv \bar{\rho}(t)(1 + \delta(\boldsymbol{x}, t)) \\ &P \to \bar{P}(t) + \delta P(\boldsymbol{x}, t) \\ &\boldsymbol{u} \to a(t)H(t)\boldsymbol{x} + \boldsymbol{v}_p(\boldsymbol{x}, t) \\ &\Phi \to \bar{\Phi}(\boldsymbol{x}, t) + \phi(\boldsymbol{x}, t) \ .\end{aligned} \tag{1.22}$$

Here, $\bar{\rho}$ is the mean density and $\delta\rho$ is a small perturbation to the mean density, $\bar{P}$ is the mean pressure and δP is a small perturbation to the mean pressure, $\boldsymbol{v}_p$ is the peculiar velocity which describes deviations from the general expansion velocity, and $\bar{\Phi}$ is the mean gravitational potential and ϕ is a small perturbation to the mean gravitational potential.

Inserting these perturbations into the equations of motion above and keeping only the linear terms leaves,

$$\begin{aligned}&\dot{\delta} + \frac{1}{a}\boldsymbol{\nabla} \cdot \boldsymbol{v_p} = 0 \\ &\dot{\boldsymbol{v}}_{\boldsymbol{p}} + H\boldsymbol{v_p} = -\frac{1}{a\bar{\rho}}\boldsymbol{\nabla}\delta P - \frac{1}{a}\boldsymbol{\nabla}\phi \\ &\boldsymbol{\nabla}^2\phi = 4\pi G a^2 \bar{\rho}\delta \ ,\end{aligned} \tag{1.23}$$

where the derivatives are with respect to the comoving coordinates.

Taking the time derivative of the perturbed continuity equation and combining it with the

perturbed Euler and Poisson equations gives,

$$\ddot{\delta} + 2H\dot{\delta} - \frac{c_s^2}{a^2}\boldsymbol{\nabla}^2\delta - 4\pi G\bar{\rho}\delta = 0 \ , \tag{1.24}$$

where $c_s = \sqrt{\partial P/\partial\rho}$ is the sound speed. This equation describes the evolution of density perturbations δ in an expanding universe. It can be simplified by converting to Fourier space,

$$\ddot{\delta} + 2H\dot{\delta} + \left(\frac{c_s^2 k^2}{a^2} - 4\pi G\bar{\rho}\right)\delta = 0 \ , \tag{1.25}$$

where δ is a function of wavenumber $\boldsymbol{k}$ instead of comoving coordinate $\boldsymbol{x}$. We now examine the behaviour of density perturbations in the different phases of the Universe; radiation dominated, matter dominated and dark energy dominated.

Radiation-Dominated Universe

During radiation domination the Universe cannot be described by a single fluid, which has been assumed in this analysis. However, using the information from relativistic perturbation theory: that the density contrast of radiation is negligible (radiation provides a smooth background[1]); and that during radiation domination $\rho_{\rm r} \gg \rho_{\rm m}$ and $a \propto t^{1/2}$ equation 1.25 reduces to,

$$\ddot{\delta_{\rm c}} + \frac{1}{t}\dot{\delta_{\rm c}} = 0 \ , \tag{1.26}$$

where the subscript $\rm c$ indicates this equation applies specifically to cold dark matter. The solutions are $\delta_{\rm c} = \text{const}$ and $\delta_{\rm c} \propto \ln t$, so dark matter perturbations do not grow or only grow very slowly during radiation domination.

Matter-Dominated Universe

When the Universe is matter dominated (after matter-radiation equality but before dark energy domination) it can be described by an Einstein de-Sitter universe where $\Omega_{\rm m} = 1$ and $\Omega_\Lambda = 0$. In a matter dominated universe $a \propto t^{2/3}$ and equation 1.25 reduces to,

$$\ddot{\delta}_{\rm m} + \frac{4}{3t}\dot{\delta}_{\rm m} - \frac{2}{3t^2}\delta_{\rm m} = 0 \ , \tag{1.27}$$

[1]This is true for scales smaller than the horizon (smaller than the visible Universe) after time averaging the baryonic acoustic oscillations.

where the suffix m emphasizes that this equation refers to matter perturbations (cold dark matter + baryons), and we have taken $c_s^2 = 0$. This equation has two solutions $\delta_\mathrm{m} \propto t^{-1}$ and $\delta_\mathrm{m} \propto t^{2/3} \propto a$. In contrast, in a static universe $\dot{a} = 0$ and the $\dot{\delta}$ term in equation 1.25 disappears, resulting in an exponentially growing solution. In an expanding universe perturbations grow with a power law dependence, whereas in a static universe perturbations grow exponentially – expansion slows the growth of matter perturbations.

Dark Energy Dominated Universe

At late times the Universe is dark energy dominated and $a \propto e^{Ht}$. In this case equation 1.25 reduces to,

$$\ddot{\delta}_\mathrm{m} + 2H\dot{\delta}_\mathrm{m} \approx 0 \ , \tag{1.28}$$

where the approximation becomes an equality as $\Omega_\Lambda \to 1$. In this case the solutions are $\delta_\mathrm{m} = \mathrm{const}$ and $\delta_\mathrm{m} \propto e^{-2Ht} \propto a^{-2}$, so dark energy suppresses the growth of structure.

Perturbations Larger than the Horizon

Until now we have been considering perturbations which are smaller than the visible Universe, but very large perturbations evolve differently. A useful quantity in this context is the Hubble radius, $r_\mathrm{H}(t_0) = c/H(t_0)$. The Hubble radius defines a sphere around the observer at the present time, beyond which objects are receding from the observer faster than the speed of light. The Hubble radius can be defined as an apparent horizon, where perturbations larger than the horizon are not observable and perturbations within the horizon are observable.

We can determine how perturbations larger than the horizon grow by considering two patches of universe; one which is flat with density ρ, and one which is outside the apparent horizon of the first and has curvature κ and density ρ_1. If we define the patches as having the same Hubble parameter we can equate the Friedmann equations as,

$$\frac{8\pi G}{3}\rho = \frac{8\pi G}{3}\rho_1 - \frac{\kappa c^2}{a^2} \ , \tag{1.29}$$

and rearrange to find,

$$\rho_1 - \rho = \frac{3}{8\pi G}\frac{\kappa c^2}{a^2} \ , \tag{1.30}$$

dividing by ρ gives,

$$\delta \propto \frac{1}{a^2 \rho} \, . \tag{1.31}$$

This classical result is confirmed by relativistic perturbation theory, but is gauge dependent (Dodelson, 2003; Weinberg, 2008). Perturbations to the metric can be expressed in multiple different coordinate systems, or choices of gauge. This result is valid for the synchronous gauge. It tells us that during radiation domination when $\rho \propto a^{-4}$ perturbations on scales larger than the horizon grow as $\delta \propto a^2$, and during matter domination when $\rho \propto a^{-3}$ they grow as $\delta \propto a$. In a matter dominated universe perturbations within and outside of the horizon grow proportional to the scale factor, whereas in a radiation dominated universe perturbations outside the horizon grow as a^2 and perturbations inside the horizon do not grow.

Non-linear Pertubations

The linear perturbation theory equations above only apply to small perturbations and break down once $\delta \sim 1$. The formation of stars, galaxies and galaxy clusters are all highly non-linear and there are only approximate solutions, such as the spherical collapse model (Mo et al., 2010). This non-linear growth is therfore usually modelled using large numerical simulations (Schneider, 2015).

1.2.2 Density Statistics

To understand the structure in the Universe we need to be able to describe the statistics of the density fluctuations. By definition the mean is zero,

$$\langle \delta(\boldsymbol{x}, t) \rangle = 0 \, , \tag{1.32}$$

where angle-brackets denote the ensemble average for all $\boldsymbol{x}$. Instead these density fluctuations are described by their second moment, the variance,

$$\langle \delta(\boldsymbol{x}, t) \delta(\boldsymbol{y}, t) \rangle = \xi(\boldsymbol{x}, \boldsymbol{y}, t) = \xi(|\boldsymbol{x} - \boldsymbol{y}|, t) \, , \tag{1.33}$$

where ξ denotes the correlation function. ξ can be written as a function of the separation between positions $\boldsymbol{x}$ and $\boldsymbol{y}$ because the density fluctuations are statistically homogeneous and isotropic and exist on a homogeneous and isotropic background. Another commonly used quantity is the Fourier

transform of the correlation function – the power spectrum. If the Fourier transform of the density contrast is,

$$\tilde{\delta}(\boldsymbol{k}, t) = \int \mathrm{d}^3x \; e^{-i\boldsymbol{k}\cdot\boldsymbol{x}} \delta(\boldsymbol{x}, t) \; , \tag{1.34}$$

then the variance in Fourier space is given by,

$$\langle \tilde{\delta}(\boldsymbol{k}) \tilde{\delta}(\boldsymbol{k'}) \rangle = (2\pi^3) \delta^{(3)}(\boldsymbol{k} + \boldsymbol{k'}) P(k) \tag{1.35}$$

where $\delta^{(3)}$ is the three-dimensional Dirac delta function and $P(k)$ is the power spectrum. The power spectrum describes the 'clumpiness' of the universe as a function of scale. The power spectrum is particularly powerful, as for a Gaussian distribution of density fluctuations it completely describes the matter density distribution.

1.2.3 Matter Power Spectrum

As mentioned previously, the initial tiny perturbations from the background universe come from quantum fluctuations amplified by inflation. However, not only does inflation provide the origin of these fluctuations, it provides a prediction for the power spectrum of these initial fluctuations,

$$P_0(k) = A_s k^{n_s - 1} \; . \tag{1.36}$$

P_0 is the dimensionless primordial power spectrum, A_s is the amplitude of the primordial fluctuations and n_s is the scalar spectral index. n_s depends on the properties of the scalar field driving inflation. The particular case of $n_s = 1$ is referred to as the Harrison-Zeldovich power spectrum.

The power spectrum observed by large galaxy surveys is the late-time matter power spectrum. The late-time power spectrum can be connected to the primordial power spectrum as so,

$$P(k, t) = T^2(k) D^2(t) P_0(k) \; . \tag{1.37}$$

$D(t)$ is the growth factor and summarises how the initial perturbations grow with time. The spatial and time dependencies can be separated because the Universe in homogeneous. $T(k)$ is the transfer function, which summarises how matter perturbations grow differently depending on the dominant component of the universe and their size. In section 1.2.1 we approximated how matter perturbations grow by assuming the Universe could be described by a single pressure-less

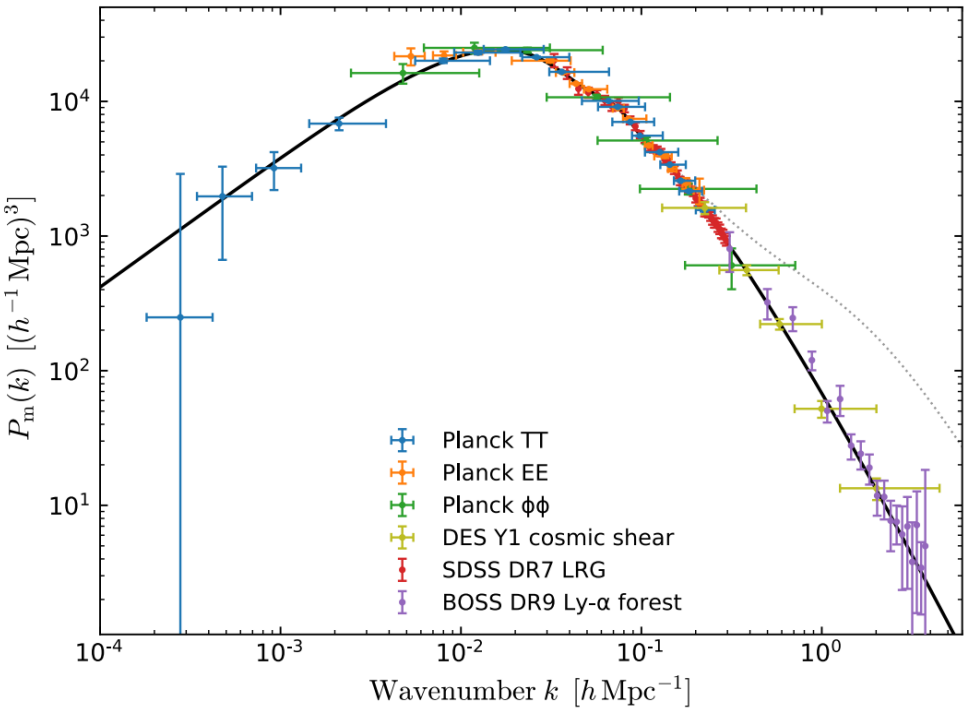

Figure 1.1: Compliation of measurements of the linear matter power spectrum at $z = 0$, from the CMB (Aghanim et al., 2018), galaxy clustering (Reid et al., 2010), the Lyman-alpha forest (Palanque-Delabrouille et al., 2015) and weak lensing cosmic shear (Troxel et al., 2018). The level of agreement with the model (black line) from a variety of cosmological probes shows the power of the ΛCDM model. The dotted line shows the effect of non-linear clustering at $z = 0$. Figure from: Akrami et al. (2018).

fluid. This helps to give intuition about how perturbations grow, but clearly the Universe has multiple components. The Boltzmann equations describe how each of these components evolves with time, and the Einstein-Boltzmann equations describe how the metric evolves with respect to these components (Dodelson, 2003; Weinberg, 2008). The transfer function is therefore computed by numerically solving the Einstein-Boltzmann equations.

Figure 1.1 shows the linear matter power spectrum at $z = 0$ predicted by the ΛCDM model compared to various measurements from the CMB (Aghanim et al., 2018), galaxy clustering (Reid et al., 2010), the Lyman-alpha forest (Palanque-Delabrouille et al., 2015) and weak lensing cosmic shear (Troxel et al., 2018). The overlap of the measurements on vastly different scales with the prediction illustrates the power of the ΛCDM model. The location of the turn-over is given by the size of the horizon at matter-radiation equality $k_{\rm eq}$. Perturbations with $k < k_{\rm eq}$ are larger than the horizon at matter-radiation equality and only enter the horizon during matter domination.

They have therefore grown as a^2 during radiation domination and as a during matter domination. Perturbations with $k > k_{\rm eq}$ are smaller than the horizon at matter-radiation equality and enter the horizon during radiation domination. Initially they grow as a^2, then their growth is ceased when they enter the horizon, until they being to grow again as a during matter domination. The growth of small scale perturbations is therefore suppressed compared to larger ones. The power spectrum takes the form of the primordial power spectrum on large scales $P \propto k^{n_s}$ where $n_s \approx 1$, and the scaling is reduced on small scales.

The other key feature of the linear matter power spectrum are the wiggles present to the right of the turnover in Fig, 1.1. Before recombination baryons and photons are tightly coupled. This means that after matter-radiation equality the dark matter perturbations begin to grow but the baryons continue to oscillate with the radiation. After recombination the baryons decouple from the photons, but the oscillations freeze into the baryon distribution. These are referred to as baryonic acoustic oscillations (BAO), as their scale is set by the sound speed in the baryon-photon plasma at recombination, and they show up as wiggles in the Fourier space matter power spectrum.

Since dark matter is not directly observable the large-scale structure probes in Fig. 1.1 use tracers of the dark matter distribution, such as galaxies. While baryon perturbations tend to mirror the dark matter perturbations in the late-time Universe, the complex physics of galaxy formation means that galaxies are not perfect tracers of the underlying dark matter distribution. Large-scale structure probes that utilise galaxies as tracers are therefore really measuring the galaxy power spectrum P_{gg}, not the matter power spectrum $P_{\delta\delta}$. The galaxy power spectrum is often related to the matter power spectrum using a multiplicative bias factor b_g where

$$P_{gg} = b_g^2 P_{\delta\delta} \ . \tag{1.38}$$

This relation works well on linear scales but breaks down on small scales where the perturbations become non-linear. The precision of large-scale surveys is reaching the point where this relation is not sufficient, so alternative approaches are being explored. One particular approach often referred to as the 'halo model' is discussed in section 3.3.2.

1.2.4 CMB

The CMB currently gives us the earliest picture of the inhomogeneous Universe. The photons in the CMB last scattered off electrons approximately 380.000 years after the Big Bang and have since travelled freely through space. The presence of this relic radiation provides key evidence that the

Universe was once hotter and denser, and measurements of the CMB anisotropies established the ΛCDM model of cosmology. The first measurements of the CMB found an almost perfect blackbody spectrum with temperature 2.7 K, and showed that the early Universe was extremely smooth (Mather et al., 1994; Smoot et al., 1992). It was only with higher precision measurements from satellites such as WMAP (Bennett et al., 2013) and *Planck* (Aghanim et al., 2018), that the tiny fluctuations in this temperature spectrum were observed.

Figure 1.2 shows a compilation of recent CMB angular power spectrum measurements from satellite experiments such as WMAP and *Planck*, to ground-based experiments such as the Atacama Cosmology Telescope (ACT) (Aiola et al., 2020) and the South Pole Telescope (SPT) (George et al., 2015), which focus on small scales. The top panel shows the power spectrum of the temperature, and E-mode and B-mode polarization signals; the middle panel the cross-correlation spectrum between temperature and E-mode polarization; and the lower panel shows the CMB lensing power spectrum. The ΛCDM prediction using the best-fit values from *Planck* is shown by the dashed grey line (Aghanim et al., 2018). There is remarkable agreement between the theory and the data across a wide range of scales.

Specifically, these observations are described by a spatially flat six parameter ΛCDM model, and there is no compelling evidence for extending this model (Aghanim et al., 2018). The *Planck* best fit parameters and their associated 1σ uncertainties are: the dark matter density $\Omega_c h^2 = 0.120 \pm 0.001$, the baryon density $\Omega_b h^2 = 0.0224 \pm 0.0001$, the amplitude of primordial fluctuations $\ln(10^{10} A_s) = 3.044 \pm 0.014$, the scalar spectral index $n_s = 0.965 \pm 0.004$, the optical depth due to Thomson scattering at the time of reionisation[2] $\tau = 0.054 \pm 0.007$ and the angular size of the sound horizon[3] at recombination $100\theta_* = 1.0411 \pm 0.0003$. Assuming these early universe parameters it is possible to infer the late-time parameters: the Hubble constant $H_0 = (67.4 \pm 0.5)\mathrm{km\ s^{-1}Mpc^{-1}}$; the matter density parameter $\Omega_m = 0.315 \pm 0.007$; and the amplitude of matter fluctuations in $8h^{-1}$ Mpc spheres $\sigma_8 = 0.811 \pm 0.006$ [4].

There is currently some tension between the late-time measurements inferred by *Planck* and the values measured directly by large-scale structure experiments. Observations of Type 1a supernovae, where the distances are calibrated using Cepheid variable stars, find $H_0 = 74.03 \pm 1.42 \mathrm{km\ s^{-1}Mpc^{-1}}$, a 4.4σ discrepancy with *Planck* (Riess et al., 2019). Weak Lensing surveys find a small tension with σ_8 and Ω_m (see section 1.3.2). These tensions could be caused by new physics, or by systematic

[2] A larger value of τ approximately corresponds with an earlier onset of star and galaxy formation, and $\tau = 0$ implies no reionisation.

[3] The sound horizon is the distance sound could travel from t=0 until recombination when the CMB is formed.

[4] The choice of $8h^{-1}$ Mpc spheres for σ_8 is a convention from early measurements of galaxy power spectra, where the amplitude was found to be roughly one on scales of $8h^{-1}$ Mpc.

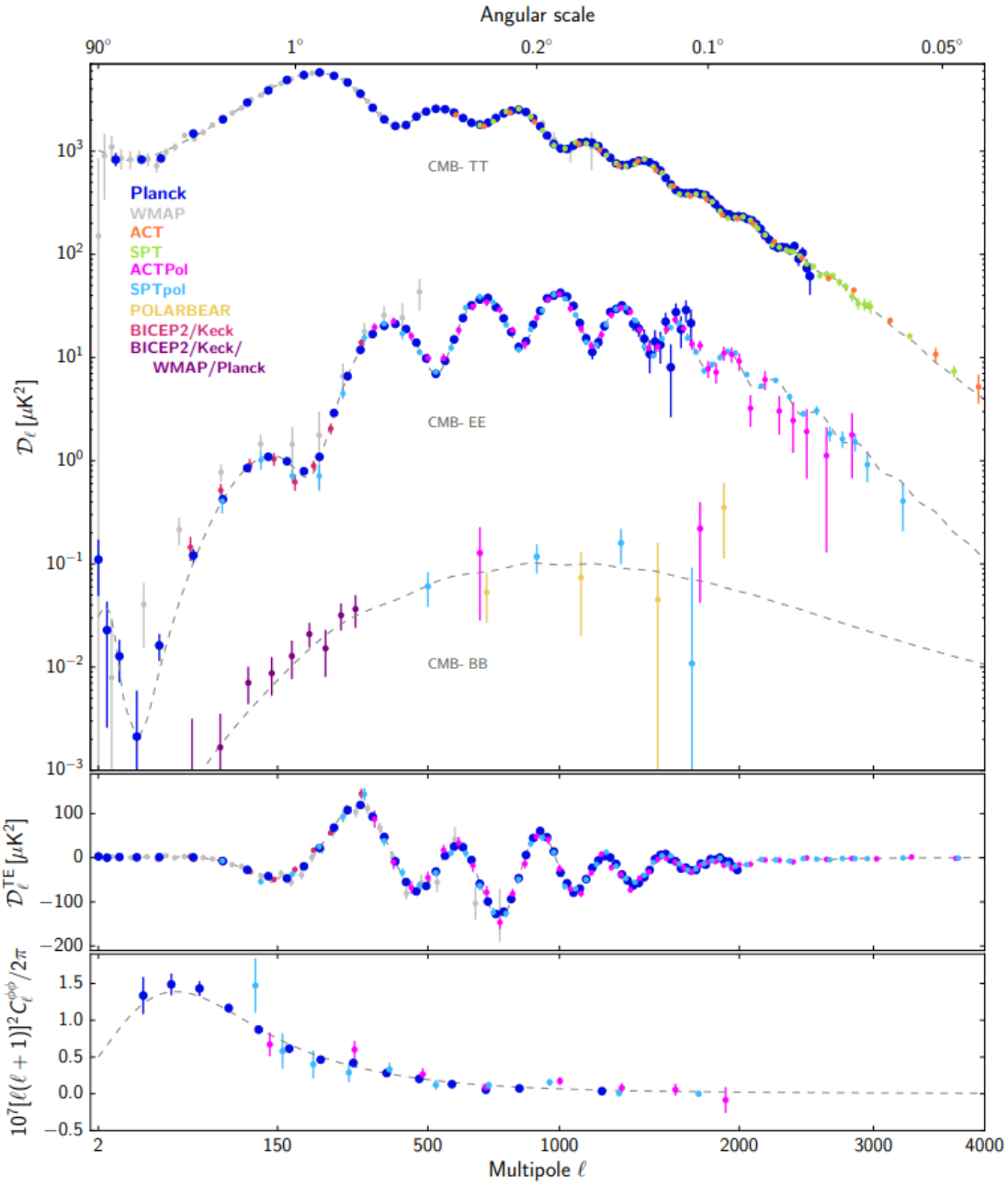

Figure 1.2: Compilation of recent CMB angular power spectrum measurements. The upper panel shows the temperature and E and B mode polarization power spectra; the middle panel shows the cross correlation spectrum between temperature and E mode polarization; and the lower panel shows the lensing deflection power spectrum. Figure from: Akrami et al. (2018).

uncertainties in any of the measurements.

1.3 Weak Lensing

Light travelling from distant galaxies is deflected gravitationally by matter along its path. This means that galaxy images appear distorted. When the deflection is large this can result in multiple images of the same galaxy, the galaxy image smeared into arcs or in the case of perfect alignment the galaxy image can be distorted into a ring. This scenario is referred to as strong gravitational lensing. When the deflection is small, as in most cases, the shapes and sizes of the galaxy images are distorted so little as to be unobservable to the naked eye. However, these minute distortions can be measured statistically and their correlations directly related to the matter power spectrum. This scenario is referred to as weak gravitational lensing.

Weak gravitational lensing is a key probe of the late-time matter distribution in our Universe. It is particularly interesting because it probes the distribution of mass, not the distribution of baryons like most other large scale structure probes. As such, weak lensing will form part of the core analysis of upcoming large-scale galaxy surveys, such as the Vera Rubin Observatory Legacy Survey of Space and Time (LSST) (LSST Science Collaboration, 2009) and *Euclid* (Laureijs et al., 2011).

In this section we summarize the theory of weak lensing and then we discuss the current status of weak lensing measurements. Then in chapter 3 we explore how an often neglected part of weak lensing, weak lensing magnification, can affect the cosmological parameter constraints obtained by LSST. This section relies on a number of reviews of weak lensing; Bartelmann and Schneider (2001), Munshi et al. (2008), Bartelmann (2010), Kilbinger (2015) and Bartelmann and Maturi (2016).

1.3.1 Theory

Lensing Potential for a Thin Lens

We begin by finding the lensing potential ψ for a thin lens, where the line-of-sight distribution of matter forming the lens is thin, compared to the overall distance between the source galaxy and the observer. The lensing potential summarises the imaging properties of the lens and is a key quantity in weak gravitational lensing.

Figure 1.3 shows the orientation of the thin lens system with the observer marked by O, the true location of the galaxy marked by S and the location of the galaxy image marked by I. The thin lens

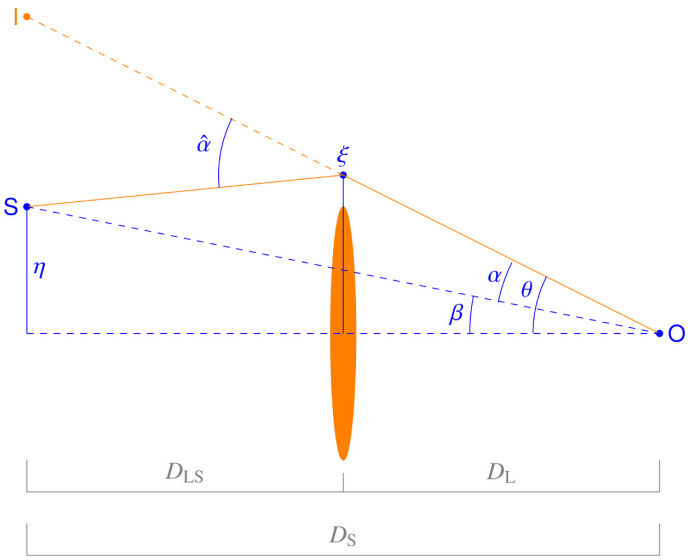

Figure 1.3: The set up of a thin lens system. The observer is located at O, the source galaxy is located at S and the image of the galaxy appears at I. D_L is the distance between the observer and the lens, D_S the distance between the observer and the source and D_{LS} is the distance between the lens and the source. Figure from: Bartelmann and Maturi (2016).

assumption allows the light paths to be marked by straight lines. The angular position of the source from the observers point of view $\boldsymbol{\beta}$ can be related to the angular position of the image from the observers point of view $\boldsymbol{\theta}$, and the deflection angle of the light ray $\hat{\boldsymbol{\alpha}}$ by,

$$\boldsymbol{\beta} = \boldsymbol{\theta} - \frac{D_{LS}}{D_S}\hat{\boldsymbol{\alpha}} \equiv \boldsymbol{\theta} - \boldsymbol{\alpha} \,, \tag{1.39}$$

where D_{LS} is the distance between the lens and the source, D_S is the distance to the source and we have defined the reduced deflection angle $\boldsymbol{\alpha}$. This equation is the lens equation.

The deflection angle with respect to the light ray $\hat{\boldsymbol{\alpha}}$ can be calculated from the perturbed metric[5];

$$ds^2 = \left(1 + \frac{2\Phi}{c^2}\right)c^2dt^2 - a^2(t)\left(1 - \frac{2\Phi}{c^2}\right)\left[\frac{dr^2}{1-\kappa r^2} + r^2 d\Omega^2\right] \,, \tag{1.40}$$

where once again $d\Omega^2 = d\theta^2 + \sin^2\theta d\phi^2$, and the gravitational potential Φ represents a perturbation to the FLRW metric. Employing Fermat's principle of least time, which states that a light ray takes the path between two points that can be traversed in the least time, gives the deflection angle of the

[5]Perturbations to the metric can be expressed in multiple different coordinate systems, or choices of gauge. This perturbed metric is defined in the conformal Newtonian gauge.

light ray in terms of the gravitational potential Φ,

$$\hat{\boldsymbol{\alpha}} = \frac{2}{c^2} \int \boldsymbol{\nabla}_\perp \Phi \, \mathrm{d}\lambda \, , \tag{1.41}$$

where the gradient is perpendicular to the light ray, and the integral is along the light ray in terms of distance $\mathrm{d}\lambda$. This gives the deflection angle from the observer's point of view,

$$\boldsymbol{\alpha} = \boldsymbol{\nabla}_\perp \left[\frac{2}{c^2} \frac{D_{LS}}{D_S} \int \Phi \, \mathrm{d}z \right] , \tag{1.42}$$

where the integral along the light ray is now in terms of distance z. This expression employs the Born approximation where the integration path along the light ray is approximated as a straight line. This approximation relies on the deflection angle of the light ray being very small. In weak lensing it is more useful to discuss the positions of sources and images in terms of their angular positions $\boldsymbol{\theta}$ on the sky, not perpendicular distances. We therefore convert the gradient $\boldsymbol{\nabla}_\perp \rightarrow D_L^{-1} \boldsymbol{\nabla}_\theta$ and find,

$$\begin{aligned} \boldsymbol{\alpha} =& \boldsymbol{\nabla}_\theta \left[\frac{2}{c^2} \frac{D_{LS}}{D_L D_S} \int \Phi \, \mathrm{d}z \right] \\ =:& \boldsymbol{\nabla}_\theta \psi \, , \end{aligned} \tag{1.43}$$

where we have defined the lensing potential ψ.

Convergence and Shear Related to the Lensing Potential

If we assume that the source is much smaller than the typical scale of variations in the deflection angle, we can relate the extent of the source $\delta\boldsymbol{\beta}$ to the extent of the image $\delta\boldsymbol{\theta}$ by linearising the lens equation,

$$\delta\boldsymbol{\beta} \approx \mathcal{A} \, \delta\boldsymbol{\theta}, \tag{1.44}$$

where $\mathcal{A}$ describes the linear mapping between the source and the image. $\mathcal{A}$ is defined as,

$$\mathcal{A}_{ij} = \frac{\partial \beta_i}{\partial \theta_j} = \delta_{ij} - \frac{\partial^2 \psi}{\partial \theta_i \partial \theta_j} = \delta_{ij} - \psi_{ij} \, , \tag{1.45}$$

where we have introduced the notation ψ_{ij} for the second derivatives of the lensing potential ψ. This equation states that the mapping between the source and the image is dependent on the curvature of the lensing potential; without a lensing potential the mapping is the identity. This

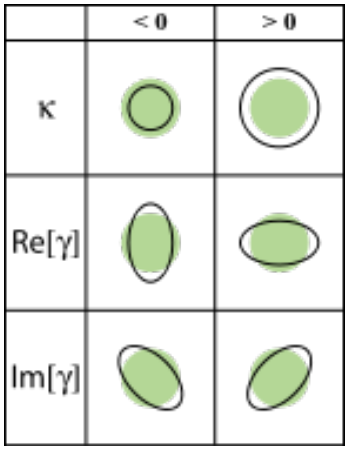

Figure 1.4: The distortion effect of convergence κ and complex shear γ on a circular image.

mapping between the source and the image is a foundation of weak lensing.

The matrix $\mathcal{A}$ is often parametrised in terms of the convergence κ and the shear γ,

$$\mathcal{A} = \begin{pmatrix} 1-\kappa-\gamma_1 & -\gamma_2 \\ -\gamma_2 & 1-\kappa+\gamma_1 \end{pmatrix} \tag{1.46}$$

where $\gamma = \gamma_1 + \mathrm{i}\gamma_2$. The distortion effect caused by κ and γ is shown in Fig. 1.4. κ is associated with a change in solid angle, referred to as weak lensing magnification, and γ with a change in shape referred to as gravitational shear. This parametrisation of $\mathcal{A}$ defines the convergence and shear in relation to the curvature of the lensing potential as,

$$\begin{aligned} \kappa &= \frac{1}{2}(\psi_{11}+\psi_{22}) = \frac{1}{2}\nabla^2\psi \\ \gamma_1 &= \frac{1}{2}(\psi_{11}-\psi_{22}) \\ \gamma_2 &= \psi_{12}\ . \end{aligned} \tag{1.47}$$

In reality we have the images of the galaxies and we want to infer the source extent $\delta\boldsymbol{\beta}$ from the image extent $\delta\boldsymbol{\theta}$,

$$\delta\boldsymbol{\theta} = \mathcal{A}^{-1}\delta\boldsymbol{\beta}\ . \tag{1.48}$$

In the weak lensing regime κ and γ are much smaller than 1, so the images of source galaxies are only mildly distorted. This means that the matrix $\mathcal{A}$ is invertible because the source can be mapped

to a single image, which is not the case for strong lensing where multiple images can be produced. The inverse of $\mathcal{A}$ is given by,

$$\mathcal{A}^{-1} = \frac{1}{\det\mathcal{A}} \begin{pmatrix} 1-\kappa+\gamma_1 & \gamma_2 \\ \gamma_2 & 1-\kappa-\gamma_1 \end{pmatrix} , \tag{1.49}$$

where the prefactor $1/\det\mathcal{A}$ defines the change in the size of the image compared to the size of the source, the magnification μ. In the weak lensing regime μ is given by,

$$\mu = \frac{1}{\det\mathcal{A}} = \frac{1}{(1-\kappa)^2-\gamma^2} \approx 1+2\kappa . \tag{1.50}$$

The magnification is determined by the convergence, and not the shear, in weak lensing.

Lensing Potential and Convergence for an Extended Lens

Clearly assuming a thin lens is not appropriate for gravitational lensing by the large-scale structure of the universe. The light ray from the source galaxy is continually distorted as it travels towards the observer. To convert the lensing potential for a thin lens (eq. 1.43) to the lensing potential for an extended lens, a flat universe is assumed, and the distances are replaced by radial comoving distances and brought within the integral,

$$\psi(\boldsymbol{\theta}) = \frac{2}{c^2}\int_0^{\chi_S} \mathrm{d}\chi \frac{\chi_S-\chi}{\chi_S\chi}\Phi(\chi^{\boldsymbol{\theta}},\chi) , \tag{1.51}$$

where χ is the comoving radial coordinate, χ_S is the comoving distance to the source and $\chi^{\boldsymbol{\theta}}$ is a position perpendicular to the line of sight (Bartelmann and Maturi, 2016).

We can then calculate the convergence κ from the lensing potential using the relation in eq. 1.47 and the Poisson equation,

$$\nabla^2\Phi = 4\pi G a^2\bar{\rho}\delta , \tag{1.52}$$

where a is the scale factor, $\bar{\rho}$ is the mean matter density and δ is the density contrast, defined in section 1.2. This gives a convergence,

$$\kappa = \frac{4\pi G}{c^2}\int_0^{\chi_S} \mathrm{d}\chi \frac{\chi(\chi_S-\chi)}{\chi_S} a^2\bar{\rho}\delta(\chi) . \tag{1.53}$$

The mean matter density $\bar{\rho}$ in terms of the cosmological parameters is,

$$\bar{\rho} = \bar{\rho}_0 a^{-3} = \frac{3H_0^2}{8\pi G}\Omega_m a^{-3} \,, \tag{1.54}$$

so in terms of the cosmological parameters the convergence of an extended lens is given by,

$$\kappa = \frac{3}{2}\frac{H_0^2}{c^2}\Omega_m \int_0^{\chi_S} \mathrm{d}\chi \frac{\chi(\chi_S - \chi)}{\chi_S}\frac{\delta(\chi)}{a} \,. \tag{1.55}$$

Convergence Power Spectrum

The actual matter distribution along the line of sight is unknown so instead weak lensing looks at correlations between the convergence κ. These correlations show the scales at which there is structure in the universe. Assuming the Universe is homogeneous and isotropic on large scales the two-point convergence correlation function, in Fourier space, is related to the convergence power spectrum by,

$$\langle \tilde{\kappa}(\boldsymbol{\ell})\tilde{\kappa}^*(\boldsymbol{\ell'})\rangle = (2\pi)^2\delta^{(2)}(\boldsymbol{\ell} - \boldsymbol{\ell'})C_\kappa(\ell) \,, \tag{1.56}$$

where $\tilde{\kappa}$ is the Fourier transform of the convergence, $\boldsymbol{\ell}$ is the two-dimensional (2D) wave vector, $\delta^{(2)}$ is the 2D Dirac delta function and C_κ is the 2D convergence power spectrum [6]

The Limber approximation (Kaiser, 1992) states that if a 2D quantity $x(\boldsymbol{\theta})$ is a projection of 3D quantity $y(\boldsymbol{r})$,

$$x(\theta) = \int_0^{\chi_S} \mathrm{d}\chi w(\chi) y(\chi^{\boldsymbol{\theta}}, \chi) \,, \tag{1.57}$$

where $w(\chi)$ is a weight function, then the angular power spectrum of x is given by,

$$C_x(\ell) = \int_0^{\chi_S} \mathrm{d}\chi \frac{w^2(\chi)}{\chi^2} P_y\left(k = \frac{\ell + 1/2}{\chi}\right) \,, \tag{1.58}$$

where C_x denotes the 2D angular power spectrum and P_y denotes the 3D power spectrum at 3D wave number k. This approximation is valid as long as y varies on length scales much smaller than the scale of weight function. This approximation is often used to calculate weak lensing power spectra, where x is κ or γ.

By inspection we can see that equation 1.55 relates the convergence to the 3D density contrast δ

[6] This expression also assumes the flat-sky approximation (e.g. Lemos et al. 2017).

via a weight function. We can therefore relate the convergence power spectrum C_κ to the matter power spectrum P_δ using equations 1.56 and 1.58 to give,

$$C_\kappa(\ell) = \frac{9}{4}\left(\frac{H_0}{c}\right)^4 \Omega_m^2 \int_0^{\chi_S} \mathrm{d}\chi \left(\frac{\chi_S - \chi}{\chi_S a}\right)^2 P_{\delta\delta}\left(\frac{\ell + 1/2}{\chi}, \chi\right) . \tag{1.59}$$

For further details see the reviews referenced at the beginning of this section.

Shear Power Spectrum

The convergence power spectrum can only be directly measured using the apparent sizes or number density of galaxies, which can be challenging. It is therefore more common to measure the shear power spectrum using the ellipticities of galaxies (see chapter 3). However, the 2D shear angular power spectrum C_γ is equivalent to the convergence power spectrum, $C_\gamma = C_\kappa$. This can be demonstrated by converting eq. 1.47 to Fourier space,

$$\begin{aligned} \tilde{\kappa} &= -\frac{1}{2}(l_1^2 + l_2^2)\tilde{\psi} \, , \\ \tilde{\gamma_1} &= -\frac{1}{2}(l_1^2 - l_2^2)\tilde{\psi} \, , \\ \tilde{\gamma_2} &= -l_1 l_2 \tilde{\psi} \, , \end{aligned} \tag{1.60}$$

where tilde denotes the Fourier transform. We can equate the shear and convergence as follows,

$$4\tilde{\gamma}^2 = 4(\tilde{\gamma_1}^2 + \tilde{\gamma_2}^2) = \left[(l_1^2 - l_2^2)^2 + 4l_1^2 l_2^2\right]\tilde{\psi}^2 = (l_1^2 + l_2^2)^2 \tilde{\psi}^2 = 4\tilde{\kappa}^2 \, . \tag{1.61}$$

1.3.2 Current Status

Three current weak lensing surveys are the Kilo Degree Survey (KiDS), the Dark Energy Survey (DES) and the Hyper Suprime-Cam Survey (HSC). Their most recent cosmic shear results are detailed in Hildebrandt et al. (2020), Troxel et al. (2018) and Hikage et al. (2019). Figure 1.5 shows a plot of the combined constraints from KiDS and DES in the $S_8 \equiv \sigma_8 \sqrt{\Omega_m / 0.3}$ vs. Ω_m plain. The parameter combination S_8 is used because it is the parameter most tightly constrained by weak lensing, due to the degeneracy between Ω_m and σ_8. Ω_m determines the position of the matter radiation equality, the scale where the matter power spectrum turns over, and σ_8 determines the amplitude of the spectrum. Therefore, if the shape of the power spectrum does not change, Ω_m and σ_8 can compensate for each other's effects. The combined results (in pink) have a 2.5σ discrepancy with the *Planck* results assuming ΛCDM (in orange). While this tension is not particularly large, it

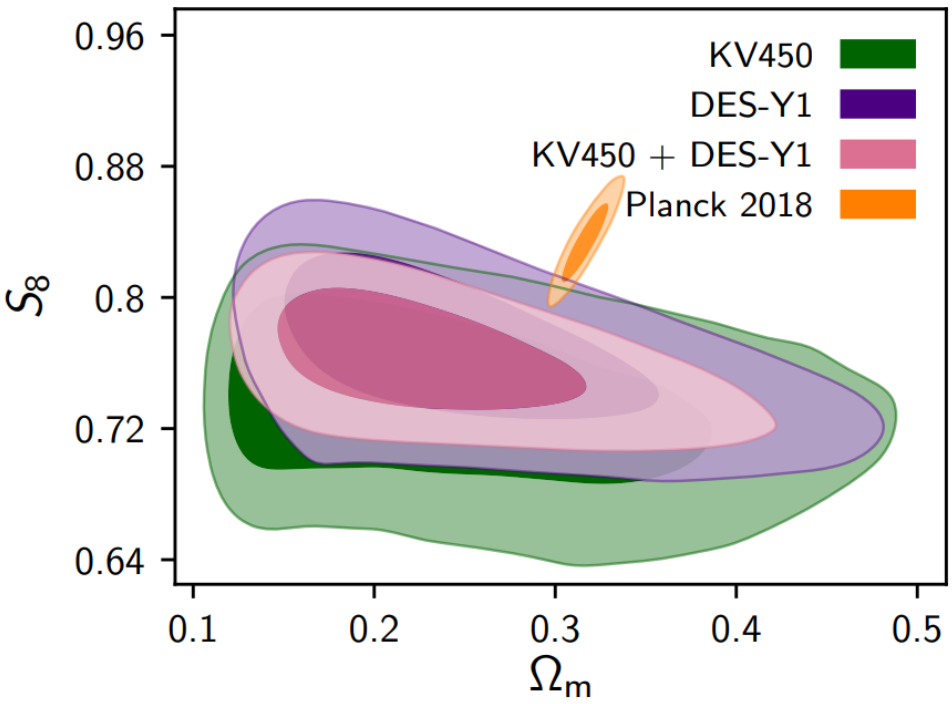

Figure 1.5: Constraints in the S_8-Ω_m plane, which weak lensing is particularly sensitive to (inner contour is 68% CL, outer contour is 95% CL). The weak lensing results from KiDS are labelled KV450 and shown in green, the weak lensing results from DES are labelled DES-Y1 and shown in purple, the combined weak lensing constraints are shown in pink, and the CMB results from *Planck* are shown in orange. Figure from: Joudaki et al. (2019).

fits a pattern of weak lensing observations finding a lower value of S_8 than *Planck* (Heymans et al., 2013).

To confirm or disprove the above tension the precision of the weak lensing results needs to be increased. A key limiting factor in current and upcoming weak lensing surveys is the accuracy of their photometric redshifts. Ideally, the redshift of a galaxy would be found by measuring the full spectrum of light from a galaxy, and looking for shifts in characteristic spectral lines – spectroscopic redshift. Unfortunately, due to the large numbers of galaxies involved in a weak lensing analysis, this technique is prohibitively slow. Instead low-resolution spectra are obtained by measuring the spectrum in a few broad filters ($\sim$5) – photometric redshift. The uncertainties on photometric redshifts can be very large, and inaccurate estimation biases the final results (Joudaki et al., 2019).

Figure 1.6: The Vera Rubin Observatory in June 2020. Figure from: Rubin Observatory image gallery.

1.3.3 Vera Rubin Observatory

The Vera Rubin Observatory Legacy Survey of Space and Time (LSST) is an upcoming 10 year survey planned to begin taking data in 2021. It will utilise the 8.4m Simonyi Survey Telescope, which is located on top of the Cerro Pachón ridge in Chile, see Fig. 1.6. The telescope has an exceptionally large field of view of 9.62 square degrees (40 times the area of the full moon), which enables it to survey the entire sky every three nights.

The LSST camera is the largest digital camera ever constructed in astronomy and contains over three billion pixels. Over the course of 10 years LSST will image billions of objects in six color bands u, g, r, i, z and y, see Fig. 1.7. LSST will also be able to record the time evolution of these objects due to its repeated imaging every three nights. While unimportant for weak lensing this is of great interest to cosmologists studying supernovae. The aspects of LSST that make it suited to weak lensing analyses are the large area and great depth, which result in a large number of objects. One of the greatest challenges for LSST is processing the huge amount of data it will produce every night due to its speed and depth, approximately 20 Terabytes. (LSST Science Collaboration, 2009)

We provide details for LSST since it is the focus of our forecast in chapter 3, however there are also upcoming satellite missions for weak lensing such as *Euclid* and the Nancy Grace Roman Space Telescope (previously known as WFIRST) (Spergel et al., 2015). These missions will be highly complementary to LSST. They will have much better resolution imaging, since they do not have to contend with the atmosphere, but are not as deep so will detect fewer objects (Rhodes et al., 2017; Schuhmann et al., 2019).

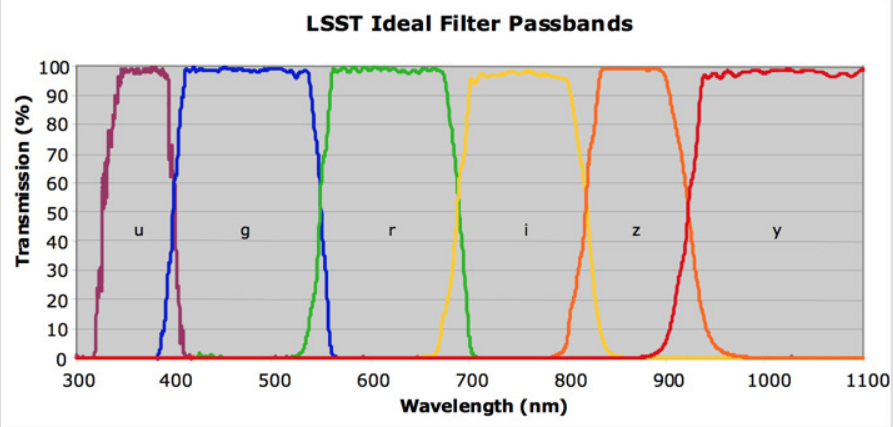

Figure 1.7: Transmission functions for the 6 LSST filters u, g, r, i, z and y. Figure from: Olivier et al. (2008).

1.4 Neutrinos

Neutrino physics is a truly interdisciplinary area of research, where discovering the properties of neutrinos will likely require combining observations from particle physics, cosmology and astrophysics. In this section we present a brief theoretical overview of neutrinos in particle physics and in cosmology. Then in chapter 2 we discuss how to combine the current best measurements of neutrino properties, from particle physics and from cosmology, in order to learn about the ordering of the neutrino masses.

1.4.1 Neutrinos in Particle Physics

Discovery of the neutrino

The neutrino was first postulated by Pauli in 1930 to explain the continuous beta decay spectrum (Pauli, 1978). Beta decay is a type of radioactive decay where a beta particle (electron or positron) is emitted from a nucleus. At the time it was thought that this process was a two body decay, so the energy spectrum of the electron was expected to be sharply peaked. However, the observed spectrum resembled that of a three body decay and led to Pauli postulating the existence of a light, weakly interacting, neutral particle.

This prediction was confirmed by Cowan and Reines in 1956 when they observed beta decay antineutrinos ($\bar{\nu}_e$) from a nearby nuclear reactor using inverse beta decay, $\bar{\nu}_e + p^+ \rightarrow n + e^+$ (Cowan et al., 1956). The existence of three flavours of neutrino – electron, muon and tau – was established by the discovery of the muon neutrino in 1962 (Danby et al., 1962) and the tau neutrino in 2001

(Kodama et al., 2001).

Neutrino Oscillations

The importance of the discovery of neutrino oscillations – that neutrinos change flavour as they propagate – cannot be understated. It can only be explained by neutrinos having mass, which is contrary to the Standard Model.

Conclusive evidence for neutrino oscillations came from two different sources, solar and atmospheric neutrinos. In the 1960s the Homestake experiment measured the flux of neutrinos from the Sun and found that it was much smaller than predicted by solar models (Davis et al., 1968). Since this experiment was only sensitive to electron neutrinos it was possible that the neutrinos were changing flavour between the Sun and the Earth. More powerful evidence came from the Sudbury Neutrino Observatory (SNO) in 2001 (Ahmad et al., 2001). This experiment measured both the flux of electron neutrinos and the total flux of neutrinos from the sun, above a certain energy. The total flux was found to match solar models and provided strong evidence for neutrino oscillations. Neutrinos are also produced in the atmosphere by cosmic rays. In 1988 the Kamiokande experiment measured the flux of atmospheric electron and muon neutrinos and found that while the electron neutrino flux matched predictions, not including oscillations, there was a significant deficit in the muon neutrino flux (Hirata et al., 1988). In 1998 the Super-Kamiokande experiment found that this flux deficit matched the predictions from oscillation models (Fukuda et al., 1998). These discoveries led to the Nobel Prize for Physics being awarded to the SNO and Super-Kamiokande collaborations in 2015.

In the three-neutrino oscillation model the neutrino flavour eigenstates $|\nu_\alpha\rangle$ are a superposition of the neutrino mass eigenstates $|\nu_i\rangle$,

$$|\nu_\alpha\rangle = \sum_{i=1}^{3} U_{\alpha i}|\nu_i\rangle \ , \tag{1.62}$$

where U is the mixing matrix which relates the mass and flavour eigenstates. This unitary matrix is called the PMNS (Pontecorvo-Maki-Nakagawa-Sakata) matrix and takes the form,

$$U = \begin{pmatrix} U_{e1} & U_{e2} & U_{e2} \\ U_{\mu 1} & U_{\mu 2} & U_{\mu 3} \\ U_{\tau 1} & U_{\tau 2} & U_{\tau 3} \end{pmatrix} \ . \tag{1.63}$$

This matrix is often parametrised as,

$$\begin{pmatrix} 1 & 0 & 0 \\ 0 & c_{23} & s_{23} \\ 0 & -s_{23} & c_{23} \end{pmatrix} \begin{pmatrix} c_{13} & 0 & s_{13}e^{-i\delta_{CP}} \\ 0 & 1 & 0 \\ -s_{13}e^{-i\delta_{CP}} & 0 & c_{13} \end{pmatrix} \begin{pmatrix} c_{12} & s_{12} & 0 \\ -s_{12} & c_{12} & 0 \\ 0 & 0 & 1 \end{pmatrix} , \tag{1.64}$$

where $c_{ij} = \cos\theta_{ij}$ and $s_{ij} = \sin\theta_{ij}$. θ_{12}, θ_{13} and θ_{23} are mixing angles and δ_{CP} is a CP violating phase. The matrix U is parametrised in this way because different experiments are sensitive to different mixing angles. The first matrix only includes θ_{23}, which is probed by atmospheric neutrino experiments. The third matrix only includes θ_{12}, which is probed solar neutrino experiments. The second matrix depends on the mixing angle θ_{13} and the CP violating phase δ_{CP}. δ_{CP} is non-zero only if neutrino oscillations violate CP (charge-parity) symmetry (different oscillation probabilities for neutrinos and antineutrinos). A discovery of non-zero δ_{CP} would be a significant finding that could help explain the dominance of matter over antimatter in the Universe.

Note that δ_{CP} is always multiplied by θ_{13} in the second matrix, so a measurement of δ_{CP} requires θ_{13} to be non zero. The first evidence of θ_{13} being non zero came from the Daya Bay reactor neutrino experiment in 2012 (An et al., 2012). In reactor neutrino experiments the source of neutrinos is a nuclear reactor, as opposed to the sun or the atmosphere. This finding was then confirmed in 2014 by the Tokai-to-Kamioka (T2K) experiment (Abe et al., 2014). T2K is a long baseline neutrino experiment, which studies the oscillations of accelerator neutrinos. Following these results, there have been recent exciting indications of a non-zero δ_{CP} from the T2K experiment (Abe et al., 2020).

Neutrinos are detected as flavour eigenstates but propagate as mass eigenstates. In the relativistic case, where the rest mass is much less than the energy of the neutrino, the probability $P(\nu_\alpha \to \nu_\beta)$ for $\nu_\alpha \to \nu_\beta$ is,

$$\begin{aligned} P(\nu_\alpha \to \nu_\beta) &= \left| \sum_i U^*_{\alpha i} U_{\beta i} e^{-i m_i^2 L/2E} \right|^2 \\ &= \delta_{\alpha\beta} - 4 \sum_{i>j} \mathrm{Re}(U^*_{\alpha i} U_{\beta i} U_{\alpha j} U^*_{\beta j}) \sin^2\left(\frac{\Delta m^2_{ij} L}{4E}\right) \\ &\quad + 2 \sum_{i>j} \mathrm{Im}(U^*_{\alpha i} U_{\beta i} U_{\alpha j} U^*_{\beta j}) \sin^2\left(\frac{\Delta m^2_{ij} L}{4E}\right) , \end{aligned} \tag{1.65}$$

where $\delta_{\alpha\beta}$ is the Kronecker delta,

$$\Delta m^2_{ij} \equiv m^2_i - m^2_j , \tag{1.66}$$

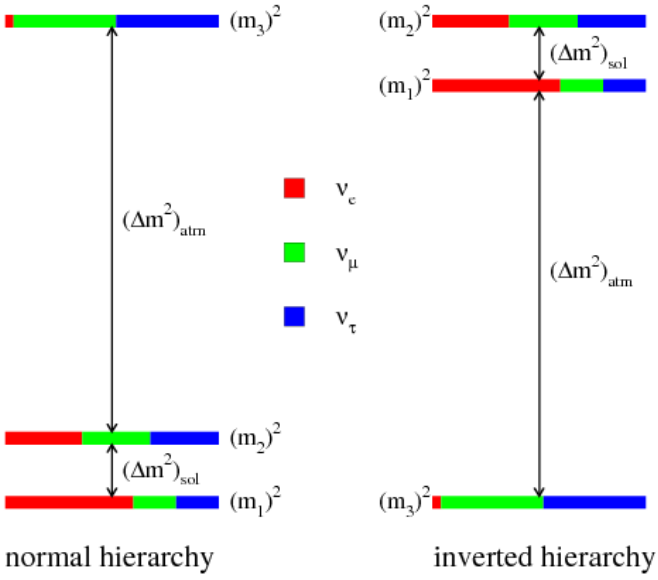

Figure 1.8: Diagram illustrating the two possible orderings of the neutrino mass eigenstates alowed by the current best measurements of the mass squared splittings Δm^2_{12} and Δm^2_{32}. Figure from: Hewett et al. (2012).

E is the energy of the neutrino and L is the distance over which it has propagated. We include this equation to show that a change in neutrino flavour can only occur if at least one neutrino has mass. If $\Delta m^2_{ij} = 0$ for all i and j the probability reduces to $\delta_{\alpha\beta}$ – there is no oscillation. This equation also shows that neutrinos change flavour with a probability which oscillates as a function of L/E, hence the name neutrino oscillation. This dependence is key in designing neutrino experiments. Finally, this equation shows that neutrino oscillation measurements are sensitive to Δm^2_{ij} not the neutrino masses m_i directly.

Neutrino Mass

Δm^2_{12} and Δm^2_{32} have been measured by neutrino oscillations experiments, see chapter 2 for the current best constraints. The sign of Δm_{12} has also been determined using the Mikheyev-Smirnov-Wolfenstein (MSW) effect, which modifies neutrino oscillations in matter (Tanabashi et al., 2018), but not the sign of Δm_{32}. This leaves two possible orderings of the neutrino mass eigenstates; Normal where $m_1 < m_2 < m_3$ or Inverted where $m_3 < m_1 < m_2$. See Fig. 1.8 for a diagram. Additionally, the overall scale of the neutrino masses is unknown.

The current best constraint on the scale of the neutrino masses comes from cosmology, see chapter 2. However, there are also particle physics experiments which focus on measuring the

neutrino mass scale. One avenue is through making precise measurements of the beta decay spectrum. If ν_e is massive then the maximum energy of the beta electron is reduced. Therefore, by studying the endpoint of the spectrum it should be possible to determine the ν_e mass, $m(\nu_e)$. The current best constraint comes from the KATRIN experiment where $m(\nu_e) < 1.1$ eV (Aker et al., 2019). The benefit of this approach is that it is not model dependent (the cosmology results assume ΛCDM). Another avenue for measuring the neutrino mass is through neutrinoless double-beta decay. Double beta decay refers to when two beta decays occur simultaneously inside a nucleus, releasing two electrons and two electron anti-neutrinos. If neutrinos are Majorana particles (identical to their antiparticles) they can effectively annihilate resulting in two electons, which carry the whole energy of the decay. Neutrinoless double beta decay has never been observed, but experiments such as SuperNEMO and KamLAND-Zen are currently searching. A measurement of neutrinoless double-beta decay would determine the nature of neutrinos, and set a scale for the neutrino masses (Avignone et al., 2008).

1.4.2 Neutrinos in Cosmology

This section is largely based on the summaries of neutrino cosmology given in Tanabashi et al. (2018), Gerbino (2018), Dodelson (2003) and Mo et al. (2010). For more detailed reviews see Lesgourgues and Pastor (2006), Hannestad and Schwetz (2016) and Lattanzi and Gerbino (2018).

Cosmic Neutrino Background

In the early Universe neutrinos were in thermal equilibrium with the cosmic plasma. Later, when the weak interaction rate fell below the expansion rate of the Universe the neutrinos decoupled from the plasma. After decoupling their temperature fell as a^{-1}. To relate the neutrino temperature to the photon temperature today (CMB temperature) we need to consider the effects of electron-positron annihilation. Neutrinos decoupled just before electron-positron annihilation, so while energy was transferred to the rest of the plasma it was not transferred to the neutrinos. The CMB temperature today is therefore higher than the relic neutrino temperature. The ratio of the temperatures today can be computed using entropy conservation to give,

$$\frac{T_\nu}{T_\gamma} = \left(\frac{4}{11}\right)^{1/3}. \tag{1.67}$$

Neutrinos are relativistic in the early Universe so contribute to the radiation density. The

radiation density ρ_r, including neutrinos, is often parametrised as,

$$\rho_r = \rho_\gamma \left[1 + \frac{7}{8} \left(\frac{4}{11} \right)^{4/3} N_{\rm eff} \right] , \tag{1.68}$$

where ρ_γ is the photon density, the factor $7/8$ accounts for the neutrinos following a Fermi-Dirac instead of a Bose-Einstein distribution, the power $4/3$ comes from the temperature ratio in eq. 1.67 and that the energy density of massless particles scales as T^4, and $N_{\rm eff}$ is the effective number of neutrino species. $N_{\rm eff}$ is labelled *effective* because it can be used to account for any relativistic species present at early times. In the standard three-neutrino cosmological model $N_{\rm eff} = 3.045$, where the extra 0.045 contribution comes from including neutrino oscillations, non-instantaneous decoupling and improved calculation of the collision terms (de Salas and Pastor, 2016).

At late times we know that at least two neutrinos are non relativistic, as the neutrino temperature today is less than both mass squared differences measured by neutrino oscillation experiments. This means that at late times neutrinos contribute to the matter density of the Universe. The energy density of non-relativistic neutrinos is given by $\rho_\nu \approx \Sigma m_i n_i$, since their velocities are small compared to their rest mass. Since the number densities n_i are equal for each neutrino species the energy density can be parametrised in terms of the sum of the neutrino masses Σm_ν. The neutrino density parameter today Ω_ν is given by,

$$\Omega_\nu = \frac{\rho_\nu}{\rho_{\rm crit}} = \frac{\Sigma m_\nu}{93.14 h^2 {\rm eV}} , \tag{1.69}$$

where the factor of 93.14 includes n_i/n_γ from theoretical studies of neutrino decoupling and n_γ from the CMB (Tanabashi et al., 2018).

These equations show that the quantities of interest when studying neutrinos in cosmology are $N_{\rm eff}$ and Σm_ν. Cosmology is not sensitive to the mixing angles or the CP violating phase measured in oscillation experiments but is highly complementary.

Observing Neutrinos

Directly measuring the cosmic neutrino background is extremely challenging, but there are experiments in development (Betti et al., 2019). However, neutrinos have a number of effects on cosmology, which can be used to probe their properties indirectly. Neutrinos contribute to the energy density of the universe and hence affect the expansion history. Since they affect the proportion of radiation at early times and the proportion of matter at late times they can alter the redshift of

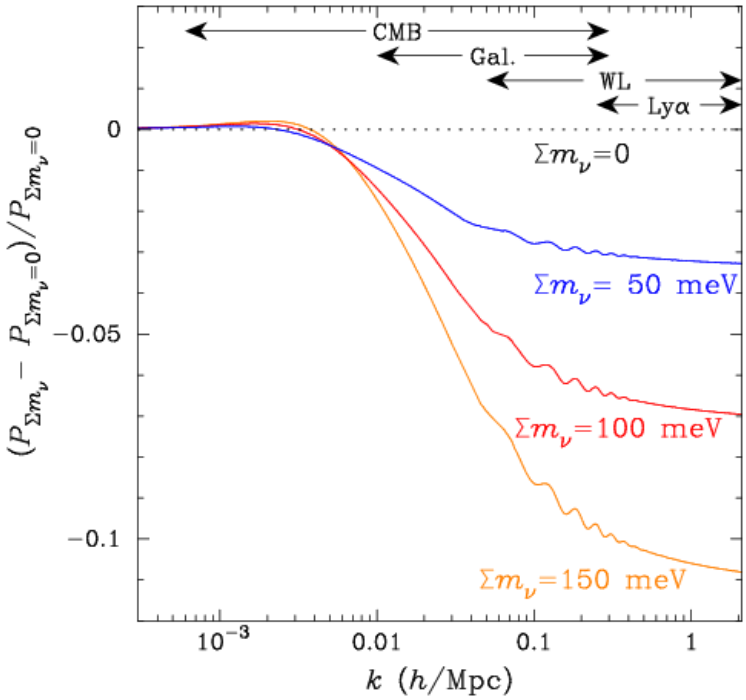

Figure 1.9: Fractional change in the matter power spectrum as a function of wavenumber k for different values of the neutrino mass sum Σm_ν. Massive neutrinos suppress structure on small scales. The arrows indicate the approximate scales probed by different cosmological observations. Figure from: Abazajian et al. (2015).

the matter-radiation equality (see section 1.1.3). They can also affect the development of matter perturbations, and one of the most sensitive methods for determining neutrino properties from cosmology is through their effect on the matter power spectrum.

While neutrinos are relativistic they can free stream out of high-density regions, suppressing perturbations smaller than the free-streaming scale. The free-streaming scale is the distance a neutrino can travel in H^{-1} (a proxy for the age of the universe) at its current speed. Above the free-streaming scale neutrinos cluster as matter. This leads to an overall suppression in the matter power spectrum at small scales, as shown in Fig. 1.9. Neutrinos with greater mass become non-relativistic at earlier times, so the free streaming length is smaller and the suppression starts on smaller scales (higher k). Additionally, neutrinos with greater mass contribute more to the energy density of the universe and hence, by free-streaming, suppress perturbations to a greater extent.

Measuring this suppression in the matter power spectrum requires combining a number of probes over different scales, finding the large-scale amplitude with the CMB and then determining the small-scale amplitude with ground-based large scale structure experiments. Since the effect of

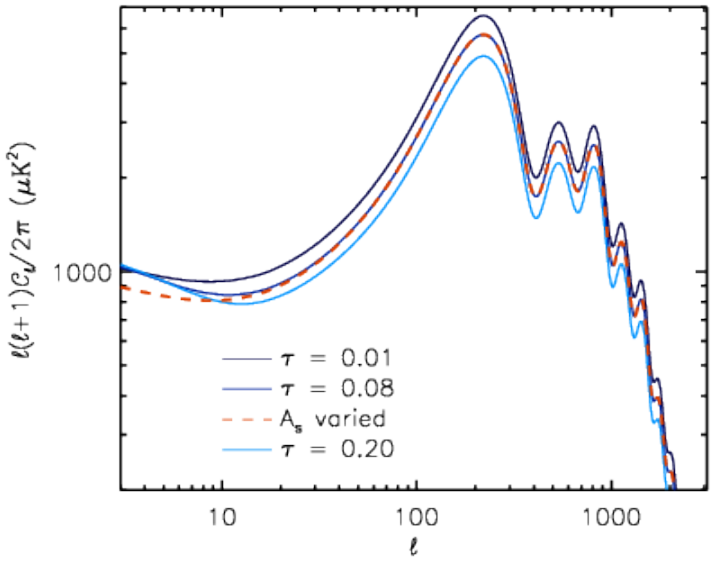

Figure 1.10: The CMB temperature power spectrum for different values of the optical depth to reionisation τ. Changing τ changes the amplitude of the power spectrum. Figure from: Reichardt (2015).

neutrinos can be compensated for by adjusting other cosmological parameters, combining multiple probes which are sensitive to different combinations of parameters helps to limit the number of degeneracies and hence improve the precision of the neutrino mass measurement. See chapter 2 for a discussion of the precision of current and future neutrino mass sum measurements from cosmology.

One particularly important degeneracy for upcoming measurements of neutrino mass involves the optical depth to reionisation τ. This is because the amplitude of the CMB temperature power spectrum is given by $A_s e^{-2\tau}$ (if all other cosmological parameters are fixed) so if τ changes so does the amplitude. This means that in order to obtain a highly precise constraint on neutrino mass τ must be determined to a very high level of precision. CMB polarization measurements on large scales (from space) are expected to significantly improve the τ measurement. Figure 1.10 illustrates how a change in τ impacts the amplitude of the CMB temperature power spectrum. Figure 1.11 shows that τ can be disentangled from an overall amplitude change with measurements of the CMB polarization power spectrum on large scales. The only approved upcoming experiment, which is potentially capable of performing this measurement is the LiteBIRD satellite (Hazumi et al., 2019).

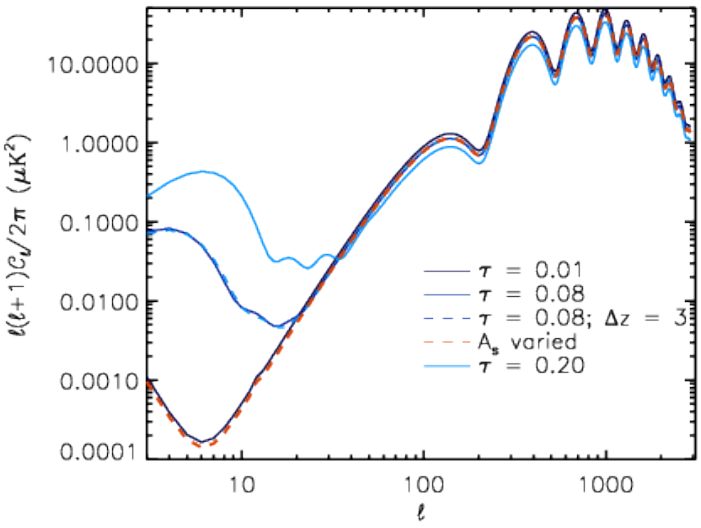

Figure 1.11: The CMB polarization power spectrum for different values of the optical depth to reionisation τ. At large scales (small ℓ) changes to the optical depth can be distinguished from an overall amplitude change. Figure from: Reichardt (2015).

2

Target Neutrino Mass Precision for Determining the Neutrino Hierarchy

Recent works combining neutrino oscillation and cosmological data to determine the neutrino hierarchy found a range of odds in favour of the normal hierarchy. These results arise from differing approaches to incorporating prior knowledge about neutrinos. We develop a hierarchy-agnostic prior and show that the hierarchy cannot be conclusively determined with current data. The determination of the hierarchy is limited by the neutrino mass scale Σ_ν measurement. We obtain a target precision of $\sigma(\Sigma_\nu) = 0.014$ eV, necessary for conclusively establishing the normal hierarchy with future data.

2.1 Introduction

Particle physics and cosmology provide complementary information about neutrinos. Neutrino oscillation experiments have determined that neutrinos have mass, contrary to the Standard Model, and that there are three mass eigenstates (De Salas et al., 2018). They have also measured two mass-squared splittings between these mass states. However, the overall scale of the neutrino masses is unknown, as is the ordering of the two squared splittings — the neutrino hierarchy. Cosmological data place a constraint on the sum of neutrino masses, which provides an overall scale and will help to distinguish the hierarchy (Tanabashi et al., 2018). Determining the neutrino hierarchy is key to further understanding the properties of the neutrino sector and theories of neutrino mass generation (Patterson, 2015).

The two possible orderings of the neutrino mass states are the Normal Hierarchy (NH) and the Inverted Hierarchy (IH). The IH has a greater total mass. The minimum total mass for the NH and IH can be calculated by fixing the mass of the lightest state at zero and using current squared

splitting measurements to calculate the mass of the other two states. In the NH configuration the minimum total mass is 0.06 eV, and in the IH configuration the minimum total mass is 0.1 eV. Recent cosmological measurements have placed a 95% CL upper bound on the sum of the neutrino masses of 0.12 eV (Aghanim et al., 2018), which is tantalizingly close to the IH minimum mass.

Motivated by these results, many works have performed joint analyses of neutrino oscillation and cosmology data to see if there is already sufficient evidence for the NH (Gariazzo et al., 2018; Gerbino et al., 2017; Hannestad and Schwetz, 2016; Heavens and Sellentin, 2018; Long et al., 2018; Simpson et al., 2017; Vagnozzi et al., 2017). The results of these analyses vary dramatically, producing relative odds favoring the NH over the IH ranging from 3:2 to 470:1. The main difference between these analyses is how they incorporate the state of knowledge about the neutrino hierarchy before taking any data into account: their choice of prior (Gariazzo et al., 2018; Heavens and Sellentin, 2018). Choosing an appropriate prior is difficult because a physically-motivated prior on the neutrino properties (whether they are the individual masses, squared splittings, mixing angles, etc) does not exist (Long et al., 2018). Further, there is a complex mapping between priors on the neutrino masses to odds on the hierarchy, so a seemingly innocuous prior choice can strongly favor a particular hierarchy.

In this work we develop a methodology for a joint analysis of neutrino oscillation and cosmology data, which is agnostic to the hierarchy — a hierarchy-agnostic prior. This guarantees that the relative odds of the NH:IH are driven by the data, and not by the choice of prior. We demonstrate using this prior that current data are not sufficiently constraining to determine the hierarchy. The limiting factor in determining the hierarchy is the neutrino mass sum measurement. We therefore set a target precision for future measurements of the neutrino mass sum, necessary in order to make a conclusive determination of the hierarchy. Assuming the NH minimum mass, this is sufficient for a conclusive determination, but other configurations will require an increased precision.

Current neutrino data is presented in section 2.2. The method for constructing a hierarchy-agnostic prior and calculating the relative odds NH:IH is described in section 2.3. The odds NH:IH for current data and a target precision for future experiments are presented in section 2.4, with conclusions summarized in section 2.5.

2.2 Current Data

Neutrino oscillation experiments have measured two mass-squared splittings: the mass-squared splitting between the closest two neutrinos Δm^2_S (the small splitting) and the mass-squared splitting

between the furthest and the midpoint of the closest two Δm^2_L (the large splitting). If we label and order the masses as $m_a < m_b < m_c$, in the NH case we have

$$\begin{aligned} \Delta m^2_S &= m^2_b - m^2_a \ , \\ \Delta m^2_L &= m^2_c - \frac{1}{2}(m^2_b + m^2_a) \ , \end{aligned} \tag{2.1}$$

and in the IH case,

$$\begin{aligned} \Delta m^2_S &= m^2_c - m^2_b \ , \\ \Delta m^2_L &= \frac{1}{2}(m^2_c + m^2_b) - m^2_a \ . \end{aligned} \tag{2.2}$$

The current best constraints on these parameters are shown in Table 2.1. The constraint on the small splitting Δm^2_S comes from combining data from the KamLAND experiment with a global analysis of solar, accelerator and short-baseline reactor neutrino experiments (Gando et al., 2013). The constraint on the large splitting Δm^2_L comes from a global analysis of data from atmospheric (Aartsen et al., 2018; Abe et al., 2018a), short-baseline reactor (Adey et al., 2018; Bak et al., 2018) and long-baseline accelerator neutrino experiments (Abe et al., 2018b; Acero et al., 2018; Adamson et al., 2014). Individual neutrinos are produced in interaction (i.e., flavor) eigenstates. Since the flavor eigenstates (ν_e, ν_μ and ν_τ) are mixtures of the mass eigenstates (m_a, m_b and m_c), the neutrino flavor subsequently oscillates as it propagates. This means if a certain number of electron neutrinos (ν_e) are produced by a source, as they propagate the number will change and manifest as a deficit of electron neutrinos and an excess of muon (ν_μ) and tau neutrinos (ν_τ). All of the experiments mentioned above search for a mismatch between the number of a particular neutrino flavor produced by a source and the number measured by the detector a certain distance away, using different sources and different distances. For example, KamLAND measures a deficit of electron anti-neutrinos using Japanese nuclear reactors as a source.

Cosmological data constrain the sum of neutrino masses:

$$\Sigma_\nu = m_a + m_b + m_c \ , \tag{2.3}$$

and the current best constraint is shown in Table 2.1 (Aghanim et al., 2018). This constraint comes from a combination of cosmological probes: the temperature and polarization fluctuations in the cosmic microwave background (CMB), which is the relic radiation from the surface of last scattering 380,000 years after the Big Bang (Hu and Dodelson, 2002); weak gravitational lensing, which

Table 2.1: Current best constraints for the mass-squared splittings with their associated 1σ uncertainty from oscillation experiments (Tanabashi et al., 2018), and 95% CL upper bound on the sum of neutrino masses from cosmological data (Aghanim et al., 2018). The results are quoted in terms of the parameters used this in work.

Measurable Parameter	**Current Constraint**
Δm^2_S	$(7.53 \pm 0.18) \times 10^{-5}$ eV^2 (Tanabashi et al., 2018)
Δm^2_L (NH)	$(2.444 \pm 0.034) \times 10^{-3}$ eV^2 (Tanabashi et al., 2018)
Δm^2_L (IH)	$(2.53 \pm 0.05) \times 10^{-3}$ eV^2 (Tanabashi et al., 2018)
Σ_ν	< 0.12 eV (Aghanim et al., 2018)

uses coherent distortions in observations of the CMB or galaxies to probe the matter distribution along the line of sight (Bartelmann and Schneider, 2001; Lewis and Challinor, 2006); and baryon acoustic oscillations (BAO), which measure a standard distance scale set by sound waves in the early universe (Anderson et al., 2014). The CMB and lensing part of this constraint comes from the *Planck* satellite (Aghanim et al., 2018), and the BAO part comes from low redshift galaxy surveys (Ade et al., 2014). A larger neutrino mass sum suppresses the growth of structure in the universe; it is only by combining measurements of cosmic structure at early times, late times, small scales and large scales, that the effect of massive neutrinos can be determined.

2.3 Method

To quantify whether one hierarchy is favored over the other, we compute the posterior odds, given by

$$\frac{p(\mathrm{NH}|D)}{p(\mathrm{IH}|D)} = \frac{p(\mathrm{NH})}{p(\mathrm{IH})} \frac{p(D|\mathrm{NH})}{p(D|\mathrm{IH})} \,, \tag{2.4}$$

where D represents current data. We wish to impose equal prior odds on the hierarchies, *i.e.* $p(\mathrm{NH}) = p(\mathrm{IH})$. Therefore, the first term on the right-hand side is equal to one, and calculating the posterior odds equates to calculating the ratio of the marginal likelihoods, $p(D|\mathrm{NH})$ and $p(D|\mathrm{IH})$. Calculating the marginal likelihoods requires marginalizing over the individual neutrino properties, and we compute them via Monte Carlo integration:

$$\begin{aligned} p(D|\mathrm{H}) &= \int p(D|\boldsymbol{\theta}, \mathrm{H}) p(\boldsymbol{\theta}|\mathrm{H}) \, \mathrm{d}\boldsymbol{\theta} \\ &\approx \frac{1}{N} \sum_{i=1}^{N} p(\Delta m^2_S|\boldsymbol{\theta}_i, \mathrm{H}) p(\Delta m^2_L|\boldsymbol{\theta}_i, \mathrm{H}) p(\Sigma_\nu|\boldsymbol{\theta}_i, \mathrm{H}) \,. \end{aligned} \tag{2.5}$$

Here $\boldsymbol{\theta}$ represents a parametrization which describes the properties of three neutrinos, N is the number of sets of neutrino properties drawn from our prior $p(\boldsymbol{\theta}|\mathrm{H})$, and H is the hierarchy under consideration. The likelihood of the data given the parameter set and hierarchy, $p(D|\boldsymbol{\theta}, \mathrm{H})$, can be split into the likelihoods $p(\Delta m_S^2|\boldsymbol{\theta}, \mathrm{H})$, $p(\Delta m_L^2|\boldsymbol{\theta}, \mathrm{H})$ and $p(\Sigma_\nu|\boldsymbol{\theta}, \mathrm{H})$ because the measurements of Δm_S^2, Δm_L^2 and Σ_ν are independent. In principle these individual likelihoods should be the data likelihoods from the experiments reported in Table 2.1. However, these results are independent and can be accurately approximated with surrogate likelihoods [1] for the purposes of this work. As such, the likelihoods for Δm_S^2 and Δm_L^2 are taken to be normal distributions with mean the measured value and standard deviation the associated uncertainty, given in Table 2.1. Note that Δm_L^2 differs between the hierarchies. Since cosmological data currently only places an upper bound on the sum of neutrino masses Σ_ν, the likelihood is taken to be a normal distribution centered on zero with standard deviation half the 95% upper bound. A normal distribution provides a flexible interpretation of the upper bound, which also allows negative values not currently excluded by cosmological data alone.

If we draw $\boldsymbol{\theta}$ from a prior which favors the NH, the corresponding posterior odds will also be weighted in favor of the NH. For example, previous works have shown that defining $\boldsymbol{\theta} = \{m_a, m_b, m_c\}$ and drawing the three masses from the same log-normal distribution[2] (then ordering them $m_a < m_b < m_c$) is a seemingly reasonable choice which, however, strongly favors the NH (Gariazzo et al., 2018; Simpson et al., 2017). We therefore require a prior which does not favor a hierarchy; where it is equally likely that a randomly drawn $\boldsymbol{\theta}$ corresponds to the NH as to the IH.

Previous works have achieved this by adopting a continuous or discrete hierarchy parameter, which is positive for the NH and negative for the IH (Gerbino et al., 2017; Jimenez et al., 2010; Loureiro et al., 2019; Xu and Huang, 2018). However, we achieve this through our choice of parametrization for $\boldsymbol{\theta}$. The only requirement is that the parameter set $\boldsymbol{\theta}$ can be translated to the measured quantities Δm_S^2, Δm_L^2 and Σ_ν. We choose $\boldsymbol{\theta} = \{\Delta m_a^2, \Delta m_b^2, m_a\}$ where Δm_a^2 is the mass-squared splitting between the lightest two neutrinos, Δm_b^2 the mass-squared splitting between the heaviest two, and m_a the mass of the lightest neutrino. Explicitly

$$\begin{aligned} \Delta m_a^2 &= m_b^2 - m_a^2 \,, \\ \Delta m_b^2 &= m_c^2 - m_b^2 \,, \end{aligned} \tag{2.6}$$

where $m_a < m_b < m_c$. Our approach means that the prior assumptions about neutrinos going into

[1] Likelihoods which use the experimental measurements to approximate the data likelihoods.
[2] The log-normal distribution is a continuous distribution where the logarithm of the variable is normally distributed.

the analysis are explicit, which is not the case for Jimenez et al. (2010); Xu and Huang (2018), and does not require introducing a separate discrete hierarchy parameter as in Gerbino et al. (2017); Loureiro et al. (2019). Parametrizing neutrino properties in terms of a minimum mass and two splittings is quite common (e.g., Beacom and Bell 2002; De Salas et al. 2018; Gerbino et al. 2017); however, the potential of this parametrization for constructing an explicitly equal-odds prior has not been previously investigated.

In the case of the NH $\Delta m_a^2 < \Delta m_b^2$ and the IH $\Delta m_b^2 < \Delta m_a^2$. Therefore, to construct a hierarchy-agnostic prior, we require $\Delta m_a^2 < \Delta m_b^2$ to be equally likely to $\Delta m_b^2 < \Delta m_a^2$. Hence we draw Δm_a^2 and Δm_b^2 from the same distribution. In our parametrization we wish the splittings to be positive and vary over a large range. There are a number of distributions which satisfy these requirements, for example uniform in log space (log-uniform) or log-normal. However, given the high accuracy of current splitting measurements, we have verified that the particular form of this distribution is unimportant. We therefore choose a log-normal distribution because it provides a proper prior [3].

The parameter m_a is required to translate Δm_a^2 and Δm_b^2 to the measurable quantities Δm_S^2, Δm_L^2 and Σ_ν, as it provides an overall mass scale. Other possible options are m_a^2 or Σ_ν. We require m_a to be non-negative and little is known about its magnitude. In the case where a parameter can vary over many orders of magnitude a log-uniform prior is a reasonable choice. We found that our results were unchanged whether we used a log-uniform or a log-normal prior, so we once again choose a log-normal prior (see Table 2.2 in the results section).

The log-normal distributions used in this analysis are defined by the mean, μ, and standard deviation, σ, of the root normal distribution. As such our prior space is defined by four parameters μ_s, σ_s, μ_{m_a} and σ_{m_a} for the priors on the splittings, Δm_a^2 and Δm_b^2, and m_a respectively. Our final posterior odds result was found to be invariant over a large range of different choices for these prior parameters; in this work we specifically used $\mu_s = -9.25$, $\sigma_s = 5.0$, $\mu_{m_a} = 0.0$ and $\sigma_{m_a} = 7.0$, where Δm_a^2 and Δm_b^2 have units of eV^2 and m_a has units of eV. This choice gives a broad prior on the splittings because little is known about the magnitude of the mass-squared splittings before including oscillation data (Tanabashi et al., 2018). This choice is also motivated by the recent KATRIN result that the highest allowed value of the effective electron neutrino mass is less than 1.1 eV (Aker et al., 2019). Additionally, this specific prior choice translates into three approximately log-normal distributions on the individual neutrino masses, which are defined by distinct parameters (see Fig. 2.1). These distributions are strongly correlated because m_b and m_c are computed by adding the splittings to m_a, so a larger m_a results in a larger m_b and m_c.

[3] a prior distribution that integrates to 1

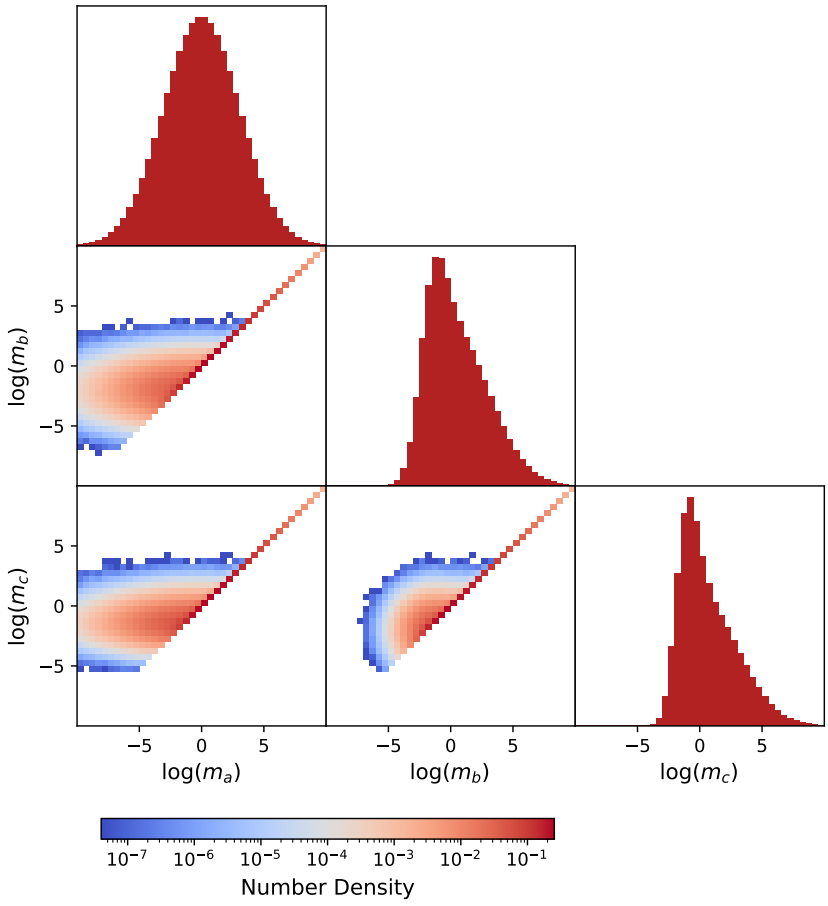

Figure 2.1: Our prior on the splittings, Δm_a^2 and Δm_b^2, and lightest neutrino mass, m_a, translated to the log neutrino masses, where $m_a < m_b < m_c$.

As expected, they are particularly strongly correlated when m_a is much larger than the splittings because the masses become quasi-degenerate [4]. The form of this prior is in contrast to log-normal priors on the individual masses where the masses are drawn from the same distribution, which have previously been found to favor the NH (Gariazzo et al., 2018; Simpson et al., 2017).

Once we have defined a hierarchy-agnostic prior, we randomly draw N sets of neutrino properties, $\boldsymbol{\theta} = \{\Delta m_a^2, \Delta m_b^2, m_a\}$. Next, we use all our samples of $\boldsymbol{\theta}$ to calculate $p(D|\mathrm{NH})$. The first step in computing $p(D|\mathrm{NH})$ is to translate the parameters Δm_a^2, Δm_b^2 and m_a to the measurable

[4]This pattern is also seen in neutrinoless double-β decay discovery plots (Agostini et al., 2017; Tanabashi et al., 2018)

quantities Δm^2_S, Δm^2_L and Σ_ν. Assuming the NH,

$$\begin{aligned} \Delta m^2_S &= \Delta m^2_a \,, \\ \Delta m^2_L &= \Delta m^2_b + \Delta m^2_a/2 \,, \end{aligned} \tag{2.7}$$

and

$$\Sigma_\nu = m_a + \sqrt{m_a^2 + \Delta m_a^2} + \sqrt{m_a^2 + \Delta m_a^2 + \Delta m_b^2} \,. \tag{2.8}$$

Once these values are found for every $\boldsymbol{\theta}$ they are used to compute the individual likelihoods $p(\Delta m^2_S|\boldsymbol{\theta}, \mathrm{NH})$, $p(\Delta m^2_L|\boldsymbol{\theta}, \mathrm{NH})$ and $p(\Sigma_\nu|\boldsymbol{\theta}, \mathrm{NH})$. Equation (2.5) is then employed to compute $p(D|\mathrm{NH})$.

Next we use the same set of $\boldsymbol{\theta}$ to compute $p(D|\mathrm{IH})$. This is allowable because our hierarchy-agnostic prior means that $p(\boldsymbol{\theta}|\mathrm{NH}) = p(\boldsymbol{\theta}|\mathrm{IH})$. The procedure for computing $p(D|\mathrm{IH})$ is analogous to $p(D|\mathrm{NH})$. However, there are two differences: the translation of Δm^2_a and Δm^2_b to the measured splittings,

$$\begin{aligned} \Delta m^2_S &= \Delta m^2_b \,, \\ \Delta m^2_L &= \Delta m^2_a + \Delta m^2_b/2 \,; \end{aligned} \tag{2.9}$$

and the form of $p(\Delta m^2_L|\boldsymbol{\theta}, \mathrm{IH})$, as the measured value of Δm^2_L differs between the hierarchies (see Table 2.1).

Once $p(D|\mathrm{NH})$ and $p(D|\mathrm{IH})$ are calculated, the ratio can be computed to find the posterior odds, as in Eq. (2.4). Since our calculation of the posterior odds is based on simulations, it is approximate. However, we find the posterior odds calculated with this method are approximately normal distributed if the number of sets of neutrino properties N drawn in Eq. (2.5) is equal to 10^9. We can therefore use jackknife resampling to calculate the mean and variance (Efron, 1982). We use 100 sub-samples in our jackknife resampling, which gives us a mean accurate to the sub-percent level and a variance to the percent level when using $N = 10^9$. Setting $N = 10^9$ allows us to explore the sensitivity to various prior choices.

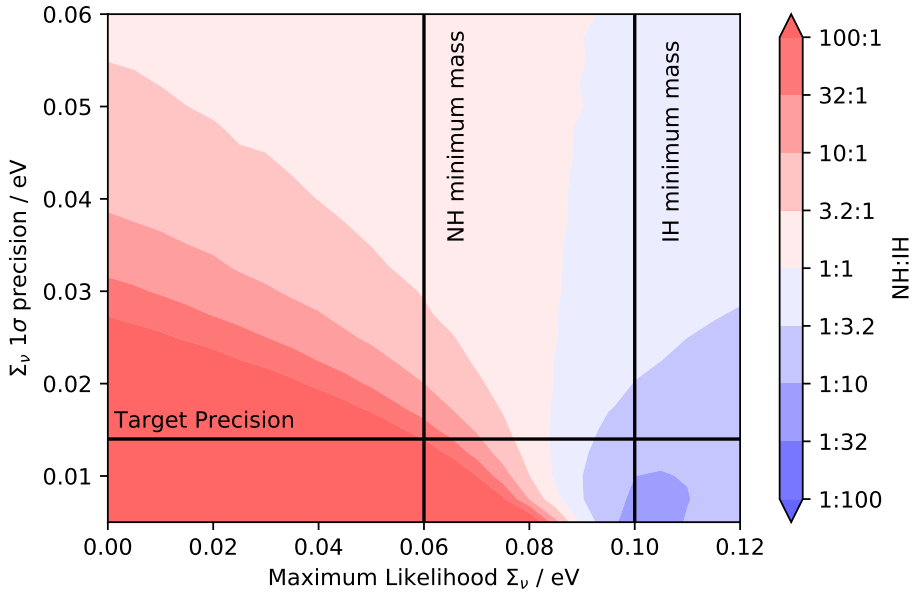

Figure 2.2: The dependence of the NH:IH posterior odds on the value of a future measurement of the neutrino mass sum Σ_ν and its associated 1σ precision. The line at $\sigma(\Sigma_\nu) = 0.014\,\mathrm{eV}$ shows the target precision required to reach posterior odds of 100:1 in favor of the NH for a measurement at the NH minimum mass. The minimum masses are calculated from the current splitting measurements shown in Table 2.1. This plot could be extended to negative maximum likelihood values, but we are specifically interested in measurements at or close to the NH minimum mass.

2.4 Results

The posterior odds using our hierarchy-agnostic prior and current data are found to be

$$\frac{p(\mathrm{NH}|D)}{p(\mathrm{IH}|D)} = 2.66 \pm 0.04\,, \tag{2.10}$$

where the 1σ uncertainty is reported. Odds of 2.7:1 show a slight but inconclusive preference for the NH. This confirms that previous results strongly favoring the NH have been driven by the prior and not by the data (Gariazzo et al., 2018; Heavens and Sellentin, 2018).

We then turn to the question of what precision needs to be targeted by experiments in order to distinguish between the hierarchies. Since the splittings are much more accurately measured than the sum of the masses, we focus on setting a target for neutrino mass sum measurements. Figure 2.2 shows the dependence of the log posterior odds on the value of a future measurement of the neutrino mass sum Σ_ν and its associated 1σ precision. The Σ_ν likelihood is assumed to be a normal

distribution centred on the measured value. For a measurement at the NH minimum mass, 0.06 eV, the precision would need to be increased to $\sigma(\Sigma_\nu) = 0.014$ eV to determine decisively the NH with odds of 100:1. For higher masses the precision required is even greater. A precision of 0.014 eV is an order of magnitude improvement on the current Σ_ν precision. This result does not change if we include future improved mass-squared splitting measurements from DUNE and JUNO, where the 1σ precision on the mass-squared splittings is expected to improve by an order of magnitude over current results (Acciarri et al., 2015; An et al., 2016).

However, we note that the preference for the IH, shown by the blue region on the right-hand side of Fig. 2.2, is driven by the prior on the lightest neutrino mass m_a (Agostini et al., 2017; Caldwell et al., 2017; Gerbino et al., 2017). This is because if the prior favors m_a close to zero, but the sum of neutrino masses Σ_ν is measured to be close to the IH minimum mass 0.1 eV, the IH is favored over the NH. The preference for the IH (shown in Fig. 2.2) disappears if one downweights smaller masses by using a uniform prior on m_a instead of a uniform (or normal) prior on log m_a, see Fig. 2.3. As little is known about the order of magnitude of m_a, we chose to place a prior on log m_a. In spite of the prior sensitivity in this region, we have verified that our results – the posterior odds for current data and the target precision for future experiments – are robust to whether we use a prior on m_a or log m_a, see Table 2.2 and the left-hand side of Fig. 2.3. This demonstrates that our results are data-driven.

Table 2.2: Our results – the posterior odds for current data and the target precision for future experiments – vary little when we place a uniform prior on m_a instead of a log-normal prior. Our choice of a log-normal prior instead of a log-uniform prior on m_a also has little impact.

Prior on m_a (eV)	**Current Odds**	**Target Precision (eV)**
log-normal	2.66 ± 0.04	0.014
uniform log, 10^{-10}–1.1	2.66 ± 0.03	0.014
uniform, 0.0–1.1	2.83 ± 0.14	0.015

As mentioned previously, making a cosmological measurement of the neutrino mass sum requires combining multiple data sets at various epochs. Upcoming cosmological experiments which will contribute to a future measurement include: large scale structure (LSS) surveys such as the Large Synoptic Survey Telescope (LSST) and *Euclid*, which will use weak lensing and galaxy clustering to measure the matter distribution in the late-time universe; spectroscopic galaxy surveys such as the Dark Energy Spectroscopic Instrument (DESI) and the Maunakea Spectroscopic Explorer (MSE),

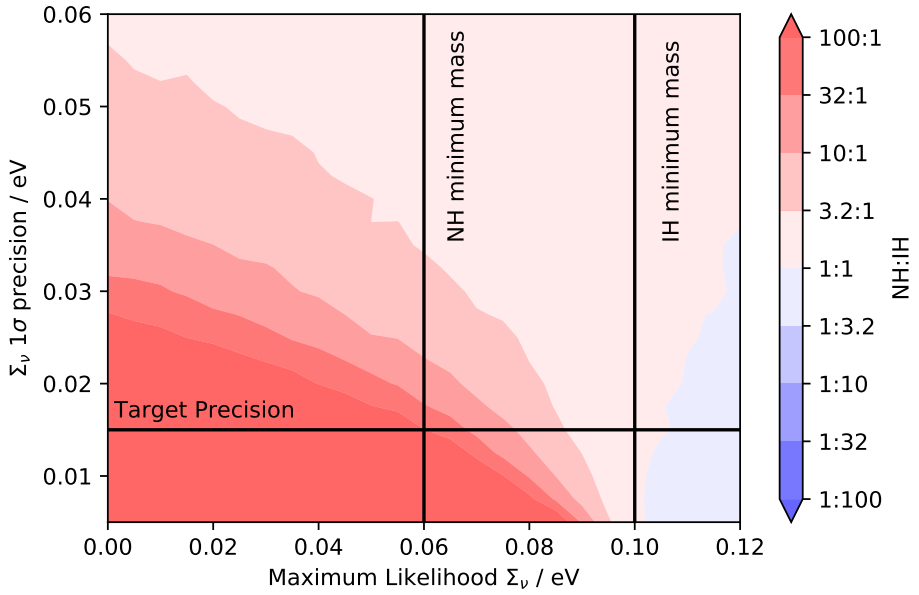

Figure 2.3: The dependence of the NH:IH posterior odds on the value of a future measurement of the neutrino mass sum Σ_ν and its associated 1σ precision, with a uniform prior between 0.0-1.1 eV on the lightest neutrino mass (instead of a log-normal prior as in Figure 2.2).

which will obtain a more accurate measurement of BAO and measure the matter distribution on smaller scales; ground-based CMB experiments such as the Simons Observatory and CMB Stage-4, which will measure fluctuations in the temperature and polarization of the CMB on smaller scales; and the CMB satellite experiment LiteBIRD, which will improve the measurement of the optical depth to reionisation τ (see introduction chapter). A number of studies have predicted the Σ_ν precision which may be attainable with these experiments, and combinations thereof (Ade et al., 2019; Aghamousa et al., 2016; Allison et al., 2015; Babusiaux et al., 2019; Brinckmann et al., 2019; Copeland et al., 2020; Errard et al., 2016; Font-Ribera et al., 2014; Laureijs et al., 2011; Mishra-Sharma et al., 2018). All of these analyses will be limited by systematic uncertainties in the Σ_ν measurement, not by statistical uncertainties. Therefore, our target precision of 0.014 eV imposes a stringent requirement on control of systematics in such analyses.

It is possible to measure the neutrino mass scale using data from particle physics as well as from cosmology. Current and upcoming experiments include: tritium beta decay experiments, such as KATRIN and *Project-8*, which aim to measure the mass of the electron anti-neutrino; and neutrinoless double beta decay experiments, such as SuperNEMO and KamLAND-Zen (Gando et al., 2016), which rely on neutrinos being their own anti-particle. These experiments involve completely

different physics and systematics modeling from the cosmological constraints. They therefore may be vital in reaching our target precision (De Salas et al., 2018; Qian and Vogel, 2015).

Current long-baseline neutrino oscillation experiments, such as T2K and NOvA, have some sensitivity to the mass hierarchy through electrons in matter affecting the neutrinos as they travel through the Earth (Tanabashi et al., 2018). These experiments previously found a slight preference for the NH (Abe et al., 2017; Acero et al., 2019), but this preference has now been reduced, leaving no clear preference for the NH (Esteban et al., 2020; Kelly et al., 2020). Heavens and Sellentin 2018 included the previous preference for the NH from long baseline neutrino oscillation experiments by scaling the surrogate likelihoods. This approach could be included in this work if a preference for the NH is re-established in the future. One of the major goals of future oscillation experiments DUNE and JUNO is to determine the mass hierarchy (Acciarri et al., 2015; An et al., 2016). These experiments are entering the construction phase but once built will have the sensitivity to provide an independent determination of the hierarchy, if sufficient neutrino interactions are recorded.

2.5 Conclusions

Combining data from neutrino oscillation experiments and cosmological probes has the potential to determine the neutrino hierarchy. In this work we developed a hierarchy-agnostic prior for a joint analysis of neutrino oscillation and cosmology data. Using current data we found odds for NH:IH of 2.7:1, which are inconclusive for determining the hierarchy. This is in contrast to previous analyses which found substantial odds in favor of the NH, demonstrating that these results were not data-driven.

We also computed the target precision, for future measurements of the neutrino mass sum, which is required to determine conclusively the NH with odds of 100:1. For a neutrino mass sum measurement at the NH minimum mass of 0.06 eV we found the precision on the neutrino mass sum would need to reach 0.014 eV. For higher masses the precision required is even greater. Future measurements of the neutrino mass sum will be systematics-limited. Therefore, our work demonstrates that an order of magnitude improvement in systematics control is needed to determine conclusively the neutrino hierarchy. While this is a challenging task, reaching this goal will be essential for our understanding of the Beyond Standard Model properties of the neutrino sector.

3

Forecasting the Potential of Weak Lensing Magnification at LSST

3.1 Introduction

As light from distant galaxies travels towards telescopes it is deflected gravitationally by intervening matter. This means that galaxy images appear distorted. On average, the distortions to individual galaxy images are very small, but when combined they can be used to map statistically the matter distribution in the universe. This technique is called weak gravitational lensing.

Weak gravitational lensing distorts both the shape and size of galaxy images. Statistical measurements of the shape distortions are referred to as cosmic shear, and statistical measurements of the size distortions are referred to as magnification. Making a magnification measurement, which directly uses size information is challenging because there is a large intrinsic variation in the sizes of galaxies. However, Schmidt et al. (2011) achieved a magnification measurement using the joint distribution of galaxy sizes and magnitudes, and there are developing techniques which anchor the size distribution using the fundamental plane of galaxies (Freudenburg et al., 2019; Huff and Graves, 2013). Most magnification analyses therefore focus on making a magnification measurement using galaxy number density information. In a flux limited survey, distortions to the size of galaxy images affect the observed number density of galaxies for two reasons:

1. Since surface brightness is conserved by lensing if the observed size of a galaxy is increased so is its observed flux. This means that galaxies previously too faint to be observed by a galaxy survey become observable. The number density of galaxies is increased.

2. It is not only the observed size of individual galaxies which is increased by magnification but the observed size of the whole patch of sky behind the lens. This means that the observable

separation between galaxies behind the lens increases and there is a dilution in the number density of galaxies.

These two effects compete and contribute to an overall fluctuation in the number density of galaxies, as a result of weak lensing magnification.

Weak lensing using cosmic shear has been a highly successful technique. In recent years there have been increasingly precise results using cosmic shear from galaxy surveys such as the Kilo Degree Survey (KiDS) (Hildebrandt et al., 2020; Joudaki et al., 2018; van Uitert et al., 2018), the Dark Energy Survey (DES) (Abbott et al., 2018; Troxel et al., 2018) and the Hyper Suprime-Cam Survey (HSC) (Hikage et al., 2019). Weak lensing magnification has not been included in standard weak lensing analyses to date. All that has been included is the sensitivity of results to including a simplified magnification model (Abbott et al., 2019). The reasoning is, magnification provides similar information to that of cosmic shear and has poorer signal to noise (Bartelmann, 2010). However, due to improvements in statistical precision, recent works have shown that cosmological results from upcoming surveys such as the Vera Rubin Observatory Legacy Survey of Space and Time (LSST) and *Euclid* will be biased if the effects of weak lensing magnification are not included (Cardona et al., 2016; Duncan et al., 2014; Lorenz et al., 2018; Thiele et al., 2019).

These works have shown that magnification must be included in future surveys to avoid bias, but the aim of this work is to determine whether including magnification as a complementary probe can also improve the final precision of the LSST weak lensing results. Duncan et al. (2014) and Lorenz et al. (2018) found no increase in precision from including magnification in a weak lensing analysis, however LSST is a special case. LSST is a very deep ground-based galaxy survey. This means that there will be a lot of very faint, small and distant galaxies, which will be poorly resolved. It will therefore not be possible to measure the shape of these galaxies, for use in a cosmic shear analysis, but it may be possible to count them for a weak lensing magnification analysis. This means that the potentially usable sample size for weak lensing magnification is significantly larger than that for cosmic shear, and as such it is worth investigating magnification's potential as a complementary probe in the case of LSST.

In summary, we wish to determine the effect of including weak lensing magnification on the precision of the final constraints from LSST weak lensing. We determine this using the Fisher matrix formalism introduced in section 3.2. We then describe the modelling of the observables (weak lensing power spectra and the galaxy luminosity function) in sections 3.3 and 3.4. We describe the details of our LSST specific survey modelling in section 3.5. We verify the stability of our Fisher

matrices in section 3.6; and present our results and conclusions in sections 3.7 and 3.8.

3.2 Fisher Analysis

The Fisher Information matrix summarises the expected curvature of the log-Likelihood function around its maximum,

$$F_{ij} = \left\langle \frac{-\partial^2 \ln L}{\partial\theta_i \partial\theta_j} \right\rangle , \tag{3.1}$$

where L is the likelihood and θ_i is a model parameter. If the likelihood function is sharply peaked for a given parameter, the parameter is tightly constrained by the data (Dodelson, 2003). The marginal uncertainty on the model parameter θ_i can be calculated from the Fisher matrix as,

$$\Delta\theta_i \geq \sqrt{(F^{-1})_{ii}} \, . \tag{3.2}$$

The greater than or equal relation is in reference to the Cramér-Rao inequality, which specifies that the Fisher matrix gives the minimum possible uncertainty on an unbiased estimate of a model parameter (Tegmark et al., 1997).

The Fisher information matrix can be calculated without data and is therefore a useful tool for forecasting best-case parameter constraints. In the case of a Gaussian likelihood function and a parameter independent covariance matrix the Fisher matrix is given by,

$$F_{ij} = \sum_{\ell} \frac{\partial C_\ell}{\partial\theta_i} \, \mathrm{Cov}^{-1} \, \frac{\partial C_\ell}{\partial\theta_j} \, , \tag{3.3}$$

where C is the theory datavector and Cov is the associated covariance (Tegmark et al., 1997). In this work we consider two component Fisher matrices, which we then add together since they concern separate observables: the Fisher matrix where the theory datavector consists of the weak lensing observables (detailed in section 3.3) and the Fisher matrix where the theory datavector consists of the galaxy luminosity function (detailed in section 3.4). The associated covariances are detailed in sections 3.5.5 and 3.5.2 respectively.

3.3 Weak Lensing Observables

The two observable quantities used in this weak lensing analysis are the shape, often referred to as ellipticity, and number density of galaxy images. Since weak lensing is a local effect the mean ellipticity ϵ and fluctuation in the number density of galaxies n, resulting from weak lensing, is equal to zero when averaged over large scales. Therefore, the key statistical quantity used in weak lensing analyses is the two-point correlation function (see section 1.2.2 for further details). There are three two-point correlation functions commonly considered in large-scale structure and weak lensing analyses; cosmic shear (ellipticity-ellipticity), angular galaxy clustering (number density-number density) and galaxy-galaxy lensing (number density-ellipticity). These two-point correlation functions can be considered as individual probes or combined together into a joint analysis, commonly referred to as '3x2pt'. Performing a joint analysis is desirable as it helps to control uncertainties in the measurement, since the two-point functions are subject to different systematic effects and have different sensitivity to the cosmological parameters.

The Fourier transform of the two-point correlation function for cosmic shear is given by,

$$\langle \tilde{\epsilon}^i(\boldsymbol{\ell})\tilde{\epsilon}^j(\boldsymbol{\ell'})\rangle = (2\pi)^2\delta^{(2)}(\boldsymbol{\ell}+\boldsymbol{\ell'})C^{ij}_{\epsilon\epsilon}(\ell)\ , \tag{3.4}$$

where $\tilde{\epsilon}$ is the Fourier transform of the ellipticity, $\boldsymbol{\ell}$ is the angular frequency, $\delta^{(2)}$ is the two-dimensional Dirac delta function and $C^{ij}_{\epsilon\epsilon}$ is the projected ellipticity power spectrum between redshift bins i and j (Joachimi and Bridle, 2010). It is useful to work in Fourier space because it simplifies linking to the theory predictions. The galaxy samples used for weak lensing are often split into redshift bins; a technique called redshift tomography. This binning enables weak lensing to probe the evolution of the power spectrum with time, through auto- and cross-correlations between the different redshift bins, and hence study the expansion of the universe and dark energy.

The Fourier space two-point correlation function for angular galaxy clustering is given by,

$$\langle \tilde{n}^i(\boldsymbol{\ell})\tilde{n}^j(\boldsymbol{\ell'})\rangle = (2\pi)^2\delta^{(2)}(\boldsymbol{\ell}+\boldsymbol{\ell'})C^{ij}_{\mathrm{nn}}(\ell)\ , \tag{3.5}$$

where $\tilde{n}$ is the Fourier transform of the number density contrast and C^{ij}_{nn} is the projected number density power spectrum between redshift bins i and j. The Fourier space two-point correlation function for galaxy-galaxy lensing is given by,

$$\langle \tilde{n}^i(\boldsymbol{\ell})\tilde{\epsilon}^j(\boldsymbol{\ell'})\rangle = (2\pi)^2\delta^{(2)}(\boldsymbol{\ell}+\boldsymbol{\ell'})C^{ij}_{\mathrm{n}\epsilon}(\ell)\ , \tag{3.6}$$

where $C^{ij}_{\mathrm{n}\epsilon}$ is the projected number density-ellipticity power spectrum between redshift bins i and j. In this work we focus on angular galaxy clustering as an individual probe and a quasi 3x2pt analysis, described in section 3.7.

3.3.1 2D Power Spectra

The key quantities in equations 3.4, 3.5 and 3.6 are the two-dimensional (2D) power spectra $C_{\epsilon\epsilon}$, C_{nn} and $C_{\mathrm{n}\epsilon}$. These are the observables we model to include in our Fisher matrix theory datavector, see section 3.2.

In this work we model the 2D observable power spectra $C_{\epsilon\epsilon}$, C_{nn} and $C_{\mathrm{n}\epsilon}$ by breaking them down into their constituent parts. The observed ellipticity of a galaxy comes from a combination of the intrinsic shear of the galaxy before it is lensed γ_I (the intrinsic alignment, see Joachimi et al. 2015 for a review), the distortion of the shape by weak lensing shear γ_G and a random shape noise component ϵ_{rnd},

$$\epsilon^i(\boldsymbol{\theta}) = \gamma^i_G(\boldsymbol{\theta}) + \gamma^i_I(\boldsymbol{\theta}) + \epsilon^i_{\mathrm{rnd}}(\boldsymbol{\theta}) \ , \tag{3.7}$$

where i denotes the redshift bin. The observed number density of galaxies comes from a combination of the number density fluctuation of galaxies as a result of galaxy clustering n_g, the distortion to the number density from weak lensing magnification n_m, and a random shot noise component n_{rnd},

$$n^i(\boldsymbol{\theta}) = n^i_g(\boldsymbol{\theta}) + n^i_m(\boldsymbol{\theta}) + n^i_{\mathrm{rnd}}(\boldsymbol{\theta}) \ . \tag{3.8}$$

In terms of the Fourier space 2D power spectra the uncorrelated random components lead to noise power spectra, and separating out the remaining contributions gives:

$$\begin{aligned} C^{ij}_{\epsilon\epsilon}(\ell) &= C^{ij}_{\mathrm{GG}}(\ell) + C^{ij}_{\mathrm{IG}}(\ell) + C^{ji}_{\mathrm{IG}}(\ell) + C^{ij}_{\mathrm{II}}(\ell) \ , \\ C^{ij}_{\mathrm{nn}}(\ell) &= C^{ij}_{\mathrm{gg}}(\ell) + C^{ij}_{\mathrm{gm}}(\ell) + C^{ji}_{\mathrm{gm}}(\ell) + C^{ij}_{\mathrm{mm}}(\ell) \ , \\ C^{ij}_{\mathrm{n}\epsilon}(\ell) &= C^{ij}_{\mathrm{gG}}(\ell) + C^{ij}_{\mathrm{gI}}(\ell) + C^{ij}_{\mathrm{mG}}(\ell) + C^{ij}_{\mathrm{mI}}(\ell) \ , \end{aligned} \tag{3.9}$$

where G represents ellipticity from weak lensing shear, I ellipticity from the intrinsic alignment of galaxies, g number density fluctuations as a results of intrinsic galaxy clustering and m number density fluctuations as a result of weak lensing magnification.

We compute all these two-dimensional power spectra C_{ab} from their associated three-dimensional

power spectra $P_{\rm ab}$ using the Limber approximation in Fourier space (Kaiser, 1992):

$$
\begin{aligned}
C^{ij}_{\rm GG}(\ell) &= \int_0^{\chi_{\rm hor}} {\rm d}\chi \frac{q^i(\chi) q^j(\chi)}{f_K^2(\chi)} P_{\delta\delta}\left(k = \frac{\ell + 1/2}{f_K(\chi)}, \chi\right) , \\
C^{ij}_{\rm IG}(\ell) &= \int_0^{\chi_{\rm hor}} {\rm d}\chi \frac{p^i(\chi) q^j(\chi)}{f_K^2(\chi)} P_{{\rm I}\delta}\left(k = \frac{\ell + 1/2}{f_K(\chi)}, \chi\right) , \\
C^{ij}_{\rm II}(\ell) &= \int_0^{\chi_{\rm hor}} {\rm d}\chi \frac{p^i(\chi) p^j(\chi)}{f_K^2(\chi)} P_{\rm II}\left(k = \frac{\ell + 1/2}{f_K(\chi)}, \chi\right) , \\
C^{ij}_{\rm gg}(\ell) &= \int_0^{\chi_{\rm hor}} {\rm d}\chi \frac{p^i(\chi) p^j(\chi)}{f_K^2(\chi)} P_{\rm gg}\left(k = \frac{\ell + 1/2}{f_K(\chi)}, \chi\right) , \\
C^{ij}_{\rm gm}(\ell) &= 2(\alpha^j - 1) C^{ij}_{\rm gG}(\ell) , \\
C^{ij}_{\rm mm}(\ell) &= 4(\alpha^i - 1)(\alpha^j - 1) C^{ij}_{\rm GG}(\ell) , \\
C^{ij}_{\rm gG}(\ell) &= \int_0^{\chi_{\rm hor}} {\rm d}\chi \frac{p^i(\chi) q^j(\chi)}{f_K^2(\chi)} P_{{\rm g}\delta}\left(k = \frac{\ell + 1/2}{f_K(\chi)}, \chi\right) , \\
C^{ij}_{\rm gI}(\ell) &= \int_0^{\chi_{\rm hor}} {\rm d}\chi \frac{p^i(\chi) p^j(\chi)}{f_K^2(\chi)} P_{\rm gI}\left(k = \frac{\ell + 1/2}{f_K(\chi)}, \chi\right) , \\
C^{ij}_{\rm mG}(\ell) &= 2(\alpha^i - 1) C^{ij}_{\rm GG}(\ell) , \\
C^{ij}_{\rm mI}(\ell) &= 2(\alpha^i - 1) C^{ij}_{\rm GI}(\ell) ,
\end{aligned}
\tag{3.10}
$$

where χ is the comoving distance, $f_K(\chi)$ is the comoving angular diameter distance, $p^i(\chi)$ is the probability distribution of galaxies in redshift bin i, and α is defined below. $q^i(\chi)$ is a weight function given by,

$$
q^i(\chi) = \frac{3 H_0^2 \Omega_{\rm m}}{2c^2} \frac{f_K(\chi)}{a(\chi)} \int_\chi^{\chi_{\rm hor}} {\rm d}\chi' p^i(\chi') \frac{f_K(\chi' - \chi)}{f_K(\chi')} , \tag{3.11}
$$

for further details see Bartelmann and Schneider (2001). The calculation of the three-dimensional power spectra P_{ab} is detailed in the following section.

The equations in 3.10 show that the 2D power spectra associated with magnification $C_{\rm gm}$, $C_{\rm mm}$, $C_{\rm mG}$ and $C_{\rm mI}$ can be computed from the 2D power spectra associated with weak lensing shear $C_{\rm gG}$, $C_{\rm GG}$ and $C_{\rm IG}$ using the faint end slope of the galaxy luminosity function α^i. We discuss the galaxy luminosity function in section 3.4 but detail the relationship between the magnification and shear power spectra here.

As mentioned previously weak lensing magnification contributes to fluctuations in the number density of galaxies n. If the number density of galaxies above the flux limit f is $N_0(> f)$

magnification alters the number density of sources as,

$$N(>f) = \frac{1}{\mu} N_0(>f/\mu)\ , \tag{3.12}$$

where $N(>f)$ is the observed number density of sources and μ is the local magnification factor (see the introduction chapter for details of the origin of μ) (Bartelmann and Schneider, 2001). If the number density of galaxies is assumed to follow a power law $N_0(>f) = kf^{-\alpha}$ near the flux limit of the survey then,

$$N(>f) = \frac{1}{\mu} k \left(\frac{f}{\mu}\right)^{-\alpha} = N_0(>f)\mu^{\alpha-1}. \tag{3.13}$$

This means the fluctuation in the observed number density of galaxies as a result of magnification n_m is given by,

$$n_m = \frac{N - N_0}{N_0} = \mu^{\alpha-1} - 1 \approx (1+2\kappa)^{\alpha-1} - 1 \approx 2(\alpha-1)\kappa, \tag{3.14}$$

where the weak lensing limit $\mu \approx 1 + 2\kappa$ has been employed (see section 1.3.1 for details).

3.3.2 3D Power Spectra

The only 3D power spectrum $P_{\rm ab}$ in equation 3.10 that is currently well modelled is the non-linear matter power spectrum $P_{\delta\delta}$. $P_{\delta\delta}$ summarises the clustering of matter in the universe and can be derived numerically using the Boltzmann equations. In this work we compute $P_{\delta\delta}$ using the Boltzmann code CAMB (Howlett et al., 2012; Lewis et al., 2000). To include non-linear corrections we use HALOFIT (Takahashi et al., 2012). The remaining power spectra in eq. 3.10 are $P_{\rm I\delta}$, $P_{\rm II}$, $P_{\rm gg}$, $P_{\rm g\delta}$ and $P_{\rm gI}$. $P_{\rm gg}$ summarises the clustering of galaxies; $P_{\rm II}$ is the intrinsic alignment power spectra; and $P_{\rm I\delta}$, $P_{\rm g\delta}$ and $P_{\rm gI}$ summarise the cross-correlations between galaxies, matter and intrinsic alignments. These power spectra can all be related to the matter power spectrum.

In this work we employ a halo model formalism to calculate $P_{\rm gg}$, $P_{\rm II}$, $P_{\rm I\delta}$, $P_{\rm g\delta}$ and P_{gI}. This model assumes that dark matter clusters into dark matter halos and that all dark matter exists within dark matter halos. Galaxies are then assumed to form within these dark matter halos and hence the galaxy distribution traces the distribution of dark matter. The model relies on two ingredients, the underlying distribution of dark matter and how galaxies populate dark matter halos.

The dark matter distribution is summarized by: the halo mass function, which gives the number

density of dark matter halos with mass M at redshift z; the halo bias function, which accounts for dark matter halos being biased tracers of the underlying dark matter distribution; and the halo density profile, which summarises how mass is distributed within dark matter halos. In this work we use the Tinker et al. (2010) functional forms for the halo mass function and halo bias function, and assume that the density of dark matter halos follows the Navarro-Frenk-White distribution (Navarro et al., 1996). We compute the halo mass function using the publicly available python package *hmf*[1] (Murray et al., 2013).

We summarise the second ingredient, how galaxies populate dark matter halos, using the conditional luminosity function (CLF) (Cacciato et al., 2013; van den Bosch et al., 2013; Yang et al., 2003). The CLF gives the average number of galaxies with a luminosity L between $L \pm \mathrm{d}L/2$ in a halo of mass M. It is divided into two parts:

$$\Phi(L|M) = \Phi_{\rm c}(L|M) + \Phi_{\rm s}(L|M) \ , \tag{3.15}$$

where $\Phi_{\rm c}(L|M)$ is the CLF for central galaxies and $\Phi_{\rm s}(L|M)$ is the CLF for satellite galaxies. Central galaxies reside at the centre of dark matter halos and satellite galaxies orbit around them. Following the approach detailed in Cacciato et al. (2013) we take the CLF of central galaxies to be modelled by a lognormal distribution,

$$\Phi_{\rm c}(L|M)\mathrm{d}L = \frac{\log e}{\sqrt{2\pi}\sigma_{\rm c}} \exp\left[- \frac{(\log L - \log L_{\rm c})^2}{2\sigma_{\rm c}^2} \right] \frac{\mathrm{d}L}{L} \ , \tag{3.16}$$

where $\sigma_{\rm c}$ represents the scatter in the log luminosity of central galaxies and $L_{\rm c}$ is parametrised as,

$$L_{\rm c}(M) = L_0 \frac{(M/M_1)^{\gamma_1}}{[1 + (M/M_1)]^{\gamma_1 - \gamma_2}} \ . \tag{3.17}$$

$L_0 = 2^{\gamma_1 - \gamma_2} L_{\rm c}(M_1)$ is a normalisation and M_1 is a characteristic mass scale. The CLF of satellite galaxies is modelled by a modified Schechter function,

$$\Phi_{\rm s}(L|M)\mathrm{d}L = \phi_{\rm s}^* \left(\frac{L}{L_{\rm s}^*} \right)^{\alpha_{\rm s}+1} \exp\left[- \left(\frac{L}{L_{\rm s}^*} \right)^2 \right] \frac{\mathrm{d}L}{L} \ . \tag{3.18}$$

where $\alpha_{\rm s}$ is the faint end slope of the satellite luminosity function. $\phi_{\rm s}^*$ is parametrised as,

$$\log[\phi_{\rm s}^*(M)] = b_0 + b_1(\log M_{12}) + b_2(\log M_{12})^2, \tag{3.19}$$

[1] https://github.com/steven-murray/hmf

where $M_{12} = M/(10^{12}h^{-1}M_{\odot})$ and $L_{\rm s}^{*}$ is parametrised as,

$$L_{\rm s}^{*}(M) = 0.562 L_{\rm c}(M) \ . \tag{3.20}$$

Both of the functional forms in eq. 3.16 and 3.18 are derived from the SDSS galaxy group catalog in Yang et al. (2008). In total we have nine free parameters in our CLF model: $\log M_1$, $\log L_0$, γ_1, γ_2, $\sigma_{\rm c}$, $\alpha_{\rm s}$, b_0, b_1 and b_2. We include all of these parameters in our Fisher matrix.

Next we detail how to calculate the 3D power spectra $P_{\rm gg}$ and $P_{{\rm g}\delta}$ from the CLF. First the power spectra can be split into contributions from the one-halo (1h) and two-halo (2h) terms. The 1h term describes the clustering of galaxies on small scales within the same dark matter halo and the 2h term describes the clustering of galaxies on large scales between different halos. These contributions can then be split into the contributions from central c and satellite s galaxies, as with the CLF. This gives,

$$\begin{aligned} P_{\rm gg} &= 2P_{\rm cs}^{\rm 1h} + P_{\rm ss}^{\rm 1h} + P_{\rm cc}^{\rm 2h} + 2P_{\rm cs}^{\rm 2h} + P_{\rm ss}^{\rm 2h} \ , \\ P_{{\rm g}\delta} &= P_{{\rm c}\delta}^{\rm 1h} + P_{{\rm s}\delta}^{\rm 1h} + P_{{\rm c}\delta}^{\rm 2h} + P_{{\rm c}\delta}^{\rm 2h} \ . \end{aligned} \tag{3.21}$$

Note that there is no 1h term for central galaxies, as by definition there is only one central galaxy in a halo. These contributions can be calculated using,

$$\begin{aligned} P_{\rm xy}^{\rm 1h}(k,z) &= \int \mathcal{H}_{\rm x}(k,M,z)\mathcal{H}_{\rm y}(k,M,z)n(M,z){\rm d}M \ , \\ P_{\rm xy}^{\rm 2h}(k,z) &= \int {\rm d}M_1 \mathcal{H}_{\rm x}(k,M_1,z)n(M_1,z) \\ &\quad \times \int {\rm d}M_2 \mathcal{H}_{\rm y}(k,M_2,z)n(M_2,z)Q(k|M_1,M_2,z) \ , \end{aligned} \tag{3.22}$$

where x and y can be c, s or δ. $n(M,z)$ is the halo mass function mentioned above. $Q(k|M_1,M_2,z)$ accounts for the clustering of halos of mass M_1 and M_2, and incorporates the halo bias mentioned above (for further details see van den Bosch et al. 2013). $\mathcal{H}$ is defined as,

$$\begin{aligned} \mathcal{H}_{\delta}(k,M,z) &= \frac{M}{\bar{\rho}_{\rm m}}\tilde{u}_{\rm h}(k|M,z) \ , \\ \mathcal{H}_{\rm c}(k,M,z) &= \mathcal{H}_{\rm c}(M,z) = \frac{\langle N_{\rm c}|M\rangle}{\bar{n}_{\rm g}(z)} \ , \\ \mathcal{H}_{\rm s}(k,M,z) &= \frac{\langle N_{\rm s}|M\rangle}{\bar{n}_{\rm g}(z)}\tilde{u}_{\rm s}(k|M,z) \ . \end{aligned} \tag{3.23}$$

where $\tilde{u}_{\rm h}$ is the Fourier transform of the normalised density distribution of dark matter in a halo

of mass M (mentioned above), and $\tilde{u}_{\rm s}$ is the normalised number density distribution of satellite galaxies in a halo of mass M. $\langle N_{\rm c}|M\rangle$ and $\langle N_{\rm s}|M\rangle$ are the average number of central and satellite galaxies in a halo of mass M with luminosity in a given interval, and $\bar{n}_{\rm g}$ is the average number density of galaxies across all halo masses in a given luminosity interval. $\langle N_{\rm c}|M\rangle$, $\langle N_{\rm s}|M\rangle$ and $\bar{n}_{\rm g}$ are calculated using the CLF,

$$\langle N_{\rm x}|M\rangle = \int_{L_1}^{L_2} \Phi_{\rm x}(L|M){\rm d}L \ , \tag{3.24}$$

where x can be c, s or g=c+s,

$$\bar{n}_{\rm g}(z) = \int \langle N_{\rm g}|M\rangle n(M,z){\rm d}M \ . \tag{3.25}$$

To calculate the 3D power spectra $P_{\rm II}$ and $P_{{\rm I}\delta}$ we employ the empirical Non-linear Linear Alignment (NLA) model (Bridle and King, 2007). This model links the strength of the tidal field when a galaxy forms to the intrinsic ellipticity of the galaxy. This gives,

$$\begin{aligned} P_{\delta{\rm I}}(k,z) &= -A_{\rm IA}C_1\rho_{\rm c}\frac{\Omega_{\rm m}}{D(z)}P_{\delta\delta} \ , \\ P_{\rm II}(k,z) &= \left(A_{\rm IA}C_1\rho_{\rm c}\frac{\Omega_{\rm m}}{D(z)}\right)^2 P_{\delta\delta} \ , \end{aligned} \tag{3.26}$$

where C_1 is a normalisation constant and $D(z)$ the linear growth factor. $C_1\rho_{\rm c}$ is set to be 0.0134, a reference value based on the intrinsic alignment amplitude measured at low redshifts on SuperCOSMOS (Bridle and King, 2007; Hirata and Seljak, 2004), and $A_{\rm IA}$ captures the amplitude of the deviation from this reference case. We take $A_{\rm IA}$ as a free parameter in our Fisher matrix. The NLA model is sufficiently flexible for current studies but in Fortuna et al. (2020) they found for upcoming surveys, such as LSST, it can lead to a 1σ bias on Ω_m. In Fortuna et al. (2020) they employ the NLA model on large scales and then use the halo model formalism to compute $P_{\rm II}$ and $P_{{\rm I}\delta}$ on small scales. Implementing this modelling could be a future extension for this work.

3.4 Galaxy Luminosity Function

The second part of our Fisher matrix theory datavector, see section 3.2, is the galaxy luminosity function. The galaxy luminosity function describes the distribution of luminosities in a galaxy sample, the number density of galaxies with a certain luminosity, and is often directly measured

from a galaxy sample. As specified in Cacciato et al. (2013) the galaxy luminosity function at a given redshift z can be calculated from the CLF detailed in section 3.3.2,

$$\Phi(L,z) = \int dM\ \Phi(L|M) n(M,z)\ , \tag{3.27}$$

where $\Phi(L|M)$ is the CLF and $n(M,z)$ is the halo mass function (see section 3.3.2). In this analysis we work with a galaxy sample divided into redshift bins (labelled i and j previously) so we wish to compute the galaxy luminosity function for each redshift bin,

$$\Phi^i(L) = \int dz\ n^i(z)\Phi(L,z)\ , \tag{3.28}$$

where $\Phi^i(L)$ denotes the luminosity function of galaxies in redshift bin i, and $n^i(z)$ the redshift distribution in bin i. We include a prediction for the galaxy luminosity function in each redshift bin in our theory datavector as it helps to constrain the 9 CLF parameters detailed in section 3.3.2. The faint end slope of the galaxy luminosity function is also required to calculate the magnification 2D power spectra, see eq. 3.31.

3.5 Survey Modelling

We perform our Fisher forecast using the cosmological parameter estimation framework CosmoSIS (Zuntz et al., 2015). To calculate the 3D power spectra detailed in section 3.3.2 we use a halo model code developed by Maria Cristina Fortuna at the University of Leiden, which is the same halo model employed in Fortuna et al. (2020).

In this analysis we define two mock LSST galaxy samples; an ellipticity sample ϵ-*sample* and a number density sample *n-sample*. We use a 445 square degree mock catalog from the LSST Dark Energy Science Collaboration (DESC) Data Challenge 2 (DC2) simulations (cosmoDC2 1.1.4 Korytov et al. 2019). This catalog includes photometric redshifts for all galaxies with an i-band magnitude less than 26.5, up to redshift 3. The photometric redshifts were calculated using the template fitting code BPZ (Benitez, 2000). *n-sample* is defined as all galaxies in this mock catalog with an i-band magnitude less than 26.5 and photometric redshift greater than 0.1 and less than 2.0. We set an upper limit as the photometric redshifts degrade significantly beyond 2.0, see Fig. 3.1. ϵ-*sample* is defined as a subset of galaxies in *n-sample* with $i < 25.3$ (Fig. 3.2). This corresponds to the LSST *gold sample*, which will be used for weak lensing (LSST Science Collaboration, 2009). ϵ-*sample* is

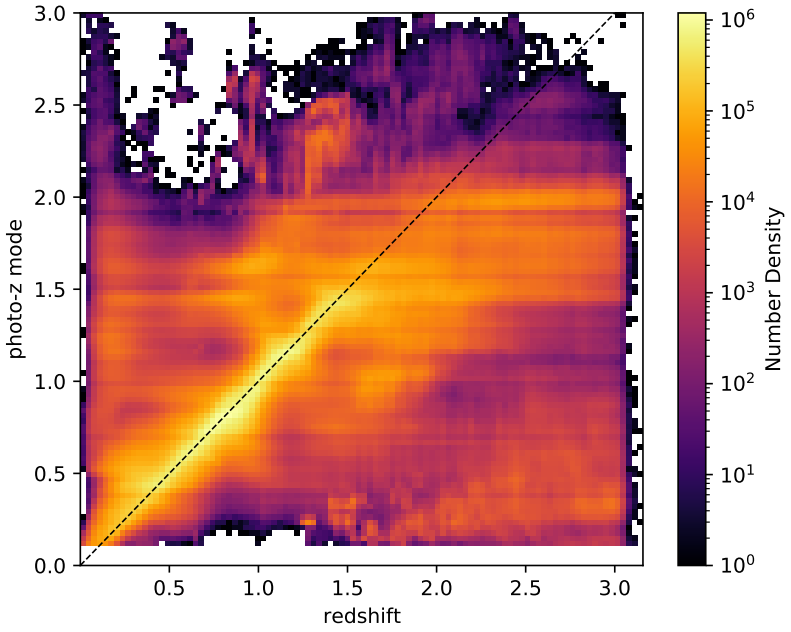

Figure 3.1: Photometric redshift point estimate mode against true redshift for the number density sample *n-sample*.

defined to be shallower than *n-sample* because ellipticity measurements require higher resolution galaxy images. Galaxies in *n-sample* have a signal-to-noise > 5 and galaxies in ϵ*-sample* have a signal-to-noise > 20.

3.5.1 N(z) Distributions

To compute the 2D power spectra in eq. 3.10 and the luminosity functions in eq. 3.28 we require the redshift distribution of galaxies in each photometric redshift bin. In this work we split both the galaxy samples, *n-sample* and ϵ*-sample*, into 10 equally sized tomographic redshift bins using their photometric redshifts. Figures 3.3 and 3.4 show the resulting distribution of galaxies with redshift for each tomographic bin, as well as the tomographic bin boundaries. Figure 3.3 shows that the photometric redshifts are close to random for bin 10 of *n-sample*, so our maximum photometric redshift cut of 2.0 is well justified.

We compute the number density of galaxies in each tomographic bin to be $12.7\ \mathrm{arcmin}^{-2}$ for *n-sample* and $4.9\ \mathrm{arcmin}^{-2}$ for ϵ*-sample*. *n-sample* has a greater number density of galaxies than ϵ*-sample* because it includes fainter galaxies, due to its greater magnitude cut. However, weak

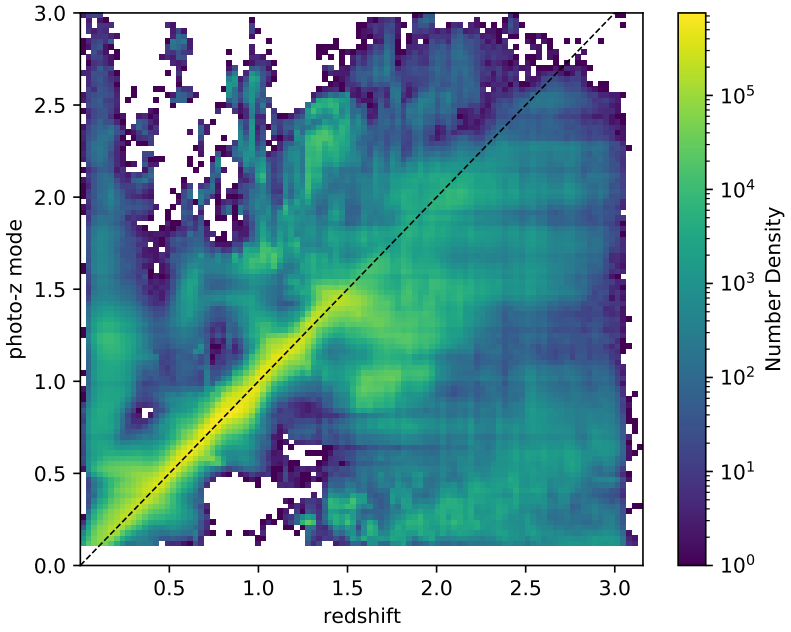

Figure 3.2: Photometric redshift point estimate mode against true redshift for the ellipticity sample *ϵ-sample*.

lensing shape measurements typically weight galaxies by signal-to-noise or ability to calibrate shape measurements, this would reduce the number density for *ϵ-sample*, especially at high redshifts.

3.5.2 Conditional Luminosity Function Fiducial Values

The Fisher matrix gives the curvature of the log-Likelihood function around its peak. It does not find the location of the peak, this is defined with a set of fiducial values (shown in Table 3.2). The set of parameters required to calculate the 3D power spectra in section 3.3.2 are the cosmological parameters and the CLF parameters. In this work we consider the constraints on a flat wCDM cosmology, and vary the cosmological parameters Ω_m, h_0, Ω_b, n_s, $A_s/10^{-9}$, w and w_a. We take their fiducial values from the input values used to generate the simulation for the LSST DESC mock catalog, or from the values obtained by the *Planck* satellite (Aghanim et al., 2018). We also vary the full set of CLF parameters $\log M_1$, $\log L_0$, γ_1, γ_2, σ_c, α_s, b_0, b_1 and b_2, detailed in section 3.3.2. In this case choosing a set of fiducial parameters is more difficult.

We find the fiducial values of the CLF parameters by measuring the luminosity functions of our mock LSST galaxy samples. We then find the CLF parameters which maximise the likelihood of the

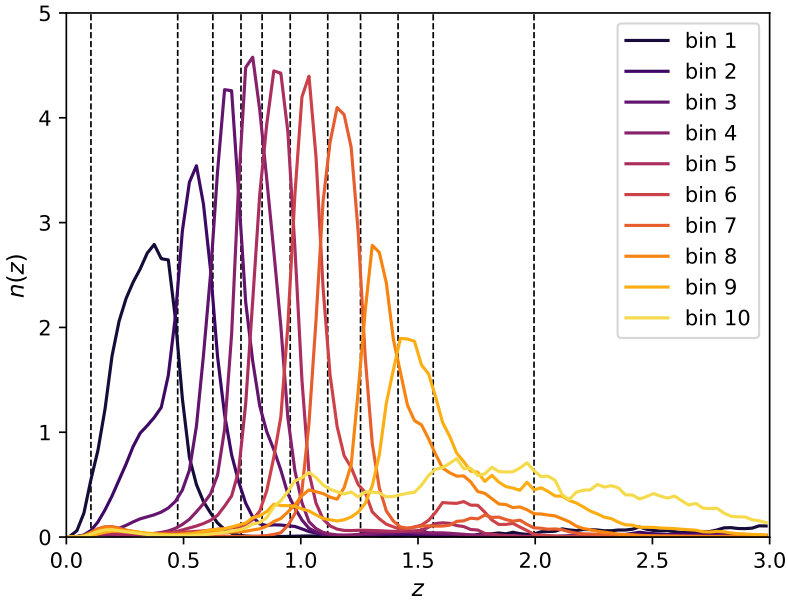

Figure 3.3: Number density of galaxies as a function of true redshift for each tomographic bin in *n-sample*. The dashed lines indicate the tomographic bin boundaries for *n-sample*.

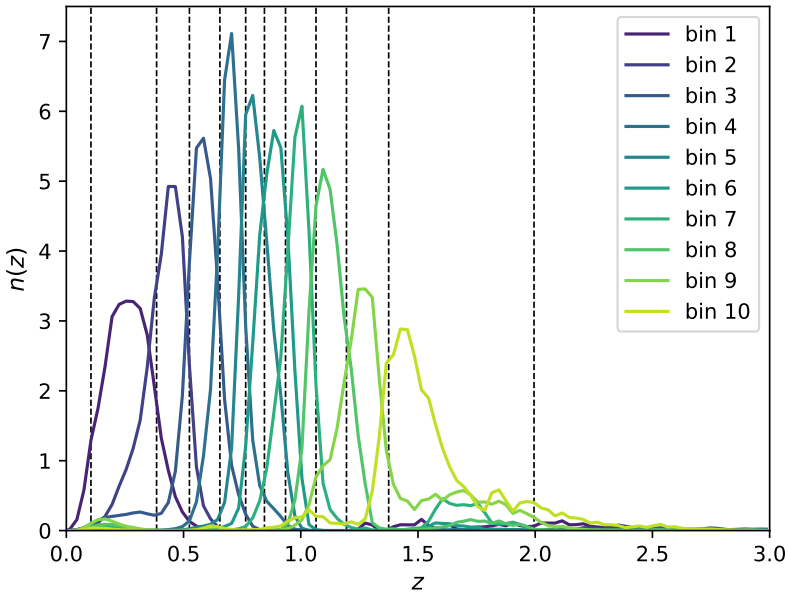

Figure 3.4: Number density of galaxies as a function of true redshift for each tomographic bin in ϵ*-sample*. The dashed lines indicate the tomographic bin boundaries for ϵ*-sample*.

luminosity function predicted by the CLF model, given our mock data. To measure the luminosity functions for *n-sample* and ϵ*-sample* we begin by computing the luminosity of each galaxy from its rest-frame absolute magnitude in the i band. We then divide our sample into the 10 tomographic bins described above and scale the luminosity function for each bin j by the volume of bin j, to convert the histogram to number density. When calculating the bin volume we assume that the galaxies do not scatter beyond the tomographic bin boundaries. This is an approximation, which figures 3.3 and 3.4 show is becoming problematic for bin 10. We bin our 10 tomographic luminosity functions using 10 luminosity bins.

Ideally, we would use the full range of galaxy luminosities in our analysis. However in order to use the low luminosity region we would need to correct our galaxy samples to be volume complete, for example through the $1/V_{max}$ method (Cole, 2011; Felten, 1976; Schmidt, 1968). High luminosity objects can be observed across the full volume of the survey, but low luminosity objects can only be observed at smaller distances. This introduces a bias referred to as Malmquist bias, and we therefore only want to include galaxies that can be observed across the whole volume of the survey. For the purposes of this work we deemed it sufficient to simply cut out the low luminosity galaxies to make the sample volume limited, since this is still a significant step forward compared to previous analyses.

A deeper sample will be volume complete to lower luminosities, so when the luminosity function of a shallower sample diverges from the luminosity function of a deeper sample, we know the shallower sample has ceased to be volume complete. We can therefore determine the volume complete luminosity cut for ϵ*-sample* by finding where it diverges from *n-sample*. Our divergence condition is,

$$\frac{|\Phi^i_\epsilon(L) - \Phi^i_{n(\epsilon)}(L)|}{\Phi^i_\epsilon(L)} > 0.2 \tag{3.29}$$

where Φ^i_ϵ is the luminosity function for ϵ*-sample* and $\Phi^i_{n(\epsilon)}$ is the luminosity function for *n-sample*, where *n-sample* has been binned using the ϵ*-sample* tomographic bins. We cut Φ^i_ϵ when there is a percentage difference of 20% from the deeper sample $\Phi^i_{n(\epsilon)}$. 20% was found to cut Φ^i_ϵ before it significantly diverged from the deeper sample whilst allowing for small deviations, see the right panel of Fig. 3.5.

Since we did not have a sample deeper than *n-sample* available to us, we made a more stringent volume complete cut on the *n-sample* luminosity function based on where the luminosity function of our shallower sample ϵ*-sample* diverged. If the shallower sample is volume complete we can be

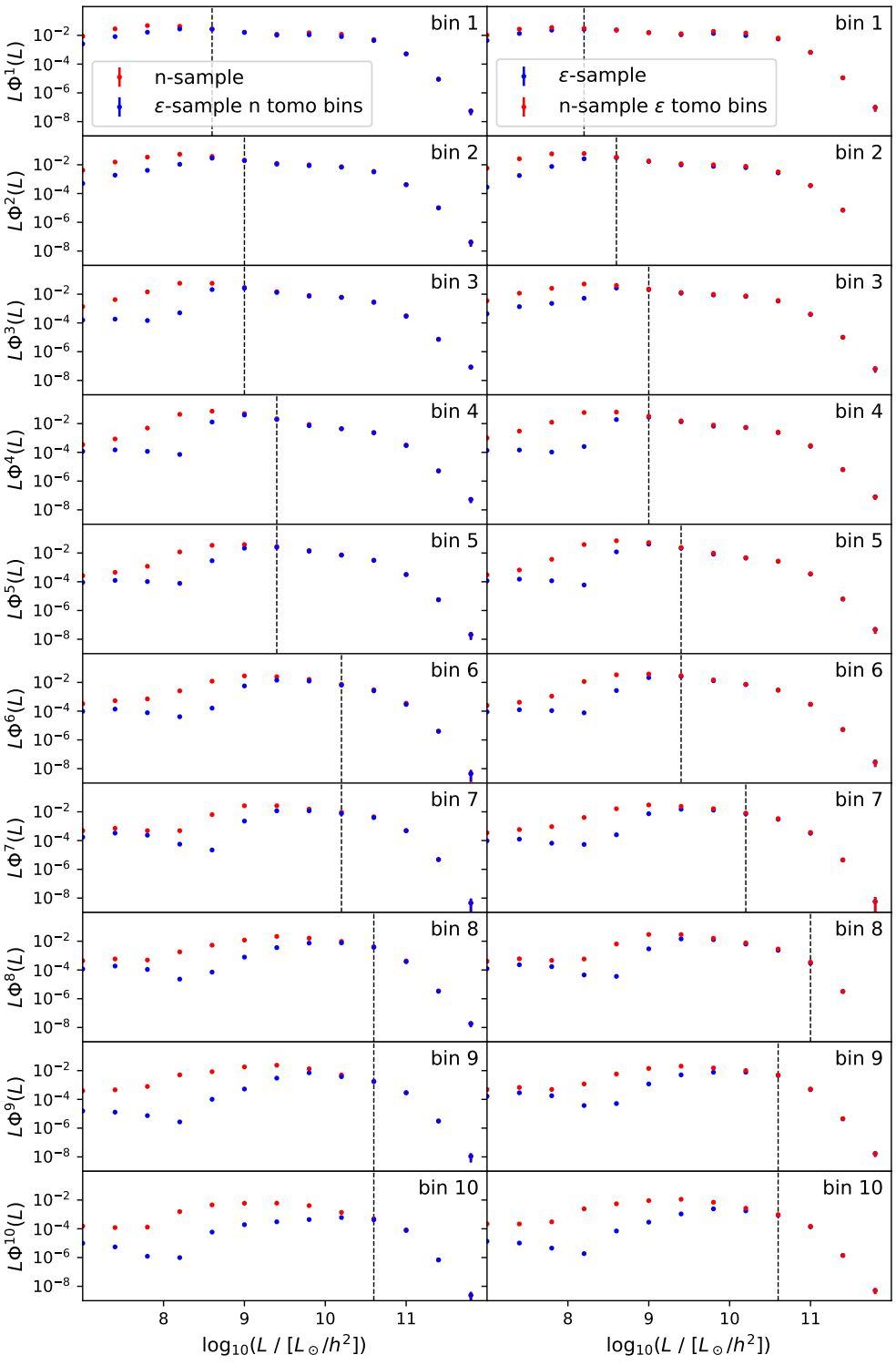

Figure 3.5: Measured luminosity functions $\Phi^i(L)$ for each photometric redshift bin in *n-sample* (left) and *ϵ-sample* (right), with associated bootstap errors. The dotted lines show the location of the luminosity cuts to *n-sample* (left) and *ϵ-sample* (right) to make sure they are volume complete, and do not introduce a bias. *ϵ-sample* n tomo bins refers to the *ϵ-sample* being binned into the *n-sample* redshift bins, and *n-sample* ϵ tomo bins refers to the *n-sample* being binned into *ϵ-sample* redshift bins. $L\Phi^i(L)$ has units of h^3/Mpc^3.

sure that the deeper sample is also volume complete. In this case our divergence condition is,

$$\frac{|\Phi_n^i(L) - \Phi_{\epsilon(n)}^i(L)|}{\Phi_n^i} > 0.2 \tag{3.30}$$

where Φ_n^i is the luminosity function for *n-sample* and $\Phi_{\epsilon(n)}^i$ is the luminosity function for *ϵ-sample*, where *ϵ-sample* has been binned using the *n-sample* tomographic bins. While this luminosity cut enforces that *n-sample* is volume complete, using a shallower sample means that the cut is much more conservative than necessary.

Before the measured luminosity functions can be used to find the maximum likelihood CLF values, we require their associated covariance. In this analysis we compute a bootstrap covariance for our measured galaxy luminosity functions. First, we sample our dataset with replacement 100 times and compute the associated datavectors. We then assume that each luminosity bin in each tomographic bin is independent (each of our datapoints is independent) and calculate the variance of these 100 samples. This gives us a diagonal covariance. The variance of the 100 samples is in general small, due to the very large numbers of galaxies in each sample. This is the covariance we use to calculate our galaxy luminosity function Fisher matrix.

Once we have measured the luminosity functions, and found their associated covariance, we can find the maximum likelihood CLF values. We assume a Gaussian likelihood, use the Nelder-Mead method in the SciPy minimize package (Virtanen et al., 2020), and use the CLF parameters obtained for the Sloan Digital Sky Survey (SDSS) by Cacciato et al. (2013) as our starting point in parameter space. Figure 3.6 shows the galaxy luminosity function predicted from the CLF using the maximum likelihood values (labelled theory) compared to the luminosity functions measured from our mock galaxy samples. The specific values obtained are given in Table 3.2. There is good agreement between the predicted luminosity function and the measured luminosity function, so we use the maximum likelihood CLF values as the fiducial values in our Fisher analysis.

The largest difference between the SDSS fiducial values found by Cacciato et al. (2013) and our maximum likelihood values is for the faint end slope of the satellite galaxy luminosity function α_s. The SDSS value for α_s is -1.18 and our maximum likelihood value is -0.18, so the satellite luminosity slope at the faint end is shallower for our deeper sample[2]. This makes sense as a survey as deep as LSST should detect all but the faintest galaxies.

[2]The SDSS sample has an SDSS r band apparent magnitude greater than 17.7

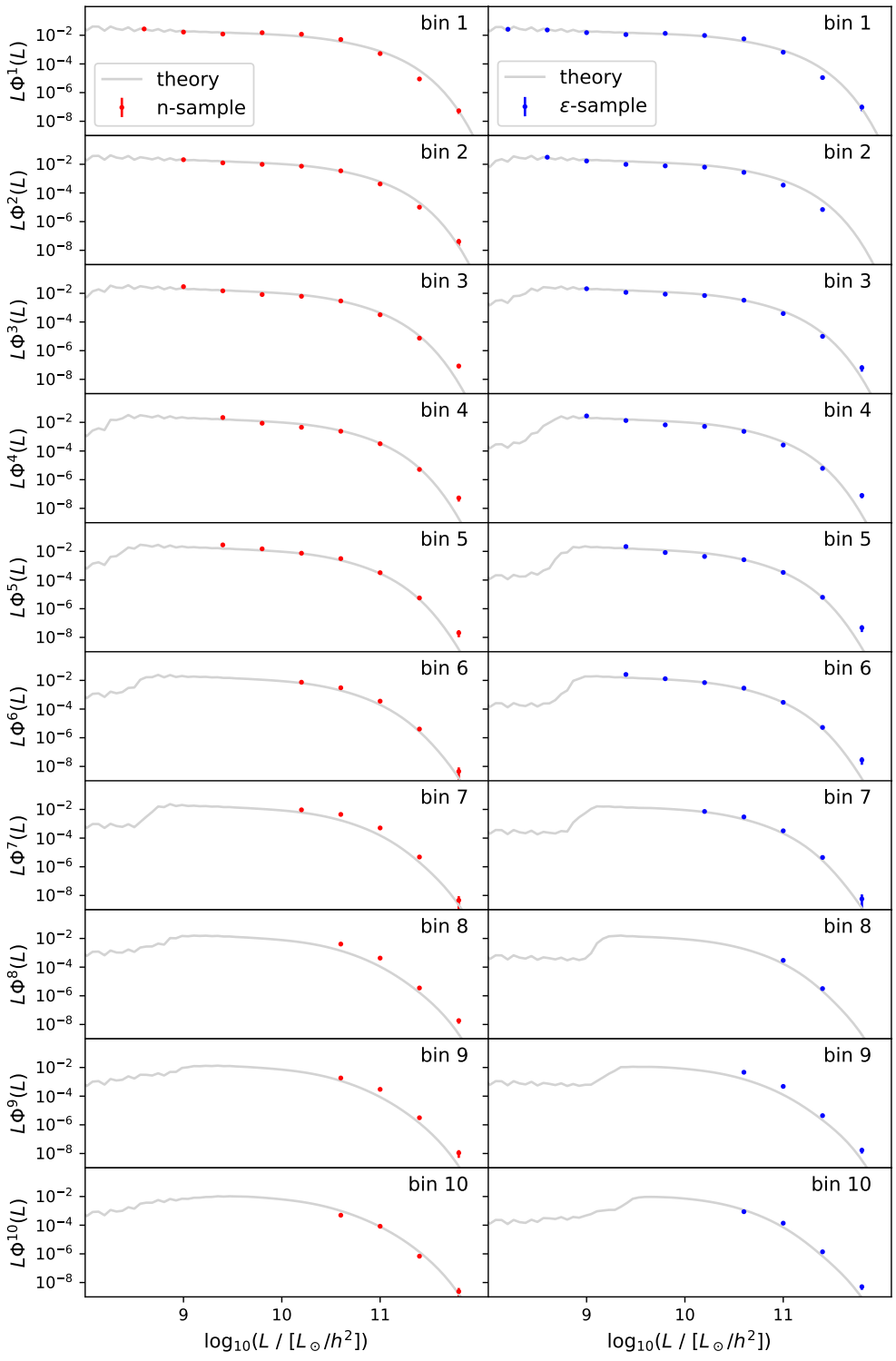

Figure 3.6: Measured luminosity functions $\Phi^i(L)$ for each photometric redshift bin in *n-sample* and *ϵ-sample* compared to the theory prediction from the Conditional Luminosity Function (CLF), where the CLF parameters that maximise the likelihood have been used as input parameters for the CLF. $L\Phi^i(L)$ has units of h^3/Mpc^3. There are no datapoints for the highest luminosity bin of *ϵ-sample* bin 2 and bin 8 due to there being no galaxies of such high luminosity in these samples.

3.5.3 Faint End Luminosity Slopes

The key quantity in determining the size of the fluctuation in the number density of galaxies as a result of weak lensing magnification is the faint end slope of the galaxy luminosity function α (see eq. 3.31). If α is equal to 1 there is no overall fluctuation but if α does not equal 1 there is either an increase or decrease in the number density of galaxies. In terms of magnitudes,

$$\alpha(i_{\rm mag}) = 2.5\frac{{\rm d}\log_{10} N(>i_{\rm mag})}{{\rm d}i_{\rm mag}} \ , \tag{3.31}$$

where $i_{\rm mag}$ represents the i band magnitude, and $N(>i_{\rm mag})$ the number of galaxies with an i band magnitude greater than $i_{\rm mag}$ (e.g. Duncan et al. 2014).

We measure the faint end slopes α from our LSST DC2 mock catalog. We compute a value α^j for each redshift bin j, in each mock sample. To compute α^j we vary the i band magnitude in eq. 3.31 and compute the cumulative number counts $N(>i_{\rm mag})$. We then fit the logarithm of $N(>i_{\rm mag})$ with a straight line, and use the slope to compute α^j. Since we are only interested in the slope at the faint end (high magnitudes) we only fit $\log_{10} N(>i_{mag})$ over the last magnitude before the sample magnitude limit; 25.5–26.5 for *n-sample*, and 24.3–25.3 for ϵ*-sample*. Figure 3.7 shows that in general this lower fit limit (marked by a dotted line) captures the value of α^j at the faint end of the sample. Increasing the lower fit limit has little effect on the value of α^j obtained, whereas decreasing the fit limit in general gives a higher value of α^j.

Table 3.4 shows the α^j values obtained for each sample and their associated uncertainties. The uncertainties come from the fit, since they were found to be much larger than the uncertainties on the values of the cumulative number counts $N(>i_{mag})$ due to the large number of galaxies in each sample. The uncertainties are very small, and would become even smaller when using the full 18000 square degree LSST area instead of a 445 square degree mock catalog. We therefore consider the α^j parameters as fixed in our forecast.

We can compare the α values in Table 3.4 to those found in Duncan et al. (2014) for the Canada–France–Hawaii Lensing Survey (CFHTLenS). In both cases α^j generally increases with redshift. CFHTLenS reaches an α^j value of approximately 1 at its i band magnitude limit of 24.7, for its highest redshift bin between 1.02 and 1.3. This roughly corresponds to α^7 and α^8 in ϵ*-sample*, where the magnitude limit of 24.7 is included in the α^j fit. Table 3.4 shows that our α^7 and α^8 values for ϵ*-sample* are consistent with CFHTLenS.

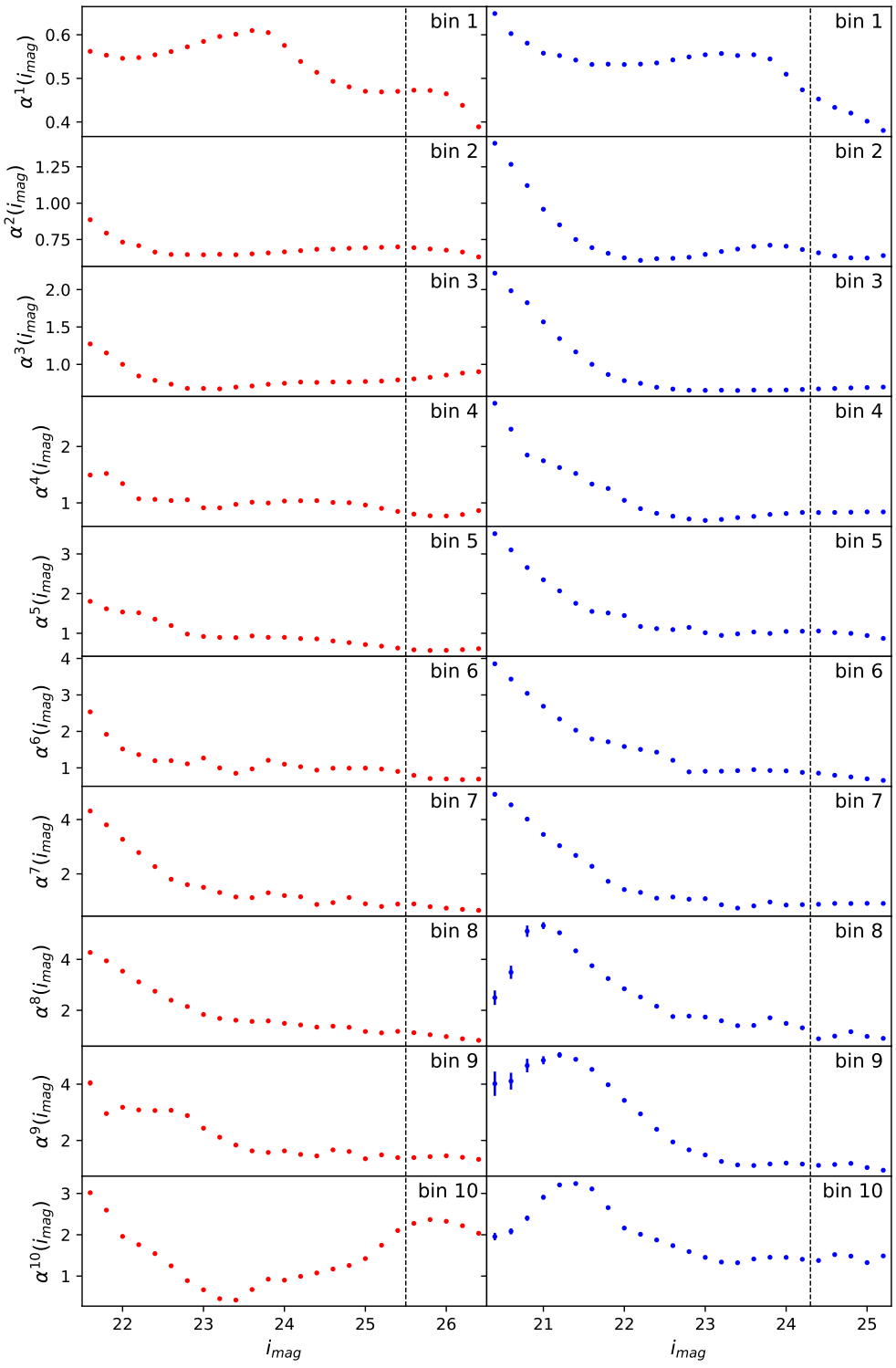

Figure 3.7: The faint end slope of the galaxy luminosity function α^i as a function of the limiting magnitude for each tomographic bin in *n-sample* (red) and ϵ-*sample* (blue). The α^i values used in this analysis were found by fitting the slope of the logarithmic cumulative number counts (see eq. 3.31) between the vertical line and the right-hand side of the figure.

Table 3.1: Faint end magnitude slopes α^j for each redshift bin j in *n-sample* and ϵ*-sample*, with their associated 1σ uncertainties.

n-sample		**ϵ-sample**	
α^1	0.445 ± 0.005	α^1	0.412 ± 0.005
α^2	0.663 ± 0.006	α^2	0.624 ± 0.004
α^3	0.848 ± 0.006	α^3	0.677 ± 0.004
α^4	0.781 ± 0.005	α^4	0.825 ± 0.006
α^5	0.573 ± 0.004	α^5	0.97 ± 0.01
α^6	0.694 ± 0.006	α^6	0.74 ± 0.01
α^7	0.74 ± 0.01	α^7	0.895 ± 0.006
α^8	0.95 ± 0.02	α^8	0.99 ± 0.01
α^9	1.39 ± 0.01	α^9	1.08 ± 0.01
α^{10}	2.24 ± 0.02	α^{10}	1.42 ± 0.01

3.5.4 Systematics

We include a number of systematics models in our analysis using nuisance parameters. For the fiducial values of these parameters and their associated priors please see Table 3.2. To apply a Gaussian prior to a particular parameter in a Fisher matrix, one simply adds $1/\sigma^2_{\rm prior}$ to the diagonal element associated with the parameter (Coe, 2009). In conceptual terms, the priors on the Fisher matrix parameters can be summarized by a diagonal covariance matrix with elements $\sigma^2_{\rm prior}$. This covariance matrix can then be inverted into a prior Fisher matrix, giving $1/\sigma^2_{\rm prior}$ diagonal elements, and added to the experimental Fisher matrix.

Shear Multiplicative Bias

Systematic uncertainties in the measuring and averaging of galaxy shapes can result in a multiplicative scaling of the observed shear. These systematic effects include: noisy galaxy images, the applicability of the model used to describe the light profile of galaxies, the details of the galaxy morphology and selection biases (Heymans et al., 2006; Mandelbaum et al., 2018; Zuntz et al., 2018). We parametrise this multiplicative scaling using one parameter m^i per redshift bin (10 parameters in total), which scale the cosmic shear and galaxy-galaxy lensing power spectra as:

$$\begin{aligned} C^{ij}_{\epsilon\epsilon}(l) &\rightarrow (1+m^i)(1+m^j)C^{ij}_{\epsilon\epsilon}(l)\ , \\ C^{ij}_{n\epsilon}(l) &\rightarrow (1+m^j)C^{ij}_{n\epsilon}(l)\ . \end{aligned} \tag{3.32}$$

We impose Gaussian priors on these multiplicative parameters, which are guided by the LSST DESC science requirements (Alonso et al., 2018). These science requirements forecast the uncertainties

LSST will need to achieve in order to meet their main objectives of significantly improving the constraints on the dark energy parameters w_0 and w_a, compared to previous dark energy experiments, and obtaining dark energy constraints where the total calibratable systematic uncertainty is less than the marginalised statistical uncertainty. For the case of shear multiplicative bias the requirement is that the systematic uncertainty should not exceed 0.003 by year 10. We therefore apply a Gaussian prior centred on zero with a standard deviation of 0.003 to our shear multiplicative bias parameters.

Clustering Multiplicative Bias

We parametrise uncertainties in the number count measurement using a similar approach to that for shear. Systematics which affect the number density of galaxies include: galactic dust obscuring background galaxies, variable survey depth impacting the number of sources promoted across the flux limit by magnification, and stars contaminating the galaxy sample (Hildebrandt, 2015; Thiele et al., 2019). Analogous to shear multiplicative bias, the observed clustering power spectra are scaled by a multiplicative factor as,

$$\begin{aligned} C^{ij}_{nn}(l) &\rightarrow (1+m^i_{\rm eff})(1+m^j_{\rm eff})C^{ij}_{nn}(l)\ , \\ C^{ij}_{n\epsilon}(l) &\rightarrow (1+m^i_{\rm eff})C^{ij}_{ne}(l)\ . \end{aligned} \tag{3.33}$$

However, since most systematics decrease with signal to noise ratio, we assume $m^i_{\rm eff}$ has a power law dependence on the signal to noise of galaxies in redshift bin i. This enables us to reduce the number of clustering multiplicative bias parameters from ten parameters (one $m^i_{\rm eff}$ per redshift bin) to two parameters α_m and β_m. $m^i_{\rm eff}$ is given in terms of α_m and β_m by,

$$\begin{aligned} m^i_{\rm eff} &= m_{\rm step} - m_{\rm fid} \\ &= \frac{1}{N_i}\left[\alpha_m \sum_{n=1}^{N_i}\left(\frac{S}{N}\right)^{\beta_m}_n - \alpha_{\rm fid}\sum_{n=1}^{N_i}\left(\frac{S}{N}\right)^{\beta_{\rm fid}}_n\right]\ , \end{aligned} \tag{3.34}$$

where N_i is the number of galaxies in tomographic bin i, the sum is over the signal-to-noise ratio S/N of all galaxies in tomographic bin i, $\alpha_{\rm fid}$ is the fiducial value of α_m and $\beta_{\rm fid}$ is the fiducial value of β_m. We introduce the $m_{\rm fid}$ term because if $m_{\rm eff} = m_{\rm step}$, β_m becomes unconstrained when α_m is equal to zero, which breaks the Gaussian Likelihood assumption in the Fisher matrix prediction.

We compute the signal to noise ratio for each galaxy in our samples from the error on the i band apparent magnitude (Hainaut, 2005). Using the signal to noise of every galaxy in this

bias calculation is computationally expensive, since the total number of galaxies in *n-sample* and ϵ-*sample* is of order 10^7 and 10^8. We therefore use a randomly selected 1% subsample of galaxies in this calculation. This subsample is representative of the full galaxy sample, but prevents our bias calculation from being prohibitively slow.

We only consider multiplicative biases because in Fourier space global additive biases disappear, and local additive biases can be calibrated directly on the data.

Photometric Redshift Uncertainties

We model uncertainties in the redshift distributions shown in Figures 3.3 and 3.4 by introducing shift factors Δ^i (Bonnett et al., 2016). Δ^i simply shifts the redshift distribution in bin i so,

$$n^i(z) \to n^i(z - \Delta^i). \tag{3.35}$$

Since we have two redshift distributions, one for ϵ-*sample* and one for *n-sample*, each divided into 10 bins this results in 20 shift parameters Δ^i. We impose Gaussian priors on these shift parameters, once again guided by the LSST DESC science requirements (Alonso et al., 2018). The prior is centred on zero, with a standard deviation of 0.003 for the *n-sample* parameters and of 0.001 for the ϵ-*sample* parameters .

3.5.5 Weak Lensing Observables Covariance

We compute a Gaussian covariance for the observable weak lensing power spectra ($C_{\epsilon\epsilon}$, C_{nn}, $C_{n\epsilon}$) using CosmoSIS. The covariance between two power spectra is given by,

$$\mathrm{Cov}\left[C^{ij}(\ell),\ C^{kl}(\ell')\right] = \delta_{\ell\ell'}\frac{2\pi}{A\ell\Delta\ell}\left[\bar{C}^{ik}(\ell)\bar{C}^{jl}(\ell) + \bar{C}^{il}(\ell)\bar{C}^{jk}(\ell)\right] , \tag{3.36}$$

where $ijkl$ denote redshift bins, A is the survey area and $\Delta\ell$ the size of the angular frequency ℓ bin (Joachimi and Bridle, 2010; Joachimi et al., 2008). The Kronecker delta $\delta_{\ell\ell'}$ shows that in the Gaussian case the covariance is diagonal. To account for the random terms in equations 3.7 and 3.8 we define,

$$\bar{C}^{ij}(\ell) = C^{ij}(\ell) + N^{ij} , \tag{3.37}$$

Table 3.2: Fiducial values and priors for the model parameters used to compute the fisher matrices in this work

Parameter	**Fiducial Value**	**Prior**
	Survey (section 3.5.5)	
Area	$18000\ \mathrm{deg}^2$	fixed
σ_e	0.35	fixed
	Cosmology (section 1.2.4)	
Ω_m	0.265	Flat
h_0	0.71	Flat
Ω_b	0.0448	Flat
n_s	0.963	Flat
$A_s/10^{-9}$	2.1	Flat
w	-1.0	Flat
w_a	0.0	Flat
Ω_k	0.0	fixed
	CLF (section 3.3.2)	
$\log(M_1)$	10.98	Flat
$\log(L_0)$	9.90	Flat
γ_1	3.00	Flat
γ_2	0.429	Flat
σ_c	0.047	Flat
α_s	-0.18	Flat
b_0	-0.63	Flat
b_1	1.50	Flat
b_2	-0.177	Flat
	Intrinsic Alignments (section 3.3.2)	
A_{IA}	1.0	Flat
	***n-sample* Photo-z** (section 3.5.4)	
Δ_n^i	0.0	Gauss(0.0, 0.003)
	ϵ***-sample* Photo-z** (section 3.5.4)	
Δ_ϵ^i	0.0	Gauss(0.0, 0.001)
	Shear Multiplicative Bias (section 3.5.4)	
m^i	0.0	Gauss(0.0, 0.003)
	Magnification Multiplicative Bias (section 3.5.4)	
α_m	0.001	Flat
β_m	0.0	Flat

where N^{ij} is the random noise contribution in the shape or number density measurement. In the case of $C_{\epsilon\epsilon}$,

$$N^{ij} = \delta_{ij} \frac{\sigma_e^2}{2\bar{n}^i} \; ; \tag{3.38}$$

in the case of C_{nn},

$$N^{ij} = \delta_{ij} \frac{1}{\bar{n}^i} \; ; \tag{3.39}$$

and in the case of $C_{n\epsilon}$, $N^{ij} = 0$. Here, σ_e^2 is the total intrinsic ellipticity dispersion, and $\bar{n}^i$ is the average number density of galaxies in redshift bin i. We compute the power spectra covariance for 20 log-spaced angular frequency ℓ bins from $\ell_{\rm min} = 30$, to avoid inaccuracies in the Limber approximation, to $\ell_{\rm max} = 3000$.

3.6 Fisher Matrix Stability

High-dimensional Fisher matrices can be unstable. Here we detail the steps taken to ensure the stability of our Fisher matrices and hence the robustness of our results.

The derivatives in eq. 3.3 are calculated numerically using a method of numerical differentiation called a 5-pt stencil (Sauer, 2012). This method requires the pipeline to be evaluated at 4 points around the model parameter's fiducial value (5 points including the fiducial value). The separation between these points is referred to as the step size. If the step size is too large the Fisher matrix fails to capture the curvature of the likelihood function about the peak and if it is too small numerical difficulties can arise. Therefore when using Fisher matrices it is vital to verify whether the step size is appropriate, otherwise any results are meaningless.

We verify our step sizes in one dimension by fixing all but one model parameter. We then calculate the 1D likelihood using a Fisher matrix with a specified step size and by sampling the likelihood function directly. If the 1D likelihoods match we know we are using a reasonable step size when calculating our Fisher matrix. We sample the likelihood function directly using a simulated datavector generated at the Fisher matrix fiducial values and a grid sampler. Grid samplers evaluate the likelihood at a specified set of grid points. Since we are assuming a Gaussian Likelihood when calculating our Fisher matrix (eq.3.3) we are only interested in whether the standard deviation σ of the likelihood calculated using the Fisher matrix matches the σ of the likelihood from sampling

directly using a grid sampler.

Figure 3.8 shows the σ of the 1D likelihood calculated using the Fisher matrix for different choices of step size. These plots show that as the step size decreases the σ of the 1D likelihood reaches a plateau, where the step size is actually capturing the shape of the likelihood, before becoming unstable (see subplot for magnification bias parameter α_m). We therefore select a step size in the range where the σ of the Fisher likelihood is stable. Figure 3.9 shows the Fisher likelihoods generated using the selected step sizes overlaid with the likelihood from the grid sampler to verify that they match. For the case of the magnification bias parameter β_m the Fisher and grid likelihoods do not match. This is because when calculating the Fisher matrix we assume that the likelihood is Gaussian, and the likelihood of β_m from direct sampling is clearly not Gaussian. This is a limitation of the Fisher matrix approach, and we keep this in mind when making statements about the β_m parameter.

The 1D grid likelihoods in Figure 3.9 also show some numerical instabilities in the cosmological parameters. We suspect that this is due to the 1D grid likelihoods challenging the numerical accuracy of the pipeline, since fixing all but one parameter is not a realistic scenario and results in incredibly tight constraints on a single parameter. We therefore additionally check the Fisher step sizes for the cosmological parameters, by varying all the cosmological parameters at once and exploring the multivariate posterior with Markov Chain Monte Carlo (MCMC) sampling[3]. Figure 3.10 shows a comparison between the constraints obtained from the MCMC and the Fisher matrix. They match well and show that our Fisher matrix is adequately capturing the shape of the likelihood.

Figures 3.8 and 3.9 show only an example case for the parameters used to generate the C_{nn} Fisher matrix for *ϵ-sample*. However, the step sizes have been verified using this method for every Fisher matrix referred to in the results section.

3.7 Results

In this section we present the effect of including magnification on the precision of an LSST like angular galaxy clustering ($C_{\rm nn}$) and a quasi '3x2pt' ($C_{\rm nn}$, $C_{\rm n\epsilon}$, $C_{\epsilon\epsilon}$) analysis. We cannot conduct a full '3x2pt' analysis as the halo model we employ to calculate the 3D power spectra does not currently have the capability to calculate $P_{\rm g\delta}$ and $P_{\rm gI}$ when the g, and the δI components come from different galaxy samples. This means we cannot currently compute $C_{\rm n\epsilon}$. Instead we assume that the $C_{\rm nn}$ and $C_{\epsilon\epsilon}$ analyses occur on separate patches of sky, so there are no correlations between

[3]the MCMC we use is emcee (Foreman-Mackey et al., 2013)

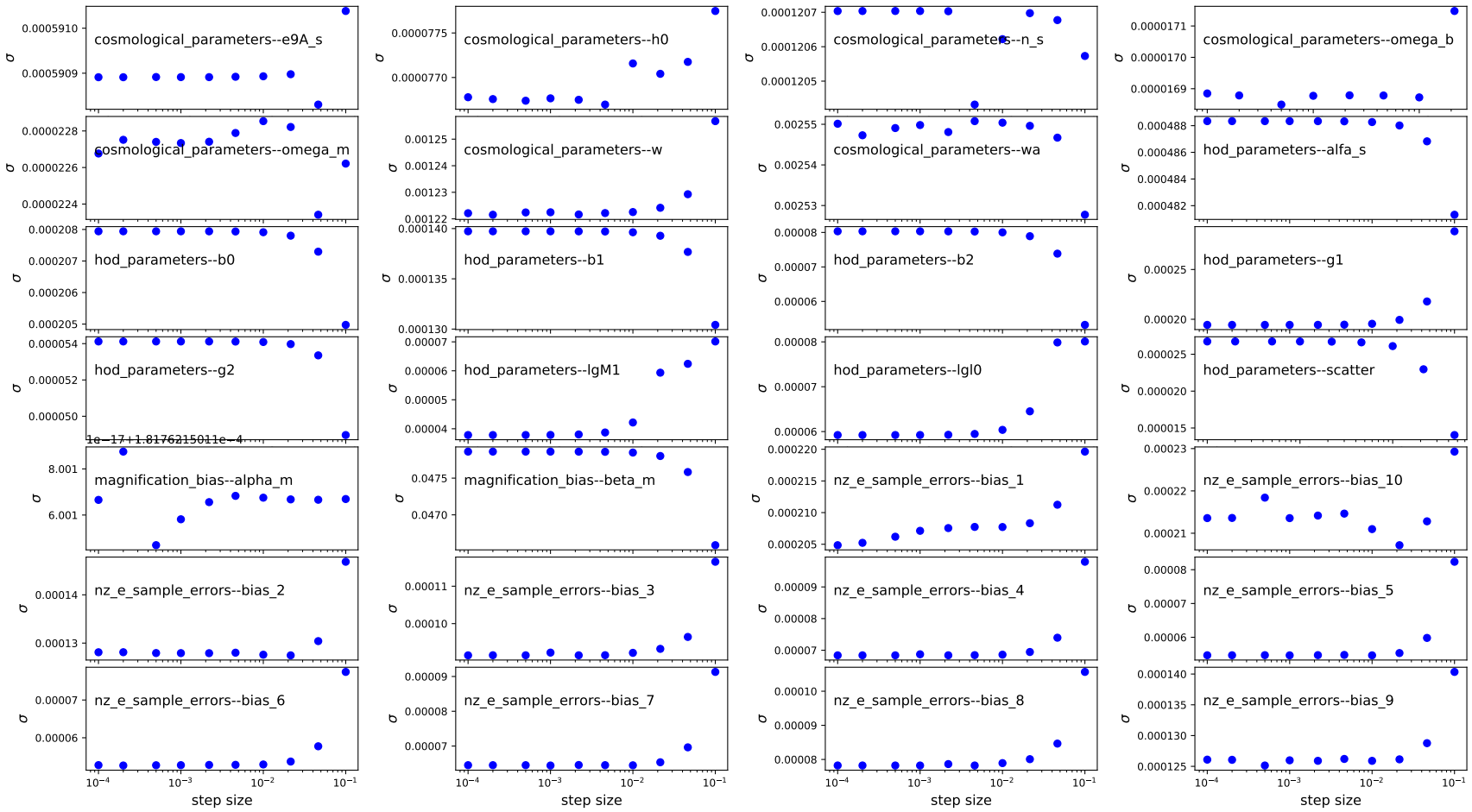

Figure 3.8: Standard deviation of the 1D Fisher likelihoods against the step size used to calculate the derivatives in the Fisher matrix. The chosen step size should be in the plateau region, where the standard deviation changes little with step size, and the Fisher matrix is actually capturing the shape of the likelihood.

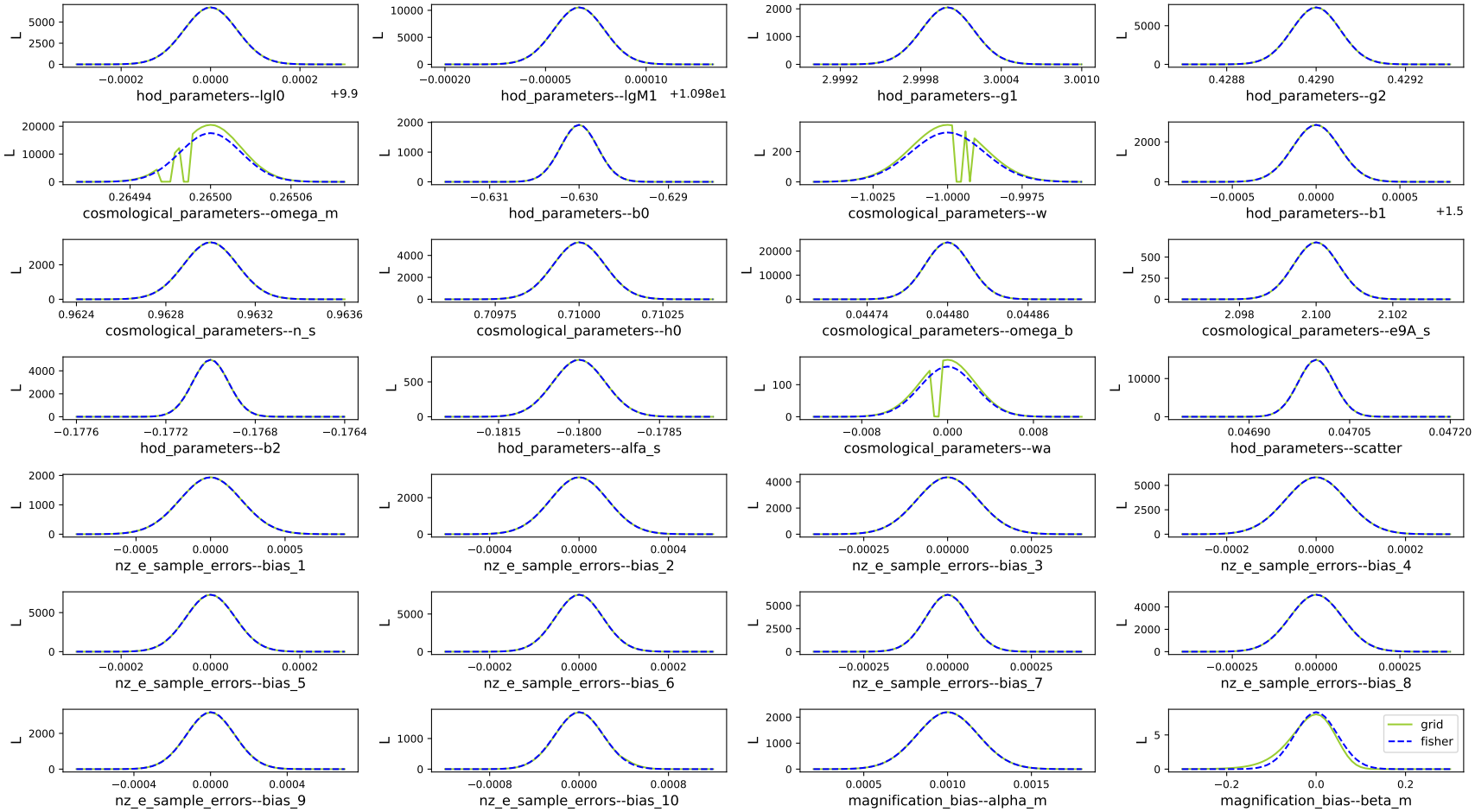

Figure 3.9: Comparison of the 1D likelihoods from the Fisher matrix calculated using the selected step size against the 1D likelihoods from sampling the likelihood directly using a grid sampler.

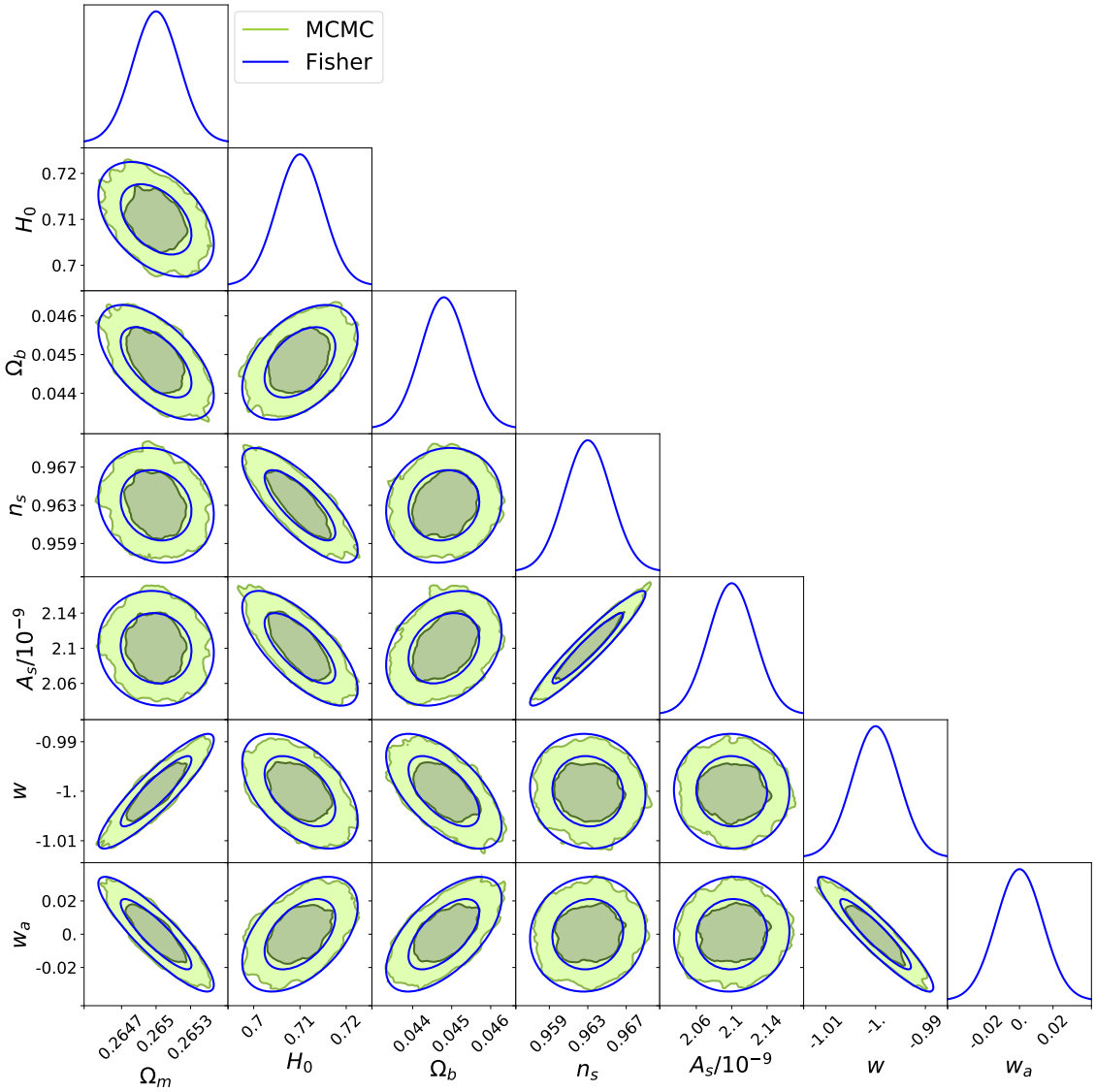

Figure 3.10: Comparison of the constraints on the cosmological parameters used in this analysis when found using an MCMC or a Fisher matrix. All other parameters have been fixed.

them (no $C_{\mathrm{n}\epsilon}$ term). We are therefore able to use two separate implementations of the halo model, and avoid the need for implementing two different samples at once.

3.7.1 Clustering

Figure 3.11 shows the forecast constraints on the cosmological parameters from C_{nn} with and without including magnification terms for *n-sample*. In the case of including magnification the observable is $C_{nn} = C_{gg} + C_{gm} + C_{mm}$ instead of $C_{nn} = C_{gg}$. Including magnification significantly improves the constraints on all of the cosmological parameters. In particular the 1σ constraint on $A_s/10^{-9}$ is improved by 73% from 0.04 without magnification to 0.01 with magnification. This is because by including magnification terms we are incorporating weak lensing information into the clustering measurement, and weak lensing is particularly sensitive to σ_8 (see introduction) which is the late-time version of A_s. The 1σ constraints on n_s and H_0 are also both improved by 61% from 0.004 to 0.002 and from 0.010 to 0.004 respectively. Weak lensing does not have particular sensitivity to these parameters, but they are highly degenerate with the measurement of A_s, see Fig, 3.11. Therefore the large increase in precision of the $A_s/10^{-9}$ constraints from including magnification is likely driving the increase in precision for n_s and H_0.

Figure 3.12 shows the forecast constraints on the CLF parameters from C_{nn} with and without including magnification terms for *n-sample*. Including magnification only slightly improves the constraints on the CLF parameters, because the CLF constraints are predominantly determined by the galaxy luminosity function, which does not change when including magnification. We focus on the cosmological and CLF parameters, instead of presenting the full 28 parameter space, for clarity.

Figure 3.13 shows the forecast constraints on the cosmological parameters from C_{nn} and C_{nn} including magnification terms for ϵ*-sample*. Including magnification improves the constraints similarly to the deeper *n-sample* case (Fig. 3.11), but the improvement is less pronounced. The greatest improvement in the constraints is still for $A_s/10^{-9}$, but the improvement is 55% from 0.05 to 0.02, instead of 73% with the deeper *n-sample*. This shows that including magnification has a greater impact for deeper samples as expected, since the total magnification is greater. Once again, for ϵ*-sample* including magnification only slightly improves the CLF parameters.

A useful measure of the constraining power of an analysis is the Figure of Merit (FoM) defined as,

$$\mathrm{FoM} = \det([\mathrm{F}^{-1}]_{\mathrm{q}})^{\frac{1}{\mathrm{N_q}}} \ , \tag{3.40}$$

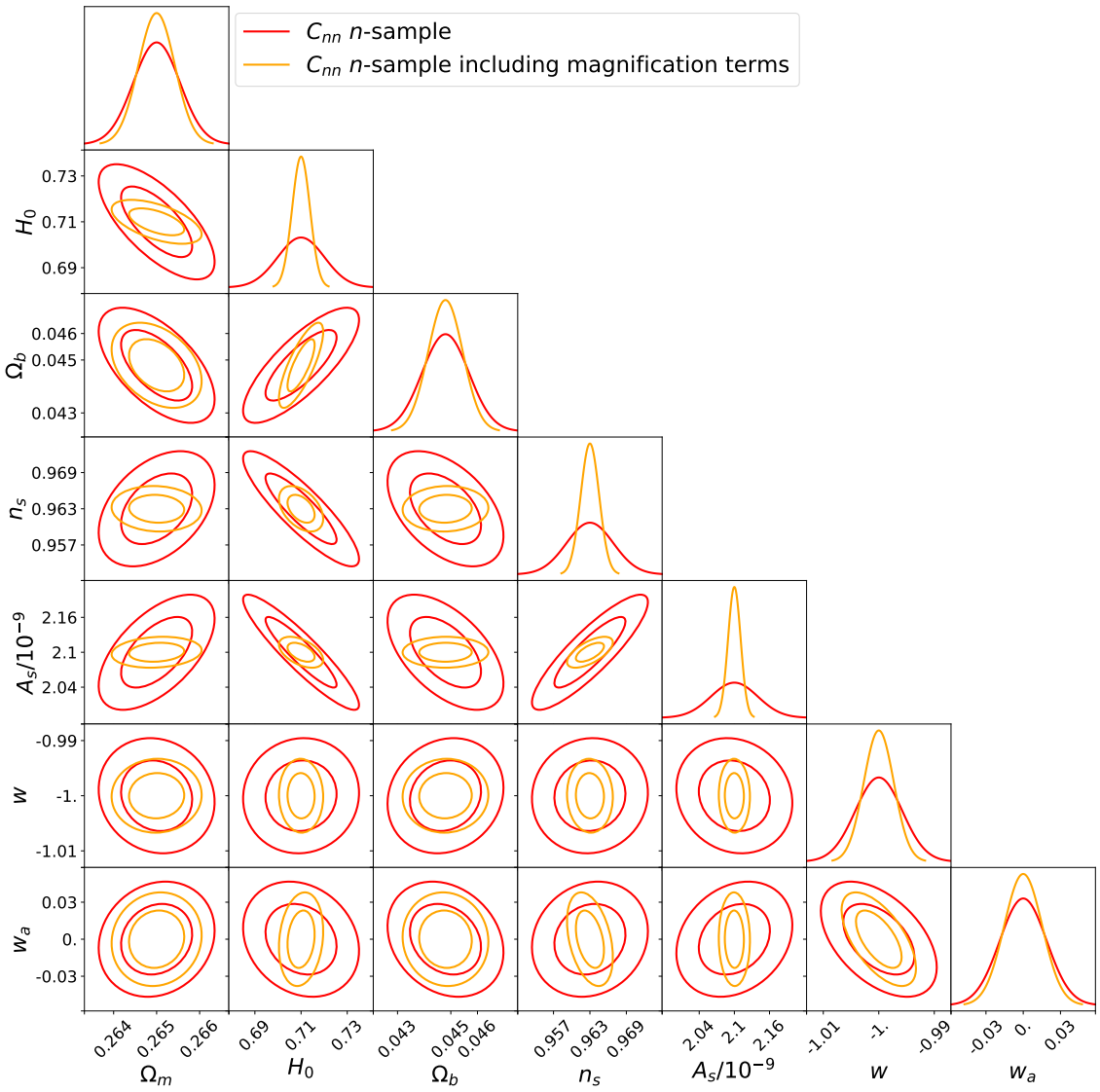

Figure 3.11: Constraints on the cosmological parameters used in this analysis from C_{nn} and C_{nn} including magnification terms for *n-sample*. Including magnification improves all of the constraints.

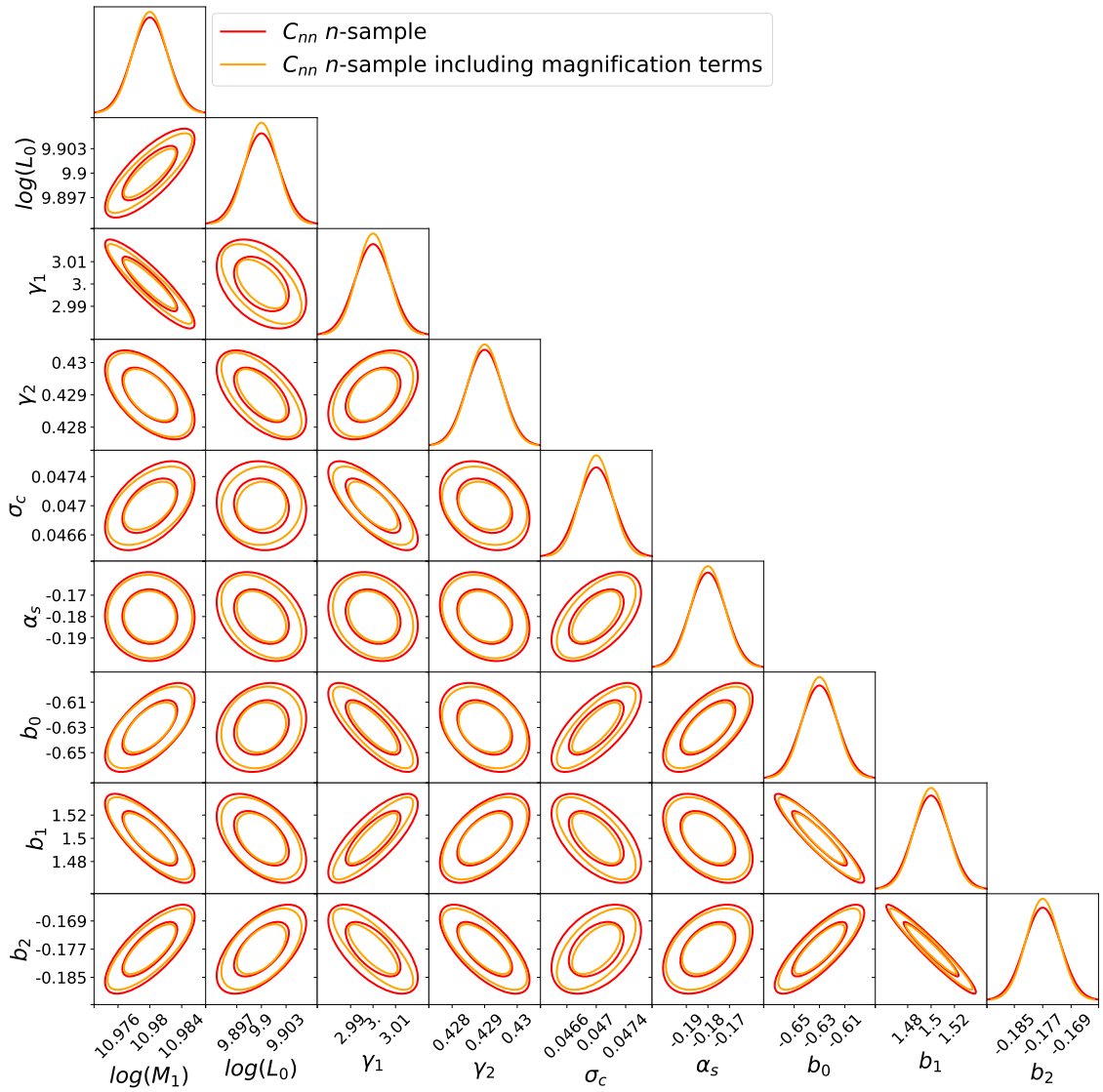

Figure 3.12: Constraints on the Conditional Luminosity Function (CLF) parameters used in this analysis from C_{nn} and C_{nn} including magnification terms for *n-sample*. Including magnification has little effect on the constraints, since they are determined by the galaxy luminosity function not the weak lensing or clustering observables.

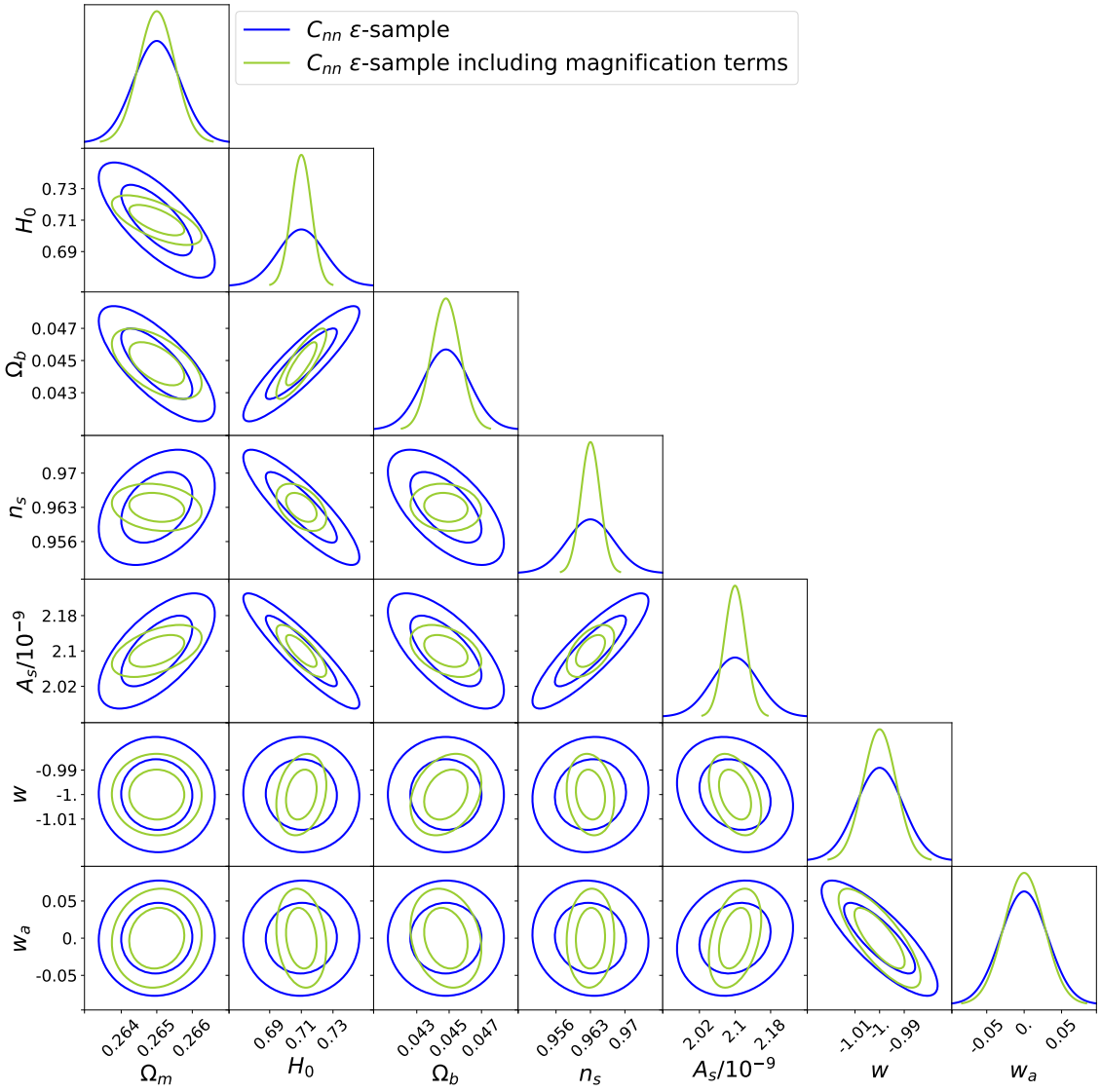

Figure 3.13: Constraints on the cosmological parameters used in this analysis from C_{nn} and C_{nn} including magnification terms for ϵ-*sample*. Including magnification improves all of the constraints, although not as significantly as for the deeper *n-sample*.

Table 3.3: Relative increase in the Figure of Merit (FoM) for the full set of cosmological parameters when deviating from the base analysis. The base analysis is taken to be C_{nn} not including magnification terms for the LSST gold sample *ϵ-sample*.

change from $C_{\rm nn}$ *ϵ-sample* base case	**relative increase in FoM**
n-sample	1.42
include magnification	1.69
n-sample and include magnification	4.13

where $[F^{-1}]_q$ is the inverse Fisher matrix for the set of parameters q and N_q is the number of parameters q in the set. In this work we define q as the full set of cosmological parameters, so the FoM represents the power of the constraints on the cosmological parameters. It is also common to define a Dark Energy FoM where $q = \{w, w_a\}$ (Albrecht et al., 2006).

Table 3.3 shows the relative increase in the FoM for the cosmological parameters, when the analysis is adjusted from the base case. We take the base case to be the clustering analysis for *ϵ-sample* (the LSST gold sample) not including the impacts of weak lensing magnification. When only the deeper *n-sample* is used the FoM is increased by a factor of 1.42, and when only the magnification terms are included the FoM is increased by a factor of 1.69. This means that when deviating from the base analysis it is more beneficial to include magnification terms than to use a deeper sample. However, if we include both the deeper *n-sample* and the magnification terms the FoM is increased by a factor of 4.13. This shows that including magnification becomes even more beneficial for deeper samples with greater numbers of low signal-to-noise galaxies.

3.7.2 Clustering + Shear

Cosmological Parameters

Figure 3.14 shows the forecast constraints on the cosmological parameters from our quasi '3x2pt' analysis of $C_{\rm nn}$ and $C_{\epsilon\epsilon}$ with and without magnification terms, where $C_{\epsilon\epsilon}$ is calculated for *ϵ-sample* and $C_{\rm nn}$ for the deeper *n-sample*. Including magnification the observables are $C_{\rm nn} = C_{\rm gg} + C_{\rm gm} + C_{\rm mm}$ and $C_{\epsilon\epsilon} = C_{\rm GG} + C_{\rm IG} + C_{\rm II}$, and in the case of not including magnification $C_{\rm nn} = C_{\rm gg}$. Including magnification improves the constraints on the cosmological parameters even when including the contribution from $C_{\epsilon\epsilon}$. The greatest improvement is in the 1σ constraint on $A_s/10^{-9}$, where there is a 60% increase in precision from 0.02 to 0.01 when including magnification. This mirrors the $C_{\rm nn}$ only case, except the improvement in the $A_s/10^{-9}$ constraint is reduced because the magnification terms provide similar information to $C_{\epsilon\epsilon}$. There is also a 47% improvement in the

Table 3.4: Relative increase in the Figure of Merit (FoM) for the full set of cosmological parameters when deviating from the base analysis. The base analysis is taken to be $C_{\epsilon\epsilon}$ and $C_{\rm nn}$ not including magnification terms for the LSST gold sample ϵ-*sample*.

change from $C_{\epsilon\epsilon}$ ϵ-*sample* and $C_{\rm nn}$ ϵ-*sample* base case	**relative increase in FoM**
n-sample	1.36
include magnification	1.30
n-sample and include magnification	2.60

H_0 constraint from 0.007 to 0.004, which as mentioned in the clustering section is likely due to the degeneracy between H_0 and $A_s/10^{-9}$ shown in Fig. 3.14. This degeneracy is worth investigating further as it implies an LSST '3x2pt' analysis could provide a competitive constraint on H_0, an active area of debate in current cosmology.

Figure 3.15 shows the forecast constraints on the cosmological parameters from our quasi '3x2pt' analysis, with and without magnification terms for ϵ-*sample*. Similarly to the $C_{\rm nn}$ only case, the impact of magnification is reduced when using the shallower ϵ-*sample*. In this case the improvement in the 1σ constraint on $A_s/10^{-9}$ is 32% from 0.03 to 0.02.

As above, Table 3.4 shows the relative increase in the FoM for the cosmological parameters, when the analysis is adjusted from the base case. We take the base case to be the shear and clustering analysis for ϵ-*sample* (the LSST gold sample), not including the impacts of weak lensing magnification. Compared to the clustering only case the gains from including magnification are reduced due to magnification providing similar information to $C_{\epsilon\epsilon}$. For the clustering only case including magnification terms was more beneficial than using the deeper *n-sample*, which is not true when including shear. When using only the deeper *n-sample* for $C_{\rm nn}$ the FoM is increased by a factor of 1.36, and when only the magnification terms are included the FoM is increased by a factor of 1.30. The factor increase in the FoM from including magnification and the deeper *n-sample* is 2.60, which is approximately half that for the clustering only case. When using shear information, including magnification is not as beneficial.

Shear Calibration

When obtaining the cosmological constraints in figures 3.15 and 3.14 we place a tight Gaussian prior on the shear multiplicative bias parameters (see Table 3.2). However, if we remove this prior we can examine the impact of magnification on the shear multiplicative bias parameters.

Figure 3.16 shows the forecast constraints on the shear multiplicative bias parameters from our

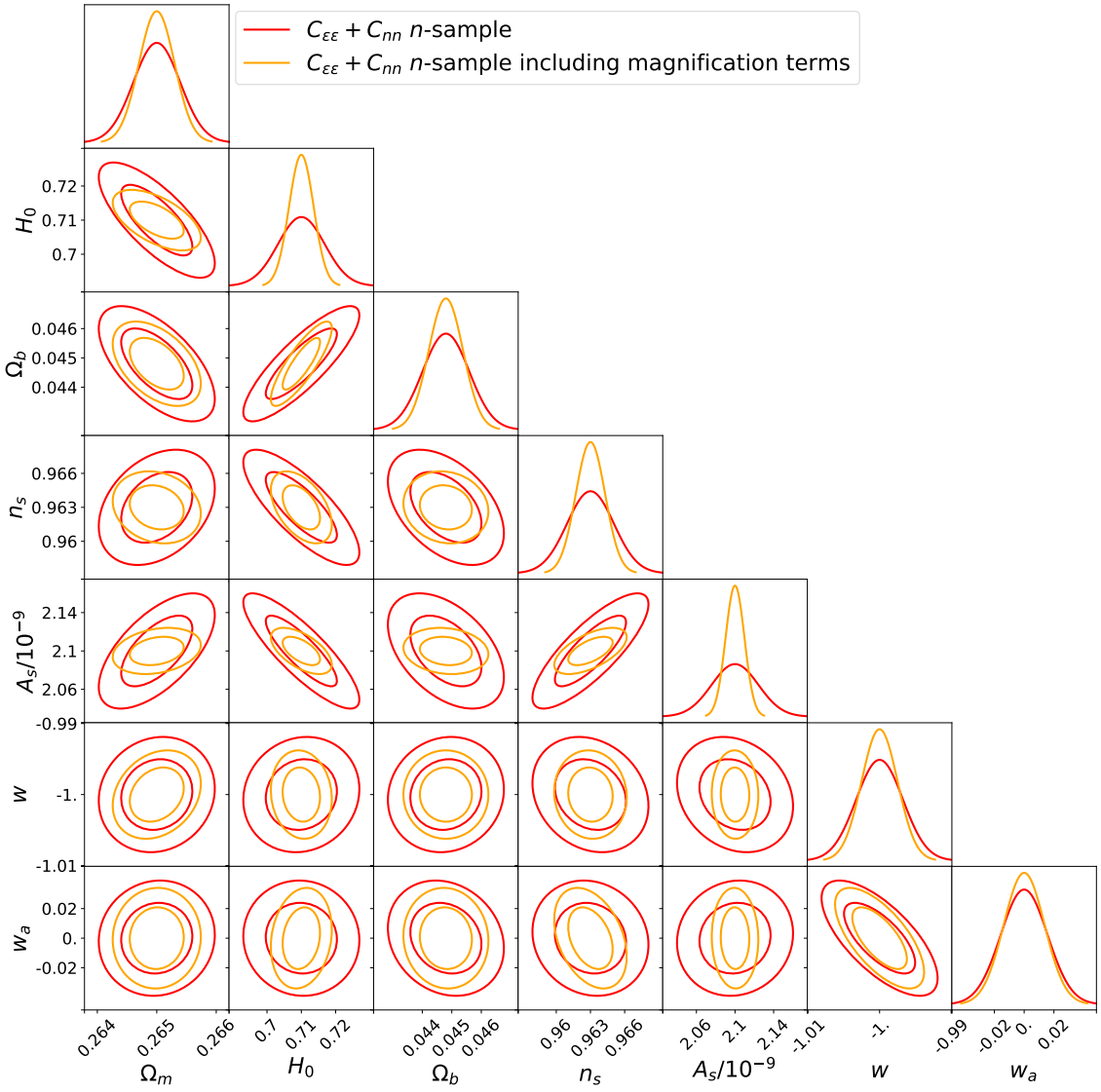

Figure 3.14: Constraints on the cosmological parameters used in this analysis from a joint analysis of $C_{\epsilon\epsilon}$ and $C_{\rm nn}$ with and without magnification terms. $C_{\epsilon\epsilon}$ is calculated for ϵ-*sample* and $C_{\rm nn}$ is calculated for *n-sample*. Including magnification improves the constraints.

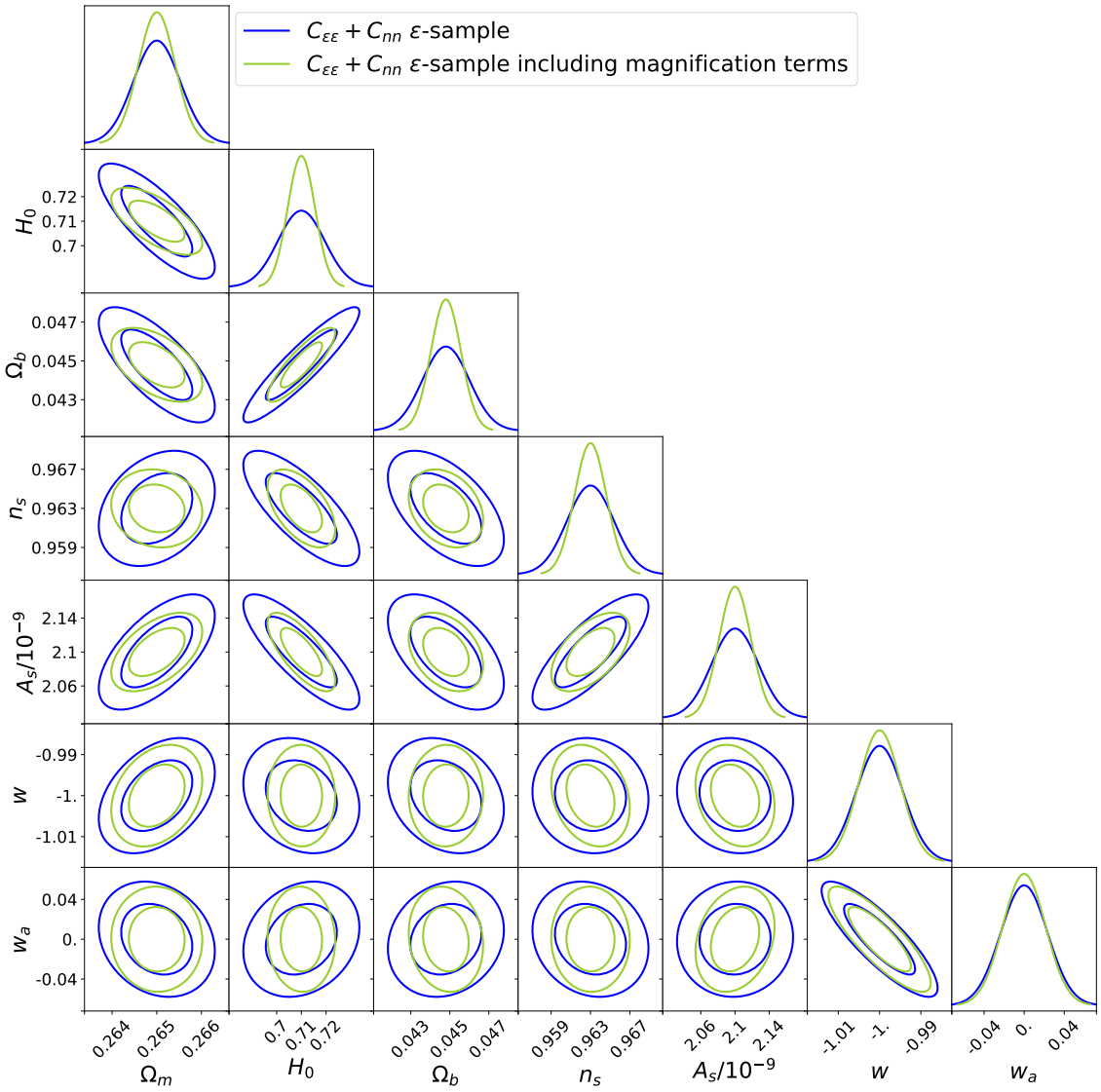

Figure 3.15: Constraints on the cosmological parameters used in this analysis from a joint analysis of $C_{\epsilon\epsilon}$ and $C_{\rm nn}$ with and without magnification terms. $C_{\epsilon\epsilon}$ and $C_{\rm nn}$ are both calculated for *ϵ-sample*. Including magnification improves the constraints to a lesser extent than when $C_{\rm nn}$ is calculated for *n-sample*.

$C_{\rm nn}$ and $C_{\epsilon\epsilon}$ analysis, with and without magnification terms, where $C_{\epsilon\epsilon}$ is calculated for *ϵ-sample* and $C_{\rm nn}$ for the deeper *n-sample*. Including magnification improves the constraints on the shear calibration parameters, particularly for those at higher redshift. For m^1 there is almost no increase in precision from including magnification, whereas for m^6 there is a 40% increase in precision and for m^{10} there is a 50% increase in precision. The effect of including magnification is similar when $C_{\rm nn}$ is calculated using the shallower *ϵ-sample*, but less pronouced. For m^1 there is almost no increase in precision from including magnification, whereas for m^6 and m^{10} there is a 20% increase in precision.

This result means that including magnification helps to calibrate internally the shear measurement. Usually shear measurments are calibrated using simulations (Kannawadi et al., 2019; Mandelbaum et al., 2018), so including magnification could be a useful validation. Additionally, as mentioned in section 3.5.4, the LSST DESC requirement is that the uncertainty on the multiplicative shear calibration should not exceed 0.003 by year 10. We find that when $C_{\rm nn}$ is calculated for the deeper *n-sample*, the constraints on the shear calibration parameters reach a precision of 0.003 when including magnification for $m^6 - m^{10}$. Magnification is therefore a highly competitive validation as it reaches the LSST requirement independently of external calibration.

Clustering Calibration

Figures 3.17 and 3.18 show the FoM for the set of cosmological parameters as a function of the width of the prior on the multiplicative clustering bias parameters. The clustering bias parameters are α_m and β_m, where α_m is the amplitude of the bias and β_m is the signal-to-noise dependence (see section 3.5.4). There are two key conclusions to be drawn from these plots. First, that including magnification always improves the FoM even if there is a lot of uncertainty in the clustering calibration. Second, that if the 1σ uncertainty on α_m can be reduced to approximately 10^{-3} there is an increase in the FoM, Fig. 3.17 shows a higher plateau below 10^{-3}. When $C_{\rm nn}$ is calculated for the deeper *n-sample* the increase is 9% and when $C_{\rm nn}$ is calculated for *ϵ-sample* there is a 7% increase. Similarly, if the 1σ uncertainty on β_m can be reduced to approximately 10^{-1} there is an increase in the FoM of 4% for *n-sample* and 3% for *ϵ-sample*. If we use the Dark Energy FoM where $q = \{w, w_a\}$, we find similar increases in the FoM at 10^{-3} for α_m and 10^{-1} for β_m. These values could therefore be considered as targets for the future calibration of LSST clustering measurements.

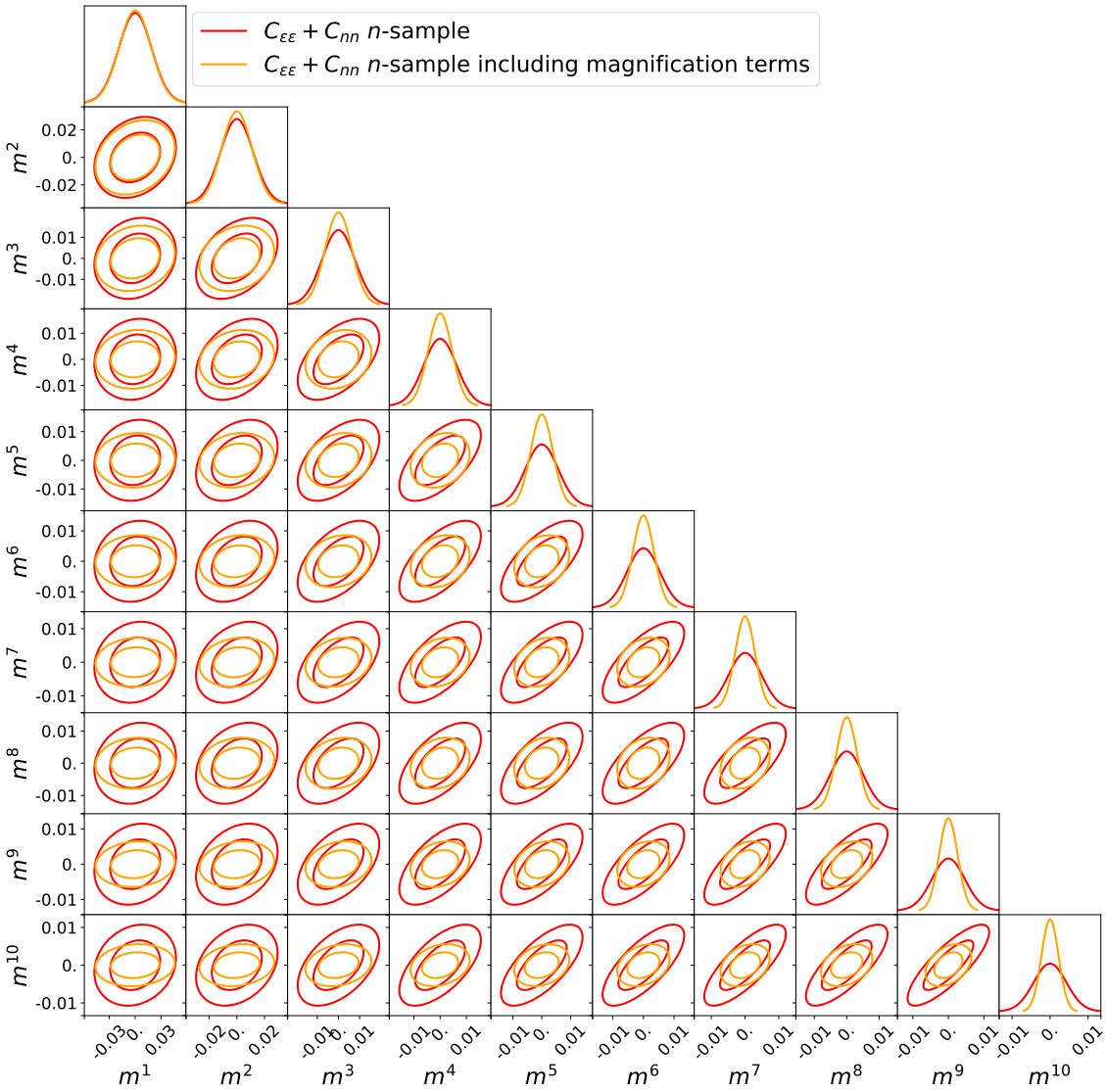

Figure 3.16: Constraints on the shear multiplicative bias parameters from a joint analysis of $C_{\epsilon\epsilon}$ and $C_{\rm nn}$ with and without magnification terms, where we have not applied the Gaussian prior detailed in Table 3.2. $C_{\epsilon\epsilon}$ is calculated for ϵ-*sample* and $C_{\rm nn}$ is calculated for *n-sample*. Including magnification improves the constraints, particularly for those at higher redshift.

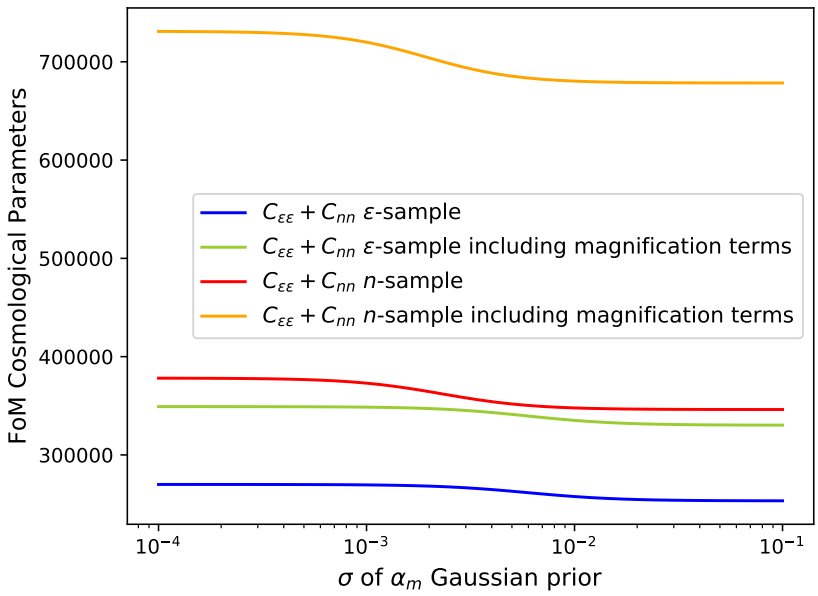

Figure 3.17: Figure of Merit (FoM) for the set of cosmological parameters used in this analysis as a function of the prior on the clustering multiplicative bias amplitude α_m. Including magnification always improves the FoM. If α_m can be calibrated to a precision of 10^{-3} there are gains in the FoM.

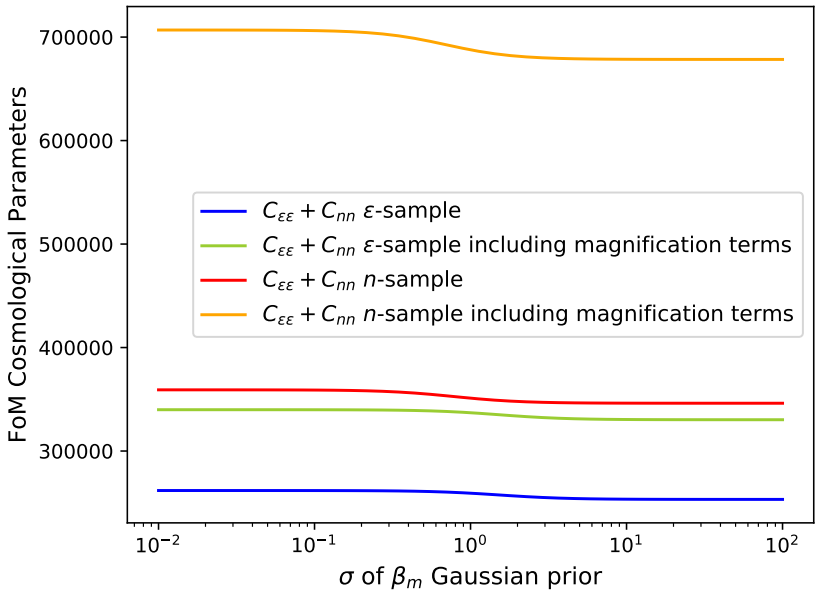

Figure 3.18: Figure of Merit (FoM) for the set of cosmological parameters used in this analysis as a function of the prior on the clustering multiplicative bias signal-to-noise dependence β_m. Including magnification always improves the FoM. If β_m can be calibrated to a precision of 10^{-1} there are gains in the FoM.

3.7.3 Bias

Recent works have shown that cosmological results from upcoming surveys such as LSST will be biased if the effects of weak lensing magnification are not included, due to improvements in statistical precision (Cardona et al., 2016; Duncan et al., 2014; Lorenz et al., 2018; Thiele et al., 2019). To examine this for our forecast, figure 3.19 shows the absolute difference between the clustering power spectra $C_{\rm nn}$ with and without magnification in terms of the 1σ uncertainty on the clustering power spectra without magnification. In this case the clustering power spectra have been calculated using *n-sample*. The grey shaded region indicates where $C_{\rm nn}$ including magnification is more than 2σ away from $C_{\rm nn}$ without magnification. Particularly at high ℓ (small scales) $C_{\rm nn}$ including magnification significantly diverges from $C_{\rm nn}$ without magnification.

For comparison, we have also shown the impact of changing Ω_m and A_s by 5σ in Fig. 3.19. In almost all of the redshift bin combinations shown the difference from including magnification is larger than the difference from changing Ω_m and A_s by 5σ. This clearly indicates that not including magnification terms will catastrophically bias cosmological constraints from LSST. Additionally, the difference from not including magnification seems to mimic the behaviour of biasing A_s by 5σ. This implies that not including magnification could particularly bias the constraints for A_s, one of the parameters weak lensing is most sensitive to.

Figure 3.20 shows the absolute difference between the clustering power spectra $C_{\rm nn}$ with and without magnification in terms of the 1σ uncertainty on the clustering power spectra without magnification, where the clustering power spectra have been calculated using the shallower ϵ-*sample*. In this case the difference from including magnification is not as large as for *n-sample*, however in most redshift bin combinations is still comparable or larger than the differences from changing Ω_m and A_s by 5σ.

3.8 Conclusions

Previous works have shown that upcoming results from surveys such as LSST and *Euclid* will be biased if the effects of weak lensing magnification are not included (Cardona et al., 2016; Duncan et al., 2014; Lorenz et al., 2018; Thiele et al., 2019). In this work we forecast whether including weak lensing magnification as a complementary probe can additionally improve the precision of the LSST weak lensing constraints. We determined this using the Fisher matrix formalism, where our theory datavector included the weak lensing observables and the galaxy luminosity function. To

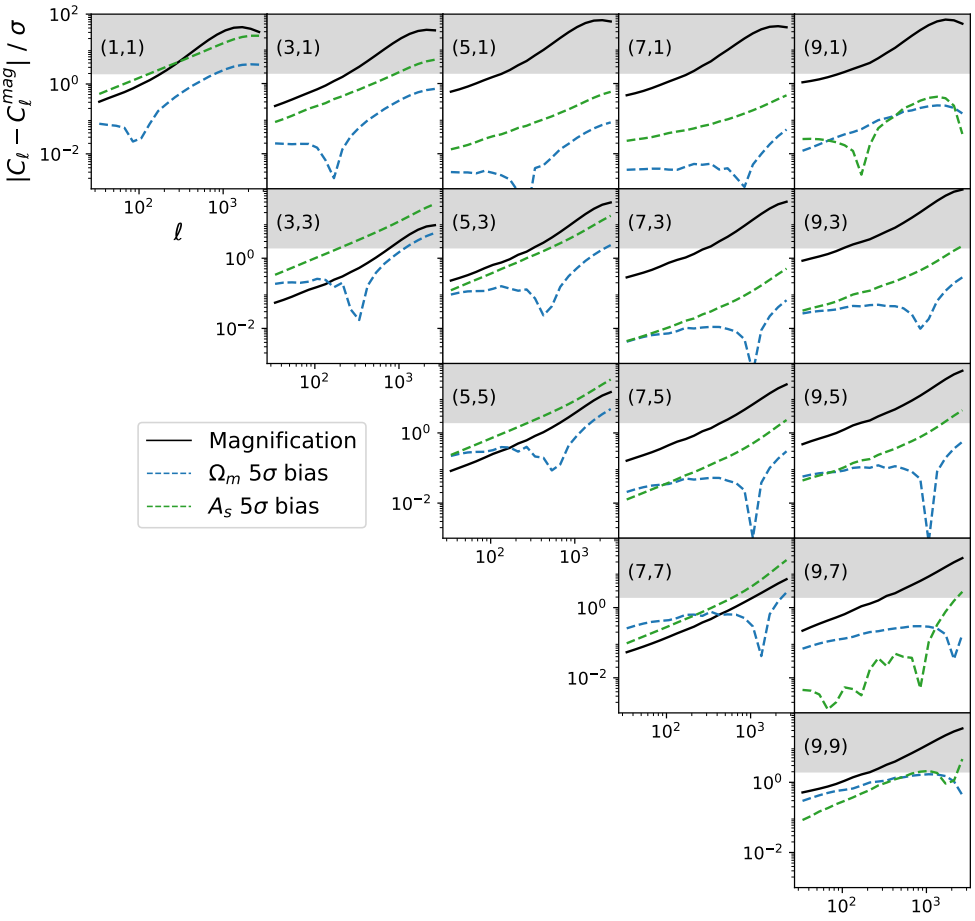

Figure 3.19: Absolute difference between $C_{\rm nn}$ with and without magnification, in terms of the uncertainty σ on $C_{\rm nn}$ with magnification, for *n-sample*. The grey shaded region indicates where $C_{\rm nn}$ including magnification is more than 2σ away from $C_{\rm nn}$ without magnification. The dashed lines show the difference in $C_{\rm nn}$ when Ω_m and A_s are altered by 5σ. The redshift bin combination is labelled in the top left corner of each panel by (i, j). We show only alternate bin combinations to condense the figure.

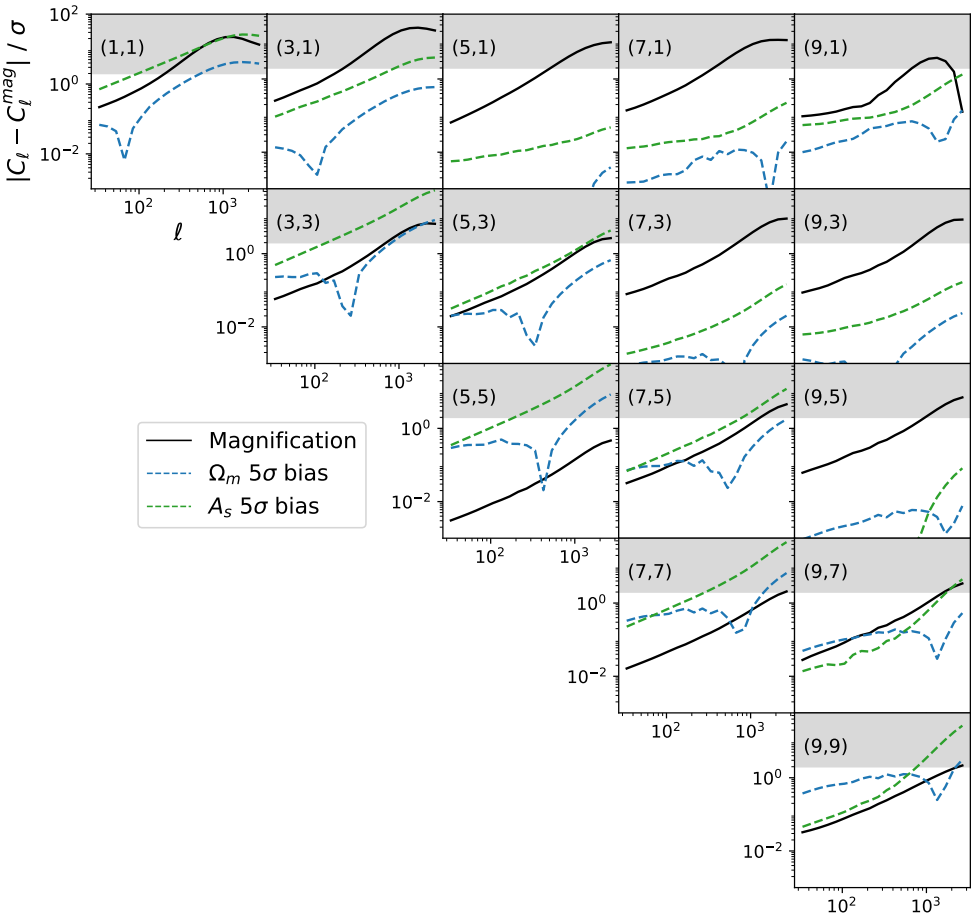

Figure 3.20: Absolute difference between $C_{\rm nn}$ with and without magnification, in terms of the uncertainty σ on $C_{\rm nn}$ with magnification, for ϵ-*sample*. The grey shaded region indicates where $C_{\rm nn}$ including magnification is more than 2σ away from $C_{\rm nn}$ without magnification. The dashed lines show the difference in $C_{\rm nn}$ when Ω_m and A_s are altered by 5σ. The redshift bin combination is labelled in the top left corner of each panel by (i, j). We show only alternate bin combinations to condense the figure.

calculate the weak lensing observables and the galaxy luminosity function, we employed a halo model, detailed in Fortuna et al. (2020). We defined two mock LSST galaxy samples from the LSST DC2 simulations (Korytov et al., 2019) for use in our forecast; a sample which corresponds to the LSST gold sample where the i band magnitude is less than 25.3 (intended to be used for the weak lensing shear measurement), and a deeper sample where the i band magnitude is less than 26.5.

We found that weak lensing magnification provides additional information as a complementary probe for LSST. For a galaxy clustering only analysis using the LSST gold sample we found that including magnification increased the Figure of Merit (FoM) for the set of cosmological parameters Ω_m, h_0, Ω_b, n_s, $A_s/10^{-9}$, w and w_a by a factor of 1.69. However, when using the deeper galaxy sample we found that magnification increased the FoM by a factor of 4.13. For a galaxy clustering and cosmic shear analysis (without galaxy-galaxy lensing) using the LSST gold sample we found that including magnification increased the FoM by a factor of 1.3. When using the deeper galaxy sample for the clustering part of the analysis we found that including magnification increased the FoM by a factor of 2.6. The effect of including magnification is reduced in the combined galaxy clustering and cosmic shear analysis because magnification provides similar information to that of cosmic shear. In both analyses including magnification is more beneficial for deeper samples.

We also found that including weak lensing magnification has a significant impact on the precision of the A_s constraints. For a galaxy clustering only analysis using the LSST gold sample we found that including magnification increased the precision of the A_s constraints by 55%, using the deeper sample we found an increase of 73%. For a galaxy clustering and cosmic shear analysis using the LSST gold sample we found that including magnification increased the precision of the A_s constraints by 32%, and when using the deeper sample for the clustering part of the analysis we found that the precision increased by 60%. Even for the LSST gold sample, which will form the core analysis, including magnification has a significant impact on the A_s constraints.

Aside from its impact on the cosmological parameter constraints we found that including weak lensing magnification in a galaxy clustering and cosmic shear analysis can help to internally calibrate the shear measurement. The increases in precision from including magnification may be optimistic for our joint galaxy clustering and cosmic shear analysis, as we assume that the cosmic shear analysis occurs on an independent part of the sky. In reality magnification will partially or fully measure the same volume as cosmic shear, which will reduce the statistical gains, but would likely improve magnification's ability to calibrate the shear measurement. There is no choice but to model the cosmology dependence of magnification in an LSST analysis to avoid bias, and this work shows that there are additional benefits to including magnification.

While this forecast is more realistic than many to date, as it includes LSST mock catalog data and a flexible galaxy bias model, it still relies on a number of simplified assumptions about magnification. Firstly, the magnification modelling assumes that the galaxy sample is purely flux limited. Often galaxies are also selected based on their signal-to-noise ratio, colours and morphology which complicates the magnification modelling (Hildebrandt, 2015). Secondly, there are a large number of systematics associated with the magnification measurement such as dust attenuation, variable survey depth, star-galaxy separation and the blending of galaxy images (Hildebrandt et al., 2013; Morrison and Hildebrandt, 2015; Thiele et al., 2019). We included a multiplicative factor in our modelling of the clustering power spectra in order to incorporate these effects, and found that magnification always improves the FoM, independent of the uncertainty in the clustering calibration. However, more detailed modelling of these effects may alter this conclusion. Our results also showed that there are much greater benefits to including magnification when using a galaxy sample deeper than the the LSST gold sample. Using a deeper galaxy sample is therefore very desirable, but the impact of systematic effects would likely be increased due to the greater numbers of low signal-to-noise galaxies.

4 Conclusion

This thesis is focussed on the precision of upcoming large-scale structure surveys. In chapter 2 we set a target precision for future large-scale structure measurements to determine the neutrino hierarchy, when combined with neutrino oscillation measurements. In chapter 3 we forecast whether including weak lensing magnification in future large-scale structure analyses, such as for LSST or *Euclid*, can improve the precision of the final cosmological constraints.

In chapter 2, we set a target precision for future large-scale structure measurements by formulating a prior, for a joint analysis of neutrino data from oscillation experiments and from cosmology, which is agnostic to the neutrino hierarchy. The neutrino hierarchy refers to the ordering of the neutrino masses, and is a key question in neutrino physics. Neutrino oscillation experiments provide information about the mass differences between the individual neutrinos, whereas cosmological experiments provide an overall mass scale in the form of the sum of neutrino masses. They are therefore highly complementary probes, and a joint analysis of the neutrino hierarchy is desirable. However, selecting a suitable prior for this joint analysis is challenging and can have a large impact on the final results. A number of works have found very different odds in favour of the neutrino hierarchy largely due to their choice of prior, see chapter 2 for details. We therefore constructed a prior, which was agnostic to the hierarchy by design, and determined that current data is not powerful enough to determine the neutrino hierarchy. Since the limiting factor in this joint analysis is the cosmological neutrino mass sum measurements, we then set a target precision for future cosmological data to determine the neutrino hierarchy.

A future direction for this work is to determine whether our target precision is achievable. With the DESI telescope currently taking data, it is likely that there will be a cosmological measurement of the neutrino mass sum in the next 5 years; currently the measurements are only upper limits (Aghamousa et al., 2016; Font-Ribera et al., 2014). But reaching the precision required to determine

the neutrino hierarchy is a more challenging task. Current forecasts suggest that a combination of CMB data from *Planck*, with large-scale structure data from *Euclid*, LSST or DESI can reach a 1σ precision of approximately 0.02 eV (Copeland et al., 2020; Font-Ribera et al., 2014; Laureijs et al., 2011; Mishra-Sharma et al., 2018). However, in order to reach our target 1σ precision of 0.014 eV, an improved measurement of the optical depth to reionisation τ is likely required (see introduction) (Brinckmann et al., 2019; Mishra-Sharma et al., 2018). Currently, the LiteBIRD satellite is the only funded experiment, which could improve upon the *Planck* measurement of τ, and it is expected to be launched in the mid-late 2020s (Hazumi et al., 2019).

One of the major goals of upcoming neutrino oscillation experiments, such as DUNE and JUNO is to determine the neutrino hierachy (Acciarri et al., 2015; An et al., 2016). This is an independent measurement, which focusses on how neutrinos and anti-neutrinos propagate differently through matter, and is becoming possible due to the long propagation distances involved in these experiments (Acciarri et al., 2015). DUNE is planned to begin taking data in 2026 and JUNO in 2021, so it is likely there will be a determination of the neutrino hierarchy from oscillation experiments in the late 2020s. However, an additional determination of the hierarchy from combining the neutrino mass splittings and neutrino mass sum from cosmological data would be a stunning confirmation of both the cosmological and the standard model, given the hugely different physics involved. Another interesting avenue for future neutrino physics is the improved measurements of the neutrino mass from beta decay and neutrino-less double beta decay experiments (see introduction). If these lab-based searches find a result consistent with future cosmological results, the cosmological model will gain a significant boost.

In chapter 3 we investigate whether including weak lensing magnification in future weak lensing analyses can increase the precision of the final constraints on the cosmological parameters. Weak lensing is a technique which uses the minute distortions to galaxy images caused by gravitational light deflection to map the matter distribution in the Universe. Usually weak lensing focuses on distortions to the observed shape of galaxies, but weak lensing magnification utilises distortions to the apparent size of galaxies. Statistical measurements of the shape distortions are called cosmic shear, and weak lensing magnification can be measured statistically through its contribution to galaxy clustering (see chapter 3). Weak lensing magnification has not been included in standard weak lensing analyses to date, but recent works have shown that it must be included in future analyses, such as for LSST and *Euclid*, to avoid biasing the results (Cardona et al., 2016; Duncan et al., 2014; Lorenz et al., 2018; Thiele et al., 2019). We therefore forecast whether including weak lensing magnification in an LSST analysis could additionally improve the precision of the final

cosmological constraints.

We found that including weak lensing magnification improves the precision of the final LSST constraints for both a galaxy clustering only analysis and a joint galaxy clustering and cosmic shear analysis, and that the impact of magnification is greater for deeper galaxy samples. In particular we found that for a joint LSST galaxy clustering and cosmic shear analysis the constraint on A_s, a parameter weak lensing is particularly sensitive to, would be improved by 32% when using the base LSST galaxy sample for the galaxy clustering analysis, and by 60% when using a sample which is approximately one magnitude deeper. In addition to weak lensing magnification improving the precision of the cosmological constraints, we found that it could help to calibrate internally the cosmic shear measurement. This work therefore shows that there are benefits to including weak lensing magnification in an LSST analysis, beyond avoiding bias.

A future direction for this work is to examine how best to include weak lensing magnification in upcoming weak lensing analyses. Current magnification modelling is quite simplified and in order to include magnification in a future weak lensing analysis the effects of various systematics on the magnification measurement would need to be modelled (see chapter 3 for further details). Thiele et al. (2019) also showed that the effects of magnification cannot simply be removed by making cuts to the datavector used in the analysis. Also, our work shows that including magnification has a much greater impact on the final constraints when using a deeper galaxy sample. A deeper galaxy sample would likely be more susceptible to systematic effects, given the greater numbers of low signal-to-noise galaxies, so accurate modelling is even more important.

Another way weak lensing magnification could bias future photometric surveys is through its impact on photometric redshift calibration. Photometric redshift estimation is a major source of uncertainty for current and upcoming large-scale photometric surveys, and may be the source of the current tension between weak lensing surveys, such as DES (Troxel et al., 2018) and KiDS (Hildebrandt et al., 2020), with *Planck* (Aghanim et al., 2018) (see introduction). One option for controlling photometric redshift uncertainties is to use the clustering of galaxies in a spectroscopic sample (where the redshifts are well known), to calibrate the photometric sample (Busch et al., 2020; Matthews and Newman, 2010). However, since magnification biases clustering measurements it can complicate the calibration. The impact of weak lensing magnification on the calibration therefore needs to be quantified. Additionally, since photometric redshift uncertainties will contribute significantly to the total uncertainty of results from upcoming surveys, accurately calibrating the photometric redshifts will be vital in reaching our target precision to determine the neutrino mass hierarchy.

Our target precision has been cited by several other studies focussed on how to learn about neutrinos from cosmology, and our finding that including weak lensing magnification can improve the precision of the final cosmological constraints provides a positive case for its inclusion in future weak lensing analyses. This thesis work has therefore made a useful contribution to the era of precision cosmology.

Bibliography

M. Aartsen et al. Measurement of Atmospheric Neutrino Oscillations at 6–56 GeV with IceCube DeepCore. *Phys. Rev. Lett.*, 120(7):071801, 2018.

K. Abazajian et al. Neutrino Physics from the Cosmic Microwave Background and Large Scale Structure. *Astropart. Phys.*, 63:66–80, 2015.

T. Abbott et al. Dark Energy Survey Year 1 Results: Constraints on Extended Cosmological Models from Galaxy Clustering and Weak Lensing. *Phys. Rev. D*, 99(12):123505, 2019.

T. M. C. Abbott et al. Dark Energy Survey year 1 results: Cosmological constraints from galaxy clustering and weak lensing. *Phys. Rev.*, D98(4):043526, 2018.

K. Abe et al. Observation of Electron Neutrino Appearance in a Muon Neutrino Beam. *Phys. Rev. Lett.*, 112:061802, 2014. doi: 10.1103/PhysRevLett.112.061802.

K. Abe et al. Measurement of neutrino and antineutrino oscillations by the T2K experiment including a new additional sample of ν_e interactions at the far detector. *Phys. Rev. D*, 96(9):092006, 2017. [Erratum: Phys.Rev.D 98, 019902 (2018)].

K. Abe et al. Atmospheric neutrino oscillation analysis with external constraints in Super-Kamiokande I-IV. *Phys. Rev. D*, 97(7):072001, 2018a.

K. Abe et al. Search for CP Violation in Neutrino and Antineutrino Oscillations by the T2K Experiment with 2.2×10^{21} Protons on Target. *Phys. Rev. Lett.*, 121(17):171802, 2018b.

K. Abe et al. Constraint on the matter–antimatter symmetry-violating phase in neutrino oscillations. *Nature*, 580(7803):339–344, 2020.

R. Acciarri et al. Long-Baseline Neutrino Facility (LBNF) and Deep Underground Neutrino Experiment (DUNE): Conceptual Design Report, Volume 2: The Physics Program for DUNE at LBNF. *arXiv:1512.06148*, 12 2015.

M. Acero et al. New constraints on oscillation parameters from ν_e appearance and ν_μ disappearance in the NOvA experiment. *Phys. Rev. D*, 98:032012, 2018.

M. Acero et al. First Measurement of Neutrino Oscillation Parameters using Neutrinos and Antineutrinos by NOvA. *Phys. Rev. Lett.*, 123(15):151803, 2019.

P. Adamson et al. Combined analysis of ν_μ disappearance and $\nu_\mu \to \nu_e$ appearance in MINOS using accelerator and atmospheric neutrinos. *Phys. Rev. Lett.*, 112:191801, 2014.

P. Ade et al. Planck 2013 results. XVI. Cosmological parameters. *Astron. Astrophys.*, 571:A16, 2014.

P. Ade et al. The Simons Observatory: Science goals and forecasts. *JCAP*, 02:056, 2019.

D. Adey et al. Measurement of the Electron Antineutrino Oscillation with 1958 Days of Operation at Daya Bay. *Phys. Rev. Lett.*, 121(24):241805, 2018.

A. Aghamousa et al. The DESI Experiment Part I: Science,Targeting, and Survey Design. *arXiv:1611.00036*, 10 2016.

N. Aghanim et al. Planck 2018 results. VI. Cosmological parameters. *arXiv:1807.06209*, 7 2018.

M. Agostini, G. Benato, and J. Detwiler. Discovery probability of next-generation neutrinoless double- β decay experiments. *Phys. Rev. D*, 96(5):053001, 2017.

Q. Ahmad et al. Measurement of the rate of $\nu_e + d \rightarrow p + p + e^-$ interactions produced by ^8B solar neutrinos at the Sudbury Neutrino Observatory. *Phys. Rev. Lett.*, 87:071301, 2001.

S. Aiola et al. The Atacama Cosmology Telescope: DR4 Maps and Cosmological Parameters. *arXiv:2007.07288*, 7 2020.

M. Aker et al. Improved Upper Limit on the Neutrino Mass from a Direct Kinematic Method by KATRIN. *Phys. Rev. Lett.*, 123(22):221802, 2019.

Y. Akrami et al. Planck 2018 results. I. Overview and the cosmological legacy of Planck. *arXiv:1807.06205*, 7 2018.

A. Albrecht et al. Report of the Dark Energy Task Force. *arXiv:astro-ph/0609591*, 9 2006.

R. Allison, P. Caucal, E. Calabrese, J. Dunkley, and T. Louis. Towards a cosmological neutrino mass detection. *Phys. Rev. D*, 92(12):123535, 2015.

D. Alonso et al. The LSST Dark Energy Science Collaboration (DESC) Science Requirements Document. *arXiv:1809.01669*, 2018.

F. An et al. Observation of electron-antineutrino disappearance at Daya Bay. *Phys. Rev. Lett.*, 108: 171803, 2012. doi: 10.1103/PhysRevLett.108.171803.

F. An et al. Neutrino Physics with JUNO. *J. Phys. G*, 43(3):030401, 2016.

L. Anderson et al. The clustering of galaxies in the SDSS-III Baryon Oscillation Spectroscopic Survey: baryon acoustic oscillations in the Data Releases 10 and 11 Galaxy samples. *Mon. Not. Roy. Astron. Soc.*, 441(1):24–62, 2014.

E. Aprile et al. Observation of Excess Electronic Recoil Events in XENON1T. *arXiv:2006.09721*, 6 2020.

F. T. Avignone, S. R. Elliott, and J. Engel. Double beta decay, majorana neutrinos, and neutrino mass. *Rev. Mod. Phys.*, 80:481–516, Apr 2008. URL `https://link.aps.org/doi/10.1103/RevModPhys.80.481`.

C. Babusiaux et al. The Detailed Science Case for the Maunakea Spectroscopic Explorer, 2019 edition. *arXiv:1904.04907*, 4 2019.

G. Bak et al. Measurement of Reactor Antineutrino Oscillation Amplitude and Frequency at RENO. *Phys. Rev. Lett.*, 121(20):201801, 2018.

M. Bartelmann. Gravitational Lensing. *Class. Quant. Grav.*, 27:233001, 2010.

M. Bartelmann and M. Maturi. Weak gravitational lensing. *arXiv:1612.06535*, 12 2016.

M. Bartelmann and P. Schneider. Weak gravitational lensing. *Phys. Rept.*, 340:291–472, 2001.

J. F. Beacom and N. F. Bell. Do Solar Neutrinos Decay? *Phys. Rev. D*, 65:113009, 2002.

N. Benitez. Bayesian photometric redshift estimation. *Astrophys. J.*, 536:571–583, 2000.

C. L. Bennett, D. Larson, J. L. Weiland, N. Jarosik, G. Hinshaw, N. Odegard, K. M. Smith, R. S. Hill, B. Gold, M. Halpern, E. Komatsu, M. R. Nolta, L. Page, D. N. Spergel, E. Wollack, J. Dunkley, A. Kogut, M. Limon, S. S. Meyer, G. S. Tucker, and E. L. Wright. Nine-year Wilkinson Microwave Anisotropy Probe (WMAP) Observations: Final Maps and Results. ApJS, 208(2):20, Oct. 2013.

M. Betti et al. Neutrino physics with the PTOLEMY project: active neutrino properties and the light sterile case. *JCAP*, 07:047, 2019.

C. Bonnett et al. Redshift distributions of galaxies in the Dark Energy Survey Science Verification shear catalogue and implications for weak lensing. *Phys. Rev. D*, 94(4):042005, 2016.

S. Bridle and L. King. Dark energy constraints from cosmic shear power spectra: impact of intrinsic alignments on photometric redshift requirements. *New J. Phys.*, 9:444, 2007.

T. Brinckmann, D. C. Hooper, M. Archidiacono, J. Lesgourgues, and T. Sprenger. The promising future of a robust cosmological neutrino mass measurement. *JCAP*, 01:059, 2019.

J. v. d. Busch, H. Hildebrandt, A. Wright, C. Morrison, C. Blake, B. Joachimi, T. Erben, C. Heymans, and K. Kuijken. Testing KiDS cross-correlation redshifts with simulations. *arXiv:2007.01846*, 7 2020.

M. Cacciato, F. C. van den Bosch, S. More, H. Mo, and X. Yang. Cosmological constraints from a combination of galaxy clustering and lensing - III. Application to SDSS data. MNRAS, 430(2): 767–786, Apr 2013.

A. Caldwell, A. Merle, O. Schulz, and M. Totzauer. Global Bayesian analysis of neutrino mass data. *Phys. Rev. D*, 96(7):073001, 2017.

W. Cardona, R. Durrer, M. Kunz, and F. Montanari. Lensing convergence and the neutrino mass scale in galaxy redshift surveys. *Phys. Rev.*, D94(4):043007, 2016.

D. Clowe, M. Bradac, A. H. Gonzalez, M. Markevitch, S. W. Randall, C. Jones, and D. Zaritsky. A direct empirical proof of the existence of dark matter. *Astrophys. J. Lett.*, 648:L109–L113, 2006.

D. Coe. Fisher Matrices and Confidence Ellipses: A Quick-Start Guide and Software. *arXiv:0906.4123*, 6 2009.

S. Cole. Maximum likelihood random galaxy catalogues and luminosity function estimation. MNRAS, 416(1):739–746, Sept. 2011.

M. Colless, G. Dalton, S. Maddox, W. Sutherland , P. Norberg, S. Cole, J. Bland -Hawthorn, T. Bridges, R. Cannon, C. Collins, W. Couch, N. Cross, K. Deeley, R. De Propris, S. P. Driver, G. Efstathiou, R. S. Ellis, C. S. Frenk, K. Glazebrook, C. Jackson, O. Lahav, I. Lewis, S. Lumsden, D. Madgwick, J. A. Peacock, B. A. Peterson, I. Price, M. Seaborne, and K. Taylor. The 2dF Galaxy Redshift Survey: spectra and redshifts. MNRAS, 328(4):1039–1063, Dec. 2001.

D. Copeland, A. Taylor, and A. Hall. Towards determining the neutrino mass hierarchy: weak lensing and galaxy clustering forecasts with baryons and intrinsic alignments. *Mon. Not. Roy. Astron. Soc.*, 493(2):1640–1661, 2020.

C. Cowan, F. Reines, F. Harrison, H. Kruse, and A. McGuire. Detection of the free neutrino: A Confirmation. *Science*, 124:103–104, 1956.

G. Danby, J. Gaillard, K. A. Goulianos, L. Lederman, N. B. Mistry, M. Schwartz, and J. Steinberger. Observation of High-Energy Neutrino Reactions and the Existence of Two Kinds of Neutrinos. *Phys. Rev. Lett.*, 9:36–44, 1962.

J. Davis, Raymond, D. S. Harmer, and K. C. Hoffman. Search for neutrinos from the sun. *Phys. Rev. Lett.*, 20:1205–1209, 1968.

P. De Salas, S. Gariazzo, O. Mena, C. Ternes, and M. Trtola. Neutrino Mass Ordering from Oscillations and Beyond: 2018 Status and Future Prospects. *Front. Astron. Space Sci.*, 5:36, 2018.

P. F. de Salas and S. Pastor. Relic neutrino decoupling with flavour oscillations revisited. *JCAP*, 07: 051, 2016.

S. Dodelson. *Modern cosmology*. Academic Press, 2003.

C. Duncan, B. Joachimi, A. Heavens, C. Heymans, and H. Hildebrandt. On the complementarity of galaxy clustering with cosmic shear and flux magnification. *Mon. Not. Roy. Astron. Soc.*, 437(3): 2471–2487, 2014.

B. Efron. *The jackknife, the bootstrap, and other resampling plans*. Siam, 1982.

J. Errard, S. M. Feeney, H. V. Peiris, and A. H. Jaffe. Robust forecasts on fundamental physics from the foreground-obscured, gravitationally-lensed CMB polarization. *JCAP*, 03:052, 2016.

I. Esteban, M. Gonzalez-Garcia, M. Maltoni, T. Schwetz, and A. Zhou. The fate of hints: updated global analysis of three-flavor neutrino oscillations. *JHEP*, 09:178, 2020. doi: 10.1007/JHEP09(2020)178.

J. E. Felten. On Schmidt's V ?m estimator and other estimators of luminosity functions. ApJ, 207: 700–709, Aug. 1976.

A. Font-Ribera, P. McDonald, N. Mostek, B. A. Reid, H.-J. Seo, and A. Slosar. DESI and other dark energy experiments in the era of neutrino mass measurements. *JCAP*, 05:023, 2014.

D. Foreman-Mackey, D. W. Hogg, D. Lang, and J. Goodman. emcee: The MCMC Hammer. PASP, 125(925):306, Mar. 2013.

M. C. Fortuna, H. Hoekstra, B. Joachimi, H. Johnston, N. E. Chisari, C. Georgiou, and C. Mahony. The halo model as a versatile tool to predict intrinsic alignments. *arXiv:2003.02700*, 2020.

J. K. Freudenburg, E. M. Huff, and C. M. Hirata. A Framework for Measuring Weak-Lensing Magnification Using the Fundamental Plane. *arXiv:1910.02906*, 10 2019.

Y. Fukuda et al. Evidence for oscillation of atmospheric neutrinos. *Phys. Rev. Lett.*, 81:1562–1567, 1998.

A. Gando et al. Reactor On-Off Antineutrino Measurement with KamLAND. *Phys. Rev. D*, 88(3): 033001, 2013.

A. Gando et al. Search for Majorana Neutrinos near the Inverted Mass Hierarchy Region with KamLAND-Zen. *Phys. Rev. Lett.*, 117(8):082503, 2016. [Addendum: Phys.Rev.Lett. 117, 109903 (2016)].

S. Gariazzo, M. Archidiacono, P. de Salas, O. Mena, C. Ternes, and M. Trtola. Neutrino masses and their ordering: Global Data, Priors and Models. *JCAP*, 03:011, 2018.

E. George et al. A measurement of secondary cosmic microwave background anisotropies from the 2500-square-degree SPT-SZ survey. *Astrophys. J.*, 799(2):177, 2015.

M. Gerbino. Neutrino properties from cosmology. *arXiv:1803.11545*, pages 52–52, 3 2018.

M. Gerbino, M. Lattanzi, O. Mena, and K. Freese. A novel approach to quantifying the sensitivity of current and future cosmological datasets to the neutrino mass ordering through Bayesian hierarchical modeling. *Phys. Lett. B*, 775:239–250, 2017.

O. Hainaut. Signal, Noise and Detection. https://www.eso.org/~ohainaut/ccd/sn.html, 2005. Accessed: 7-06-19.

S. Hannestad and T. Schwetz. Cosmology and the neutrino mass ordering. *JCAP*, 11:035, 2016.

M. Hazumi et al. LiteBIRD: A Satellite for the Studies of B-Mode Polarization and Inflation from Cosmic Background Radiation Detection. *J. Low Temp. Phys.*, 194(5-6):443–452, 2019.

A. F. Heavens and E. Sellentin. Objective Bayesian analysis of neutrino masses and hierarchy. *JCAP*, 04:047, 2018.

J. Hewett et al. Fundamental Physics at the Intensity Frontier. *arXiv:1205.2671*, 5 2012.

C. Heymans, L. Van Waerbeke, D. Bacon, J. Berge, G. Bernstein, E. Bertin, S. Bridle, M. L. Brown, D. Clowe, H. Dahle, T. Erben, M. Gray, M. Hetterscheidt, H. Hoekstra, P. Hudelot, M. Jarvis, K. Kuijken, V. Margoniner, R. Massey, Y. Mellier, R. Nakajima, A. Refregier, J. Rhodes, T. Schrabback, and D. Wittman. The Shear Testing Programme I. Weak lensing analysis of simulated ground-based observations. *Monthly Notices of the Royal Astronomical Society*, 368(3):1323–1339, 04 2006. ISSN 0035-8711. URL https://doi.org/10.1111/j.1365-2966.2006.10198.x.

C. Heymans et al. CFHTLenS tomographic weak lensing cosmological parameter constraints: Mitigating the impact of intrinsic galaxy alignments. *Mon. Not. Roy. Astron. Soc.*, 432:2433, 2013.

C. Hikage et al. Cosmology from cosmic shear power spectra with Subaru Hyper Suprime-Cam first-year data. *Publ. Astron. Soc. Jap.*, 71(2):Publications of the Astronomical Society of Japan, Volume 71, Issue 2, April 2019, 43, https://doi.org/10.1093/pasj/psz010, 2019.

H. Hildebrandt. Observational biases in flux magnification measurements. *Monthly Notices of the Royal Astronomical Society*, 455(4):3943–3951, 12 2015. ISSN 0035-8711. URL https://doi.org/10.1093/mnras/stv2575.

H. Hildebrandt, L. van Waerbeke, D. Scott, M. Béthermin, J. Bock, D. Clements, A. Conley, A. Cooray, J. S. Dunlop, S. Eales, T. Erben, D. Farrah, A. Franceschini, J. Glenn, M. Halpern, S. Heinis, R. J. Ivison, G. Marsden, S. J. Oliver, M. J. Page, I. Pérez-Fournon, A. J. Smith, M. Rowan-Robinson, I. Valtchanov, R. F. J. van der Burg, J. D. Vieira, M. Viero, and L. Wang. Inferring the mass of submillimetre galaxies by exploiting their gravitational magnification of background galaxies. MNRAS, 429(4):3230–3237, Mar. 2013.

H. Hildebrandt et al. KiDS+VIKING-450: Cosmic shear tomography with optical and infrared data. *Astron. Astrophys.*, 633:A69, 2020.

C. M. Hirata and U. Seljak. Intrinsic alignment-lensing interference as a contaminant of cosmic shear. Phys. Rev. D, 70(6):063526, Sept. 2004.

K. Hirata et al. Experimental Study of the Atmospheric Neutrino Flux. pages 235–246, 3 1988.

C. Howlett, A. Lewis, A. Hall, and A. Challinor. CMB power spectrum parameter degeneracies in the era of precision cosmology. J. Cosmology Astropart. Phys., 2012(4):027, Apr 2012.

W. Hu and S. Dodelson. Cosmic Microwave Background Anisotropies. *Ann. Rev. Astron. Astrophys.*, 40:171–216, 2002.

E. Hubble. A relation between distance and radial velocity among extra-galactic nebulae. *Proceedings of the National Academy of Sciences*, 15(3):168–173, 1929. ISSN 0027-8424. URL https://www.pnas.org/content/15/3/168.

E. M. Huff and G. J. Graves. MAGNIFICENT MAGNIFICATION: EXPLOITING THE OTHER HALF OF THE LENSING SIGNAL. *The Astrophysical Journal*, 780(2):L16, dec 2013. URL https://doi.org/10.1088%2F2041-8205%2F780%2F2%2Fl16.

R. Jimenez, T. Kitching, C. Pena-Garay, and L. Verde. Can we measure the neutrino mass hierarchy in the sky? *JCAP*, 05:035, 2010.

B. Joachimi and S. L. Bridle. Simultaneous measurement of cosmology and intrinsic alignments using joint cosmic shear and galaxy number density correlations. *A&A*, 523:A1, 2010. URL `https://doi.org/10.1051/0004-6361/200913657`.

B. Joachimi, P. Schneider, and T. Eifler. Analysis of two-point statistics of cosmic shear. 3. Covariances of shear measures made easy. *Astron. Astrophys.*, 477:43, 2008.

B. Joachimi et al. Galaxy alignments: An overview. *Space Sci. Rev.*, 193(1-4):1–65, 2015.

S. Joudaki et al. KiDS-450 + 2dFLenS: Cosmological parameter constraints from weak gravitational lensing tomography and overlapping redshift-space galaxy clustering. *Mon. Not. Roy. Astron. Soc.*, 474(4):4894–4924, 2018.

S. Joudaki et al. KiDS+VIKING-450 and DES-Y1 combined: Cosmology with cosmic shear. *arXiv:1906.09262*, 6 2019.

N. Kaiser. Weak Gravitational Lensing of Distant Galaxies. ApJ, 388:272, Apr. 1992.

A. Kannawadi et al. Towards emulating cosmic shear data: Revisiting the calibration of the shear measurements for the Kilo-Degree Survey. *Astron. Astrophys.*, 624:A92, 2019.

K. J. Kelly, P. A. Machado, S. J. Parke, Y. F. Perez Gonzalez, and R. Zukanovich-Funchal. Back to (Mass-)Square(d) One: The Neutrino Mass Ordering in Light of Recent Data. 7 2020.

M. Kilbinger. Cosmology with cosmic shear observations: a review. *Rept. Prog. Phys.*, 78:086901, 2015.

K. Kodama et al. Observation of tau neutrino interactions. *Phys. Lett. B*, 504:218–224, 2001.

D. Korytov et al. CosmoDC2: A Synthetic Sky Catalog for Dark Energy Science with LSST. *Astrophys. J. Suppl.*, 245(2):26, 2019.

M. Lattanzi and M. Gerbino. Status of neutrino properties and future prospects - Cosmological and astrophysical constraints. *Front. in Phys.*, 5:70, 2018.

R. Laureijs et al. Euclid Definition Study Report. *arXiv e-prints*, art. arXiv:1110.3193, Oct. 2011.

G. Lemaître. Un Univers homogène de masse constante et de rayon croissant rendant compte de la vitesse radiale des nébuleuses extra-galactiques. *Annales de la Société Scientifique de Bruxelles*, 47:49–59, Jan. 1927.

P. Lemos, A. Challinor, and G. Efstathiou. The effect of Limber and flat-sky approximations on galaxy weak lensing. *JCAP*, 05:014, 2017. doi: 10.1088/1475-7516/2017/05/014.

J. Lesgourgues and S. Pastor. Massive neutrinos and cosmology. *Phys. Rept.*, 429:307–379, 2006.

A. Lewis and A. Challinor. Weak gravitational lensing of the CMB. *Phys. Rept.*, 429:1–65, 2006.

A. Lewis, A. Challinor, and A. Lasenby. Efficient computation of CMB anisotropies in closed FRW models. *Astrophys. J.*, 538:473–476, 2000.

A. J. Long, M. Raveri, W. Hu, and S. Dodelson. Neutrino Mass Priors for Cosmology from Random Matrices. *Phys. Rev. D*, 97(4):043510, 2018.

C. S. Lorenz, D. Alonso, and P. G. Ferreira. Impact of relativistic effects on cosmological parameter estimation. *Phys. Rev.*, D97(2):023537, 2018.

A. Loureiro et al. On The Upper Bound of Neutrino Masses from Combined Cosmological Observations and Particle Physics Experiments. *Phys. Rev. Lett.*, 123(8):081301, 2019.

LSST Science Collaboration. LSST Science Book, Version 2.0. *arXiv e-prints*, art. arXiv:0912.0201, Dec 2009.

R. Mandelbaum et al. Weak lensing shear calibration with simulations of the HSC survey. *Mon. Not. Roy. Astron. Soc.*, 481(3):3170–3195, 2018.

J. C. Mather, E. S. Cheng, J. Eplee, R. E., R. B. Isaacman, S. S. Meyer, R. A. Shafer, R. Weiss, E. L. Wright, C. L. Bennett, N. W. Boggess, E. Dwek, S. Gulkis, M. G. Hauser, M. Janssen, T. Kelsall, P. M. Lubin, J. Moseley, S. H., T. L. Murdock, R. F. Silverberg, G. F. Smoot, and D. T. Wilkinson. A Preliminary Measurement of the Cosmic Microwave Background Spectrum by the Cosmic Background Explorer (COBE) Satellite. ApJ, 354:L37, May 1990.

J. C. Mather et al. Measurement of the Cosmic Microwave Background spectrum by the COBE FIRAS instrument. *Astrophys. J.*, 420:439–444, 1994.

D. J. Matthews and J. A. Newman. Reconstructing Redshift Distributions with Cross-correlations: Tests and an Optimized Recipe. ApJ, 721(1):456–468, Sept. 2010.

S. Mishra-Sharma, D. Alonso, and J. Dunkley. Neutrino masses and beyond- ΛCDM cosmology with LSST and future CMB experiments. *Phys. Rev. D*, 97(12):123544, 2018.

H. Mo, F. van den Bosch, and S. White. *Galaxy Formation and Evolution*. Cambridge University Press, 2010.

C. B. Morrison and H. Hildebrandt. Mitigating Systematic Errors in Angular Correlation Function Measurements from Wide Field Surveys. *Mon. Not. Roy. Astron. Soc.*, 454(3):3121–3133, 2015.

D. Munshi, P. Valageas, L. Van Waerbeke, and A. Heavens. Cosmology with Weak Lensing Surveys. *Phys. Rept.*, 462:67–121, 2008.

S. G. Murray, C. Power, and A. S. G. Robotham. HMFcalc: An online tool for calculating dark matter halo mass functions. *Astronomy and Computing*, 3:23–34, Nov 2013.

J. F. Navarro, C. S. Frenk, and S. D. M. White. The Structure of Cold Dark Matter Halos. ApJ, 462: 563, May 1996.

S. S. Olivier, L. Seppala, and K. Gilmore. Optical design of the LSST camera. 7018:70182G, July 2008.

N. Palanque-Delabrouille et al. Neutrino masses and cosmology with Lyman-alpha forest power spectrum. *JCAP*, 11:011, 2015.

R. Patterson. Prospects for Measurement of the Neutrino Mass Hierarchy. *Ann. Rev. Nucl. Part. Sci.*, 65:177–192, 2015.

W. Pauli. Dear radioactive ladies and gentlemen. *Phys. Today*, 31N9:27, 1978.

S. Perlmutter et al. Measurements of Ω and Λ from 42 high redshift supernovae. *Astrophys. J.*, 517: 565–586, 1999.

X. Qian and P. Vogel. Neutrino Mass Hierarchy. *Prog. Part. Nucl. Phys.*, 83:1–30, 2015.

C. L. Reichardt. Observing the Epoch of Reionization with the Cosmic Microwave Background. *arXiv:1511.01117*, 11 2015.

B. A. Reid et al. Cosmological constraints from the clustering of the Sloan Digital Sky Survey DR7 luminous red galaxies. MNRAS, 404(1):60–85, May 2010.

J. Rhodes et al. Scientific Synergy Between LSST and $Euclid$. *Astrophys. J. Suppl.*, 233(2):21, 2017.

A. G. Riess, S. Casertano, W. Yuan, L. M. Macri, and D. Scolnic. Large Magellanic Cloud Cepheid Standards Provide a 1% Foundation for the Determination of the Hubble Constant and Stronger Evidence for Physics beyond ΛCDM. *Astrophys. J.*, 876(1):85, 2019.

A. G. Riess et al. Observational evidence from supernovae for an accelerating universe and a cosmological constant. *Astron. J.*, 116:1009–1038, 1998.

V. C. Rubin and J. Ford, W. Kent. Rotation of the Andromeda Nebula from a Spectroscopic Survey of Emission Regions. ApJ, 159:379, Feb. 1970.

T. Sauer. *Numerical Analysis*. Pearson, 2012.

F. Schmidt, A. Leauthaud, R. Massey, J. Rhodes, M. R. George, A. M. Koekemoer, A. Finoguenov, and M. Tanaka. A DETECTION OF WEAK-LENSING MAGNIFICATION USING GALAXY SIZES AND MAGNITUDES. *The Astrophysical Journal*, 744(2):L22, dec 2011.

M. Schmidt. Space Distribution and Luminosity Functions of Quasi-Stellar Radio Sources. ApJ, 151: 393, Feb. 1968.

P. Schneider. *Extragalactic Astronomy and Cosmology*. Springer, 2015.

R. L. Schuhmann, C. Heymans, and J. Zuntz. Galaxy shape measurement synergies between LSST and Euclid. *arXiv:1901.08586*, 1 2019.

F. Simpson, R. Jimenez, C. Pena-Garay, and L. Verde. Strong Bayesian Evidence for the Normal Neutrino Hierarchy. *JCAP*, 06:029, 2017.

G. F. Smoot et al. Structure in the COBE Differential Microwave Radiometer First-Year Maps. ApJ, 396:L1, Sept. 1992.

D. Spergel et al. Wide-Field InfrarRed Survey Telescope-Astrophysics Focused Telescope Assets WFIRST-AFTA 2015 Report. *arXiv:1503.03757*, Mar. 2015.

R. Takahashi, M. Sato, T. Nishimichi, A. Taruya, and M. Oguri. Revising the Halofit Model for the Nonlinear Matter Power Spectrum. ApJ, 761(2):152, Dec. 2012. doi: 10.1088/0004-637X/761/2/152.

M. Tanabashi et al. Review of Particle Physics. *Phys. Rev. D*, 98(3):030001, 2018.

M. Tegmark, A. Taylor, and A. Heavens. Karhunen-Loeve eigenvalue problems in cosmology: How should we tackle large data sets? *Astrophys. J.*, 480:22, 1997.

L. Thiele, C. A. J. Duncan, and D. Alonso. Disentangling magnification in combined shear-clustering analyses. *arXiv:1907.13205*, 2019.

J. L. Tinker, B. E. Robertson, A. V. Kravtsov, A. Klypin, M. S. Warren, G. Yepes, and S. Gottlöber. The Large-scale Bias of Dark Matter Halos: Numerical Calibration and Model Tests. ApJ, 724(2): 878–886, Dec. 2010.

M. A. Troxel et al. Dark Energy Survey Year 1 results: Cosmological constraints from cosmic shear. *Phys. Rev.*, D98(4):043528, 2018.

S. Vagnozzi, E. Giusarma, O. Mena, K. Freese, M. Gerbino, S. Ho, and M. Lattanzi. Unveiling ν secrets with cosmological data: neutrino masses and mass hierarchy. *Phys. Rev. D*, 96(12):123503, 2017.

F. C. van den Bosch, S. More, M. Cacciato, H. Mo, and X. Yang. Cosmological constraints from a combination of galaxy clustering and lensing - I. Theoretical framework. MNRAS, 430(2): 725–746, Apr. 2013.

E. van Uitert et al. KiDS+GAMA: cosmology constraints from a joint analysis of cosmic shear, galaxygalaxy lensing, and angular clustering. *Mon. Not. Roy. Astron. Soc.*, 476(4):4662–4689, 2018.

P. Virtanen, R. Gommers, T. E. Oliphant, M. Haberland, T. Reddy, D. Cournapeau, E. Burovski, P. Peterson, W. Weckesser, J. Bright, S. J. van der Walt, M. Brett, J. Wilson, K. Jarrod Millman, N. Mayorov, A. R. J. Nelson, E. Jones, R. Kern, E. Larson, C. Carey, İ. Polat, Y. Feng, E. W. Moore, J. Vand erPlas, D. Laxalde, J. Perktold, R. Cimrman, I. Henriksen, E. A. Quintero, C. R. Harris, A. M. Archibald, A. H. Ribeiro, F. Pedregosa, P. van Mulbregt, and S. . . Contributors. SciPy 1.0: Fundamental Algorithms for Scientific Computing in Python. *Nature Methods*, 17:261–272, 2020.

S. Weinberg. *Cosmology*. Oxford University Press, 2008.

L. Xu and Q.-G. Huang. Detecting the Neutrinos Mass Hierarchy from Cosmological Data. *Sci. China Phys. Mech. Astron.*, 61(3):039521, 2018.

X. Yang, H. J. Mo, and F. C. van den Bosch. Constraining galaxy formation and cosmology with the conditional luminosity function of galaxies. MNRAS, 339(4):1057–1080, Mar. 2003.

X. Yang, H. J. Mo, and F. C. van den Bosch. Galaxy Groups in the SDSS DR4. II. Halo Occupation Statistics. ApJ, 676(1):248–261, Mar. 2008.

J. Zuntz, M. Paterno, E. Jennings, D. Rudd, A. Manzotti, S. Dodelson, S. Bridle, S. Sehrish, and J. Kowalkowski. CosmoSIS: modular cosmological parameter estimation. *Astron. Comput.*, 12: 45–59, 2015.

J. Zuntz et al. Dark Energy Survey Year 1 Results: Weak Lensing Shape Catalogues. *Mon. Not. Roy. Astron. Soc.*, 481(1):1149–1182, 2018.

F. Zwicky. Die Rotverschiebung von extragalaktischen Nebeln. *Helvetica Physica Acta*, 6:110–127, Jan. 1933.